

TOWARDS TRANSFERABLE POLLUTION DETECTION METHODS IN AQUATIC ENVIRONMENTS USING HYPERSPPECTRAL TECHNOLOGY

Ámbar Pérez-García

Supervisors:

José Fco. López Feliciano

Tim H.M. van Emmerik

Programa de Doctorado en
Tecnologías de Telecomunicación e Ingeniería Computacional

March 2024
Las Palmas de Gran Canaria





IUMA
Instituto Universitario de
Microelectrónica Aplicada

Universidad de Las Palmas de Gran Canaria
Programa de Doctorado en Tecnologías de Telecomunicación
e Ingeniería Computacional
Escuela de Doctorado

Towards Transferable Pollution Detection Methods in Aquatic Environments Using Hyperspectral Technology

Ámbar Pérez-García

José Fco. López Feliciano

Tim H.M. van Emmerik

Las Palmas de Gran Canaria

March 2024



Consejería de Universidades,
Ciencia e Innovación y Cultura
Agencia Canaria de Investigación,
Innovación y Sociedad
de la Información



Cofinanciado por
la Unión Europea



Fondos Europeos

Acknowledgments

I would like to express my sincere gratitude to my thesis supervisor, José F. López, for giving me the opportunity to delve into the world of research and for guiding me with commitment and dedication throughout this process. Your trust and support have allowed me to explore new ideas, always with the freedom to make my own decisions and follow my own path. Thank you for instilling in me your enthusiasm for projects and new challenges.

I would also like to thank my co-supervisor, Tim H.M. van Emmerik, who joined my project halfway through. With you began my enriching international collaborations with Wageningen University & Research, which have been an essential part of my development as a researcher. Thank you for sharing your experience with me and for the inspiring conversations we have had.

My thanks also go to all my colleagues, both in Spain and the Netherlands. Their valuable advice and the discussions we've had have enriched me as a researcher. Additionally, in our moments of rest, we had the opportunity to get to know each other better and forge friendships that I now carry with me.

o

Finalmente, quiero dedicar unas palabras especiales a mi familia y amigos, quienes me han acompañado a lo largo de todo este proceso. Agradezco profundamente a mis padres, Elsa y José, su paciencia y comprensión, y por ser un pilar fundamental en mi vida. Y no puedo dejar de agradecer a mi compañero de vida, Luismi, que me acompaña en todos mis proyectos.

Summary

This thesis presents a suite of transferable methodologies for environmental monitoring, focusing on detecting pollutants in aquatic ecosystems. Leveraging remote sensing with hyperspectral imaging (HSI) and artificial intelligence (AI), these approaches enable precise pollutant identification and adaptability across diverse scenarios. Thus, supporting systematic observation over extensive geographic regions or long-term datasets contributes to developing standardized solutions for monitoring and protecting Earth's ecosystems.

Aquatic pollution threatens biodiversity and ecosystem services, especially oil spills and plastic waste. Oil spills spread quickly across water surfaces, blocking sunlight and endangering aquatic biodiversity. Plastic waste accumulates in water bodies, breaking into microplastics that marine organisms ingest, disrupting food chains. Both pollutants are especially critical to monitor because they have profound, long-term impacts on ecosystems and food webs. Dye tracers such as rhodamine can be used as a proxy in oil spill simulations due to their similar dispersion behaviour in water. This aids in the development of detection and monitoring techniques for real oil spill events. However, there is a need for efficient and transferable aquatic pollution monitoring technologies.

HSI is a powerful tool for identifying aquatic pollutants due to its rich spectral detail. However, the massive data it generates is costly and complex to process, posing key challenges. Dimensionality reduction techniques—such as spectral indices and band selection—can trim redundant data, reducing storage and computational demand while maintaining accuracy. Furthermore, the scarcity of labelled datasets hinders AI model training. Unsupervised learning approaches offer a promising solution, enabling models to extract meaningful patterns from non-labelled data, making HSI more adaptable across diverse environments.

This thesis aims to pioneer efficient and transferable HSI methodologies for detecting and monitoring critical aquatic pollutants. It focuses on developing novel approaches that streamline data analysis and improve transferability across diverse environments. The research progresses from well-established, straightforward methods such as spectral indexes to cutting-edge AI methodologies to enhance pollutant detection. Each chapter focuses on different HSI technology needs, overcoming the challenges of data complexity, dimensionality, and the scarcity of labelled datasets. This creates a cohesive framework that addresses the demands of large-scale environmental monitoring with adaptable HSI methods.

Chapter 2 reduces HSI data complexity by introducing the *Normalized Difference Oil Index (NDOI)*, a new spectral index designed to improve oil spill detection in coastal areas. The study compares the performance of several spectral indices utilizing images from multiple satellite and airborne sensors—AVIRIS, HICO, and MERIS—captured during the Deepwater Horizon disaster in the Gulf of Mexico in 2010. Traditional indices often misclassify other elements, such as suspended sediments, leading to inaccurate results. The NDOI avoids sand-in-suspension false positives, offering a more reliable response in coastal areas. NDOI is suitable for detecting oil spills thicker than 50 microns, with an average oil F1-score of 83%, and estimating its thickness and oil volume exceeding 90% accuracy. It also provides rapid detection of oil spills due to its simple calculation compared with other spectral indices and IA models, which is crucial for quick responses to environmental crises. This development directly contributes to optimizing the use of optical sensors for fast and efficient pollutant detection.

Chapter 3 tackles the challenge of hyperspectral data’s high dimensionality by presenting a new dimensionality reduction methodology. The spectral band selection method identifies the most relevant bands for detecting specific pollutants, with testing conducted on plastics and rhodamine. This minimises redundant or irrelevant bands, reducing computational cost and resource demands. This methodology has been applied to laboratory images and outdoor experiments, focusing on analyzing the impact of background effects on identifying target objects. The methodology successfully transferred influential spectral bands between datasets with 80-90% accuracy, indicating the potential for developing specialized sensors with these common bands to enable detection across various environments. However, the transfer of pre-trained classification models remains an area for further research, particularly regarding semi-transparent objects or solutions influenced by background reflections in complex environments like optically shallow waters. Refined post-processing approaches suggest that model transfer could be feasible, potentially reducing the need for labelled data or in-situ validation, thus preserving resources and enabling a more generalizable classifier.

Chapter 4 addresses the scarcity of labelled data in HSI and AI applications through the *spectral loss function (Sl)*, which enhances HSI segmentation in unsupervised neural networks. The loss function is tested on HSI benchmark datasets, such as Pavia University, Salinas Valley, Indian Pines, and University of Houston, and a case study using an AVIRIS image from the Deepwater Horizon catastrophe. *Sl* was introduced in the currently best-performing unsupervised segmentation neural network, enhancing evaluation metrics performance by up to 6%. The proposed method also outperforms well-established techniques, such as spectral indices. For example, spectral indices rely on few spectral bands to produce a numerical value for each pixel, requiring an expert to

establish a threshold for class determination. In contrast, the unsupervised neural network can directly assign different classes to varying oil thicknesses based on their complete spectral response, making them fully transferable across environments. Therefore, the unsupervised approach can generate ground-truth data, reducing manual labour. This is especially relevant for remote areas such as the open ocean, where manual labelling is challenging and resource-intensive. This contribution expands the scope of AI-driven detection techniques to operate without labelled datasets, thereby enhancing adaptability.

This thesis concludes with a synthesis of the main insights from each chapter, a reflection on the implications and limitations identified, and suggestions for future research directions. The thesis successfully develops new transferable HSI methods that enhance the detection and monitoring of aquatic pollutants, overcoming critical knowledge gaps. Spectral indices, such as NDOI, provide a quick and efficient solution for rapid, low-resource decision-making but rely on manual thresholding. Band selection methods help identify critical spectral bands, which can improve model transfer and generalization across environments. Unsupervised methods complement these techniques by addressing non-labelled datasets, providing a foundation for large-scale monitoring. This research contributes to more efficient, adaptable, and transferable environmental monitoring technologies by addressing critical challenges related to data complexity, dimensionality reduction, and the scarcity of labelled datasets. The strengths and weaknesses of this suite of methods should be carefully considered to select the most appropriate approach based on each study's specific characteristics.

These advancements hold promise for designing next-generation sensors for UAVs and space missions, prioritizing data efficiency and precision. Moreover, the techniques directly apply to environmental management, including early spill detection, beach cleanup coordination, and supporting data-driven policies. Future work will focus on further automating hyperspectral monitoring techniques to minimize manual intervention. Efforts will be directed toward improving algorithm transferability by incorporating more variability in training data and advancing post-processing techniques. Additionally, the scalability of emerging tools, such as cloud computing, will be explored to improve efficient large-scale monitoring.

This thesis contributes to advancing aquatic pollution monitoring by presenting novel transferable remote sensing methodologies that support environmental preservation.

Contents

1	Introduction	1
1.1	Background	1
1.1.1	Aquatic Pollution	2
1.1.2	Principles of Remote Sensing	4
1.1.3	Detection techniques	7
1.2	Knowledge Gaps	10
1.3	Objectives	13
1.4	List of Publications	14
1.5	Justification of the Thematic Unit	15
1.6	Fundings	17
2	Spectral Indices to Reduce Misclassification in Oil Spill Detection	21
2.1	Spectral Indices Survey for Oil Spill Detection in Coastal Areas	22
3	Band Selection Method for Efficient Water Pollution Monitoring	37
3.1	Efficient Plastic Detection in Coastal Areas with Selected Spectral Bands	40
3.2	Developing a Generalizable Spectral Classifier for Rhodamine Detection in Aquatic Environments	48
4	Unsupervised Hyperspectral Methods for Scalable Monitoring	67
4.1	Novel Spectral Loss Function for Unsupervised Hyperspectral Image Segmentation	68
5	Conclusions	75
5.1	Future work	77
A	Resumen en Español	81
	Bibliography	85

Chapter 1

Introduction

This section provides an overview of the context, motivations, and objectives that underpin this research. It begins with a background on key topics, including the challenges of aquatic pollution, the fundamentals of remote sensing and Hyperspectral imaging, and a summary of the artificial intelligence techniques applied in the study. The section also highlights significant gaps in current knowledge, which have driven the focus of this study and its main research objectives. Additionally, the section includes a brief list of publications arising from the research, a justification of the thematic unit within the broader scientific framework, and an outline of the funding sources supporting the work.

1.1 Background

There is a need to improve the detection and monitoring of pollution to enable more effective responses and strengthen legislation. Pollutants in aquatic environments have significant and long-lasting effects on biodiversity, water quality, and ecosystem health [1, 2]. Oil spills and plastic waste are some of the most widespread contaminants, posing risks to aquatic life and human communities that rely on healthy coastal and ocean environments [3–5]. Traditional techniques for monitoring aquatic hazardous agents rely on in situ measurements, which are costly, resource-intensive, time-consuming, require expert supervision, and face geographical limitations [6–8].

In this context, new technologies and methodologies are needed to improve the identification of marine debris in a fast, accurate and transferable way (Figure 1.1) [9]. Remote sensing plays a crucial role in this process by enabling large-scale data collection without the need for direct physical interaction, making it ideal for monitoring hard-to-reach areas. Hyperspectral Imaging (HSI) is an advanced remote sensing technique that captures vast data across the electromagnetic spectrum for material identification [10]. Combined with artificial intelligence, HSI improves environmental monitoring efficiency and facilitates global algorithm application [11–13]. This integration is vital for rapid response, lower operational costs, and tracking pollution hotspots [14–16].

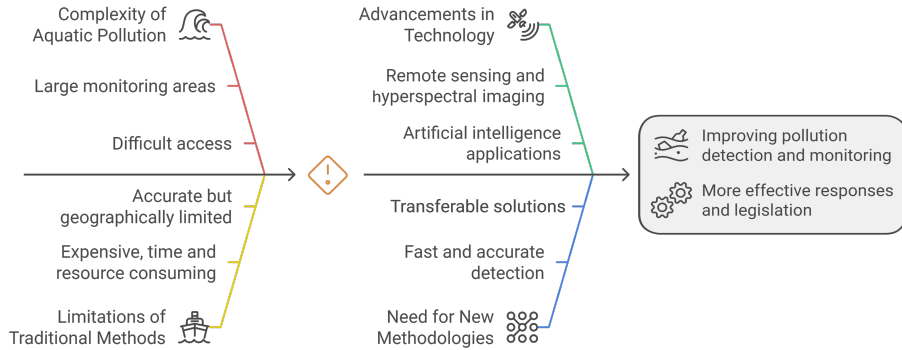


Figure 1.1: Aquatic pollutant monitoring needs.

1.1.1 Aquatic Pollution

As human activities have intensified over the past few decades, pollution in aquatic environments has significantly increased, contributing to the deterioration of these ecosystems [1]. Coastal areas and rivers are particularly vulnerable due to their proximity to human activities such as industry, agriculture, and urbanization [17]. When pollutants such as oil and plastics enter aquatic environments, they are distributed according to water movement and hydrodynamics [18], directly disrupting the feeding and breeding behaviours of marine organisms and smothering coral reefs, which are critical for biodiversity [19]. The effects of pollution extend beyond wildlife, as they pose significant risks to human health. Pollutants can bioaccumulate in marine organisms, leading to higher concentrations of toxins as they move up the food chain [20]. This poses a direct threat to humans who consume contaminated seafood. Additionally, pollution degrades the quality of coastal waters, affecting industries such as tourism and fishing, and leading to economic losses [21]. Figure 1.2 illustrates the pollutants examined in this thesis, emphasizing the role of hydrodynamics in their distribution and the impact on Earth and society.

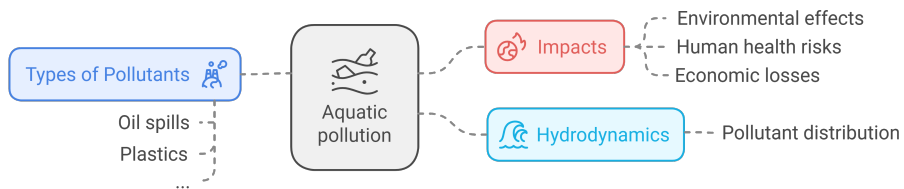


Figure 1.2: Overview of aquatic pollution in this thesis

Oil spills and plastics have garnered significant attention due to their widespread prevalence and persistence in marine environments. Plastic pollution is a pervasive problem affecting terrestrial and aquatic ecosystems globally [4]. The highest concentrations of plastic pollution are seen along shorelines, water and seafloors, particularly near densely populated regions and industrialized areas [4]. Plastic degrades into smaller pieces that remain for centuries, posing long-term ecological threats [22]. Plastics are non-biodegradable material, accumulating in ecosystems and harming wildlife [23]. Animals often mistake plastic debris for food, leading to ingestion and entanglement, which causes injury, starvation, and death [24]. Additionally, plastics act as vectors for chemical pollutants, which adhere to their surfaces and enter organisms, leading to long-term toxic effects [25]. Coastal areas, where human activity is concentrated, often suffer the most, with visible pollution affecting beaches [3].

Oil spills cause immediate and severe damage to ecosystems [2]. Oil spills, often caused by accidents involving tankers, refineries, or offshore platforms during drilling and transportation, are among the most destructive forms of aquatic pollution [26, 27]. Oil floats on the water's surface and spreads rapidly, forming slicks that block sunlight [28]. Its harmful effects on invertebrate fauna vary depending on the oil's type, exposure duration, and environmental conditions such as water temperature and depth [29]. Over time, oil can sink and contaminate the seafloor, severely affecting deep-sea ecosystems [30]. A notable example is the 2010 Deepwater Horizon disaster, where approximately 800,000 cubic meters of oil were released into the Gulf of Mexico for months, devastating wildlife and coating thousands of birds, mammals, and sea turtles in oil [31]. It also caused long-term economic losses including over 25,000 jobs, \$2.3 billion in industry output, and \$1.2 billion in gross regional product, along with hundreds of millions in lost tax revenues. [32].

Another important aspect to consider is hydrodynamics, the study of liquids in motion, which is essential for understanding how water movement affects the distribution and transport of pollutants in aquatic environments [33]. Ocean currents, driven by wind, tides, temperature differences, and the Earth's rotation, transport pollutants across vast distances [34]. For instance, the spread of oil spills is affected by water properties and the oil's viscosity, while oceanic gyres trap plastic waste in swirling vortexes, such as the Great Pacific Garbage Patch [35]. This is a massive concentration of plastic debris located in the North Pacific Ocean, where the convergence of several ocean currents forms a swirling vortex, pulling in and containing millions of tons of floating plastic and other waste [36]. Understanding these dynamics is essential for developing effective monitoring and mitigation strategies [18]. Scientists frequently use dye tracers, such as rhodamine, to study localized water movement and predict pollutant dispersion [37]. These dyes help map the flow and velocity of currents, allowing researchers to create accurate models of how contaminants

might be transported [38]. Such insights are precious in coastal areas, where pollution tends to accumulate, and can guide more targeted and efficient cleanup efforts [39].

Therefore, developing new tools and technologies that allow us to address these environmental challenges more effectively is essential. With oil spills and plastics threatening aquatic ecosystems, fast and advanced methods such as hyperspectral imaging are critical for rapidly detecting these contaminants and responding to environmental crises [40]. These innovations are crucial for developing scalable solutions to mitigate the impacts of human activities on the environment.

1.1.2 Principles of Remote Sensing

Remote sensing is a technology used to gather information about the Earth's surface without physical contact, typically through satellites or aircraft [41]. By detecting and recording reflected or emitted energy from various surfaces, remote sensing enables monitoring and analyzing environmental changes, mapping landscapes, and assessing resources across large or hard-to-access areas [42]. Widely applied in fields like agriculture, forestry, climate science, and disaster management, remote sensing provides crucial data for tracking natural and human-made changes over time, supporting better-informed decision-making on global and local scales [43].

Optical Sensing Technologies

Optical sensors are pivotal in remote sensing, converting light into measurable signals to analyze various biophysical parameters [44]. Within the optical range, the studies will be focused on the Visible (VIS, 400–700 nm), Near Infrared (NIR, 700–1400 nm), Visible and Near Infrared (VNIR, 400–1000 nm), and Short-Wave Infrared (SWIR, 1000–2500 nm) regions [42]. These sensors provide non-destructive measurement capabilities, allowing researchers to analyze ecosystems without disruption. They can be categorized into multispectral and hyperspectral sensors (Figure 1.3), each serving distinct applications and offering unique advantages and limitations [42].

Multispectral Sensors These sensors capture data in a limited number of broad spectral bands, typically three to ten. RGB sensors, which capture data in the red, green, and blue bands are widely used in remote sensing for producing true-color images that resemble what we would see naturally.

Hyperspectral Sensors They collect data across hundreds of narrow, contiguous spectral bands, allowing for a detailed spectral analysis of materials.

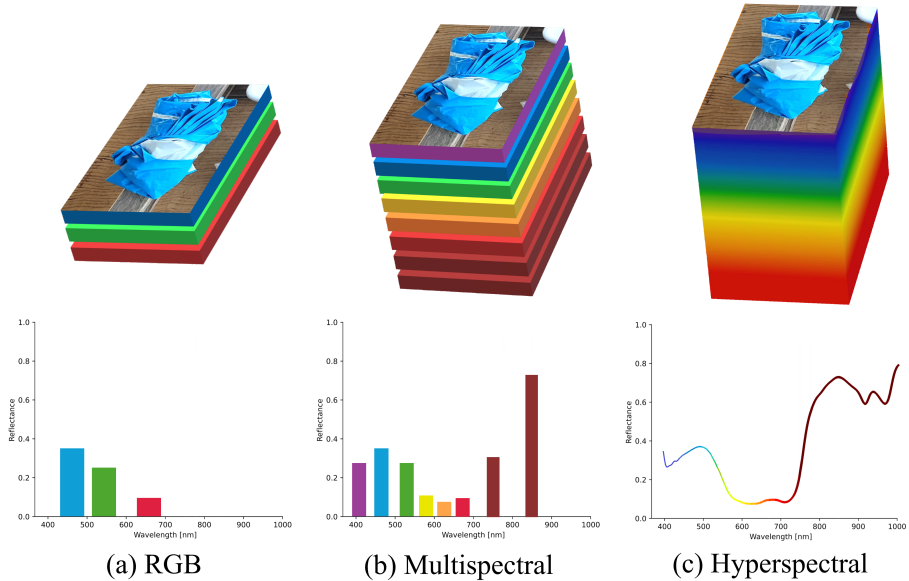


Figure 1.3: Comparison of multispectral and hyperspectral information.

Multispectral sensors provide helpful information for applications like vegetation mapping and land cover classification, but their spectral resolution is relatively low [45]. This can limit their ability to differentiate between similar materials, making them less effective for complex analyses. In contrast, the high spectral resolution of hyperspectral sensors enables the identification of subtle differences in material properties and is particularly advantageous for challenging applications [45]. However, compared to their multispectral counterparts, hyperspectral sensors are 3 to 5 times more expensive and capture data across hundreds of narrow spectral bands (typically from 100 to 300), whereas multispectral sensors capture only from 3 to 10 broad bands [46]. This high dimensionality in hyperspectral sensors results in 10 to 20 times more data volume, which presents significant challenges in terms of storage, processing, and analysis, complicating operational workflows [47].

The versatility of optical sensors allows deployment across various platforms—satellites, airborne systems, and UAVs—enabling wide-area monitoring and flexible data collection tailored to specific needs [15, 48].

Satellite-based systems These systems offer extensive coverage and are well-suited for large-scale monitoring of marine environments. However, their revisit period and spatial resolution may be insufficient for detecting small-

scale pollution events [49]. Additionally, cloud cover presents a limitation when relying on these platforms [50].

Airborne systems They can capture higher spatial resolution data than satellites and be deployed more frequently, allowing for timely assessment of pollution events. However, airborne systems are typically more costly to operate and may have flight duration and coverage area limitations [51,52].

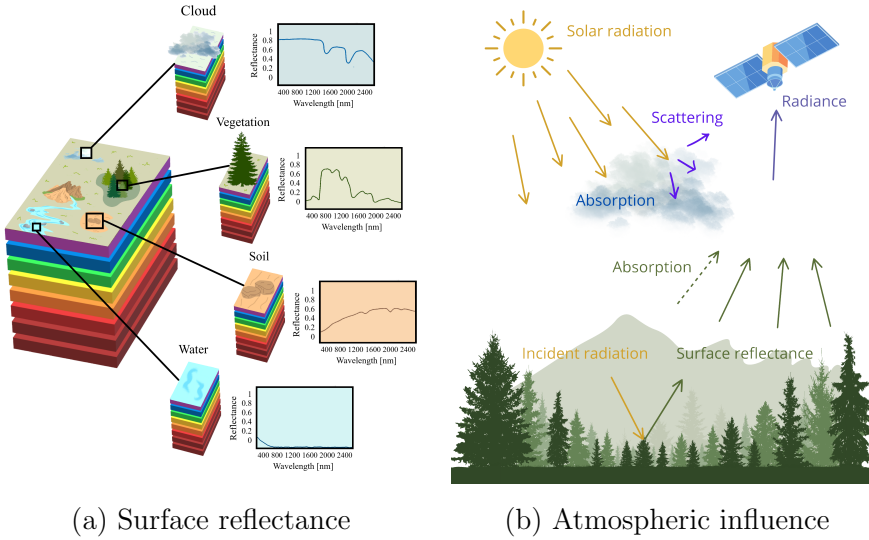
UAV-based systems Uncrewed Aerial Vehicles (UAVs) represent a growing field in remote sensing, offering high spatial resolution and flexibility in data collection. UAVs are quickly deployable and effective for localized pollution assessments, but they have limited operational range and require skilled operators for data collection and analysis [15,38].

In summary, each technology has advantages and limitations, but it is clear that optical sensors, encompassing multispectral and hyperspectral technologies, play a crucial role in environmental pollution monitoring.

Hyperspectral Imaging (HSI)

Hyperspectral Imaging (HSI) is a remote sensing technique that captures data across a broad range of the electromagnetic spectrum [42]. It divides the spectrum into hundreds of narrow, contiguous bands and generates detailed spectral profiles for each pixel in an image [53,54]. The data acquired through HSI is typically organized into large three-dimensional data cubes, where each pixel contains an N -dimensional vector, with N corresponding to the number of spectral bands [55]. This structure facilitates comprehensive material analysis, as the spectral signature of each pixel can be processed to identify and differentiate various substances (Figure 1.4 (a)), including pollutants [40].

HSI measures solar radiation reflected off the Earth's surface after interacting with the atmosphere. The radiant flux intensity at a specific wavelength and surface is quantified in watts per square meter steradian [$W/(sr \cdot m^2)$] [42]. However, this raw data is influenced by atmospheric conditions, as shown in Figure 1.4 (b), which can distort the measured signals. To mitigate these effects, reflectance is utilized, which is defined as the ratio of emitted surface flux to incident solar flux [45]. Reflectance values are obtained after atmospheric correction, providing a more accurate representation of the surface characteristics [56]. The underlying principle of HSI is based on the distinct ways different materials reflect solar radiation [57]. Depending on the atomic structure of a surface, solar radiation is absorbed or reflected at specific wavelengths, resulting in a distinct spectral response for each material, which is called spectral signature [47]. These spectral signatures depend highly on the material's physical and chemical properties and surface roughness.



(a) Surface reflectance

(b) Atmospheric influence

Figure 1.4: Hyperspectral technology fundamentals.

HSI has broad applications across various Earth observation fields, including precision agriculture, risk prevention, environmental studies, and natural resource management [42]. In particular, HSI detects pollutants in aquatic environments by analyzing their unique spectral responses, which are influenced by their interactions with electromagnetic waves and the optical properties of water, such as absorption and scattering [58]. This capability allows for accurate identification and analysis of surface materials, facilitating informed decision-making and enhancing management strategies for Earth’s observation and pollution control [59]. HSI remote sensing also enables large-scale monitoring by facilitating the analysis of extensive data collected across vast geographic areas, diverse locations, or long-term periods [43]. Thus, HSI is a powerful tool for providing precise solutions in environmental management [60].

1.1.3 Detection techniques

HSI offers rich spectral information, but its high dimensionality makes analysis complex due to challenges in managing noise and redundancy within the datasets [53]. Several techniques can help reduce the complexity of HSI, with spectral indices and various AI methods being among the most commonly used. Figure 1.5 summarises the techniques employed in each thesis chapter.

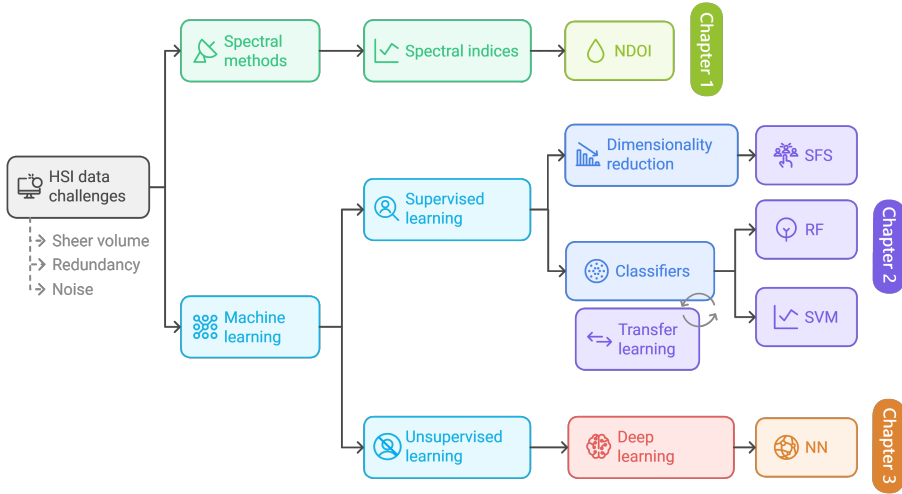


Figure 1.5: Outline of the techniques applied in this thesis.

Spectral indexes

Spectral indices are powerful tools in HSI that simplify complex data analysis by combining multiple spectral bands through simple arithmetic operations [61]. These indices highlight specific spectral behaviours of interest while suppressing background noise or irrelevant information [62].

The choice of bands used in spectral indices is crucial and depends on the unique spectral characteristics of the phenomenon being studied [63]. For example, certain materials or pollutants have distinct reflectance patterns at specific wavelengths, making it possible to create indices that emphasize those features while reducing the influence of other, less relevant bands [58]. Common examples include vegetation indices like the Normalized Difference Vegetation Index (NDVI) [64], which is used to highlight plant health by combining the near-infrared and red bands (Equation 1.1), or the Chlorophyll content (CHL) [65], which measures the surface chlorophyll-a using violet, blue and green bands (Equation 1.2).

$$NDVI = \frac{NIR - Red}{NIR + Red} \quad (1.1)$$

$$CHL = \log(\max(R_{433,490,510})/R_{555}) \quad (1.2)$$

Artificial Intelligence (AI) Techniques for HSI

AI techniques have become essential tools in overcoming these challenges, improving the efficiency of surface classification and enhancing hyperspectral data analysis [66–68]. AI encompasses a broad range of technologies and methodologies designed to enable machines to mimic human intelligence and perform tasks that typically require cognitive functions, such as learning, reasoning, and problem-solving [69]. Within this expansive and changing discipline, Machine Learning (ML) and Deep Learning (DL) have transformed various fields, including healthcare, finance, and environmental monitoring [67]. As AI is a large field, we will limit this section to introduce the concepts necessary to understand the chapters in this study.

Machine Learning Is a branch of AI that focuses on developing algorithms that allow computers to learn from and make predictions or decisions based on data without being explicitly programmed [70].

Deep Learning Is a specialized area within ML that employs neural networks with multiple layers (hence “deep”) to analyze complex patterns in large datasets [71]. This approach has proven particularly effective for image recognition [72]. The performance of deep learning models is heavily influenced by the choice of loss function, which measures the difference between the predicted and actual outcomes, guiding the optimization process during training [73].

Dimensionality reduction Is an ML technique that aims to reduce the number of input variables in a dataset while preserving essential information, improving model performance and decreasing computational cost [74]. A common method for HSI dimensionality reduction is Sequential Feature Selection (SFS) [75], a band selection technique that iteratively selects relevant bands based on their contribution to model predictive power, thereby enhancing its efficiency and interoperability [69].

ML algorithms can be classified as follows¹ [76]:

- **Supervised learning:** models are trained on labelled datasets, meaning that each input is paired with the correct output, and the goal is to learn a mapping from inputs to outputs so that the model can make accurate predictions on new, unseen data [69].
 - **Classification:** is one of the most common techniques in supervised learning, where the goal is to assign a label or category to a new instance based on the features learned from labelled data [77]. These

¹DL and dimensionality reduction techniques can be supervised and unsupervised.

approaches accurately classify materials based on spectral signatures but require an expert to identify and label the surfaces [78]. Standard classification algorithms include Support Vector Machines (SVM) [79] and Random Forests (RF) [80].

- **Unsupervised learning:** identify patterns and groupings within the data through clustering and dimensionality reduction techniques without labelled data. While less precise, these methods alleviate the need for specialized experts to label data, which is significantly time-consuming, and can also assist in labelling datasets more efficiently [69, 81].
 - **Segmentation:** is akin to classification; each pixel is assigned a category, with neighbouring pixels sharing the same label treated as part of the same object or region, thus preserving spatial context. While segmentation can be performed using supervised methods, unsupervised techniques such as k-means clustering [82] and unsupervised NNs [83–86] are more commonly utilized in practice to reveal inherent structures in hyperspectral datasets [81].

Finally, transfer learning is not an ML subcategory but a technique or strategy that can be applied within various ML paradigms [87]. This strategy leverages a pre-trained model initially developed for one task and adapts it for a different but related task [88]. This allows for faster training and improved performance, especially when the new task has limited data [89]. This strategy reuses knowledge from one hyperspectral scene and applies it to another, often improving efficiency and accuracy with less data or computational resources [87].

1.2 Knowledge Gaps

HSI offers a significant advantage over traditional RGB and multispectral imaging by providing detailed spectral information across hundreds of narrow bands [45]. HSI's rich spectral resolution enables precise differentiation between materials that may look similar in conventional images [90–92]. However, several challenges remain to be fully addressed, including managing the vast amount of data that HSI generates, developing models that adapt to diverse environments, and the restrictions linked to the difficulty in obtaining labelled datasets for analysis [93–96]. These issues collectively restrict the practical large-scale deployment of standardized HSI methods for environmental monitoring and pollution detection [97, 98].

HSI provides rich spectral information, but its high dimensionality and complexity pose significant challenges for data processing [53]. Each pixel of HSI data contains extensive spectral information, requiring ample storage, advanced

processing power, and efficient algorithms [53, 99]. The sheer volume of data collected—often comprising hundreds of spectral bands—leads to the “curse of dimensionality,” where traditional algorithms struggle to find meaningful patterns amid vast datasets [100]. Furthermore, noise and redundancy in the data can obscure critical signals, complicating the identification of surfaces and making pollutant detection a slow and resource-intensive process [74].

Some approaches to reduce HSI complexity are to apply spectral indexes or dimensionality reduction methods [99]. Spectral indexes combine a few spectral bands with simple arithmetic operations to extract information about target characteristics, facilitating analysis for particular applications [101]. Nevertheless, spectral indexes face limitations, such as reliance on manual thresholding and difficulty distinguishing between multiple objects [102]. Some band selection methods to reduce HSI dimensionality have been developed, but most focus on general-purpose spectral bands rather than optimizing them for specific tasks or detecting particular contaminants [103]. Band selection methods can aid in developing specialized sensors for specific tasks, complementing current space missions like Sentinel-2 [104] and Landsat 8 [105], which use general multispectral bands for broad applications. Specialized multispectral sensors must balance sensor resolution, cost, and pollutant detection capabilities [46]. This balance is especially critical for emerging technologies such as drones (UAVs) and nanosatellites, where constraints on space and hardware demand efficient data usage [15, 106].

A key to improving monitoring effectiveness is developing transferable methods that enable the use of pre-trained ML models across diverse scenarios [87]. Band selection methods can facilitate this goal by identifying the most influential spectral ranges for detecting specific contaminants, thereby enhancing the robustness of these models in various environmental contexts [74]. Transferable models can reduce the need for extensive labelled data and expert supervision in new environments, making them ideal for broad-scale implementation [89]. However, the limited transferability of current detection techniques across different environments remains a significant challenge for real-world applications [48]. For instance, estimating rhodamine concentration typically requires in situ calibration measurements from each location [107]. This requirement constrains the method’s generalizability and limits its usability across diverse geographic regions, highlighting the need for more adaptable, site-independent solutions.

Another significant challenge in environmental studies is the scarcity of labelled data, which is crucial for training supervised machine learning models [108]. Labelling hyperspectral data is time-consuming and resource-intensive, often requiring expert knowledge to interpret complex spectral information accurately [78]. This process is particularly challenging in remote or hazardous locations, such as the open ocean, where field validation is

logistically difficult and costly [47]. AI methods significantly reduced manual effort and increased adaptability, extracting more detailed information from the data for interpretation, which surpasses the capabilities of visual analysis and algebra-based methods in handling complex environmental conditions [69]. Still, most algorithms lack the generalizability needed to perform reliably across diverse environmental conditions [109]. Supervised learning models typically depend on large, labelled datasets to achieve high accuracy, but the limited availability of such data hinders their effectiveness across various scenarios [70, 108]. Integrating unsupervised learning techniques, which do not require labelled data, has allowed algorithms to learn directly from data patterns and distributions [81]. However, these methods still face challenges with the high variability of natural environments, which can result in detection inconsistencies [110]. For instance, in turbid or optically shallow waters, where the bottom reflects light, the surface spectral signature received can be altered, complicating accurate interpretation and detection [38, 107].

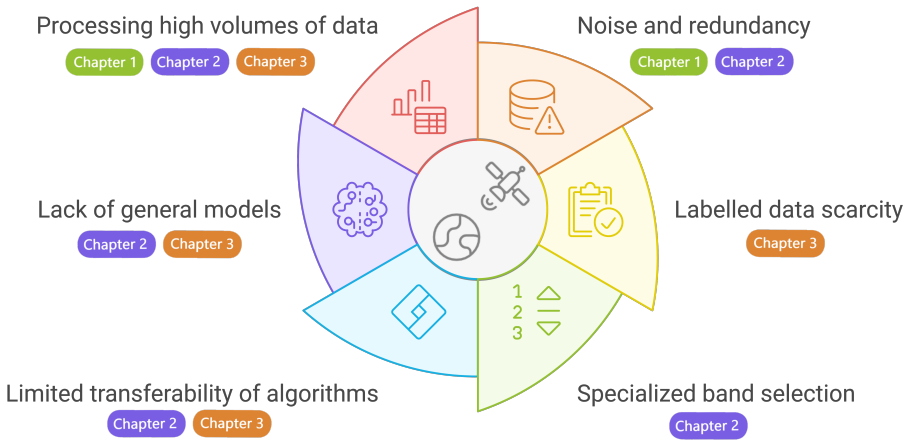


Figure 1.6: HSI challenges faced in the thesis.

These interconnected challenges shown in Figure 1.6—high data complexity and volume, limited model transferability across diverse environments, and scarcity of labelled data—significantly hinder the standardization of HSI models for environmental monitoring. Overcoming these barriers is essential not only to enable large-scale and efficient Earth observation but also to enhance informed decision-making in environmental management. Scalable and generalizable HSI solutions will support data-driven responses to environmental crises and guide the development of targeted policies, ultimately contributing to environmental preservation.

1.3 Objectives

This thesis aims to overcome the critical challenges of HSI that hinder large-scale systematic monitoring, thus contributing to Earth preservation. The main objective of this work is to develop a suite of transferable methodologies for pollutant detection in aquatic environments. To achieve the main goal, several specific sub-objectives have been outlined (Figure 1.7):

1. Present a novel spectral index to improve oil spill detection and facilitate a rapid response during an environmental crisis.
2. Develop a dimensionality reduction methodology that optimizes the spectral bands for water pollutant monitoring and improves the transferability of results across different environments.
3. Propose a new loss function for unsupervised neural networks to improve hyperspectral image processing.

The research in this thesis follows a clear progression. It starts with an analysis of how current remote sensing missions and available sensors can be leveraged to monitor pollution using established techniques such as spectral indexes. Building on this, it moves towards more advanced dimensionality reduction approaches to streamline data processing and enhance the adaptability of detection models across various environments. The final stage of the work expands the scope by investigating improvements to unsupervised AI-driven detection techniques, broadening the scalability of these methods.

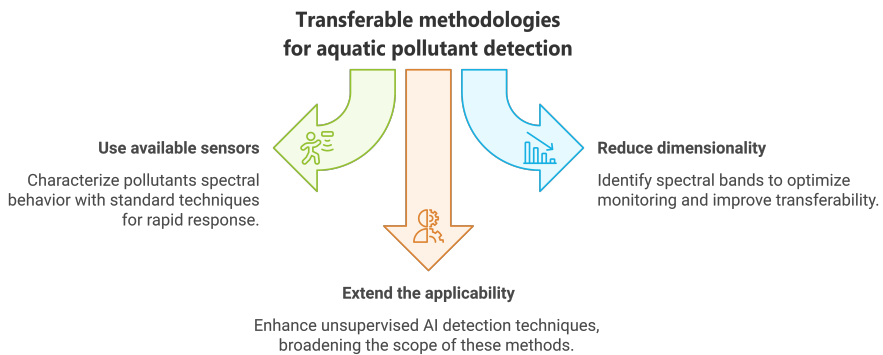


Figure 1.7: Main objective and sub-objectives of the thesis.

1.4 List of Publications

This thesis includes the following journal and conference articles:

2. Spectral Index to Reduce Misclassification in Oil Spill Detection

- 2.1** Á. Pérez-García, A. Rodríguez-Molina, E. Hernández and J. F. López, “Spectral Indices Survey for Oil Spill Detection in Coastal Areas,” *IEEE Journal of Selected Topics in Applied Earth Observations and Remote Sensing*, vol. 17, pp. 15359-15372, 2024. DOI: [10.1109/JSTARS.2024.3438123](https://doi.org/10.1109/JSTARS.2024.3438123)

3. Band Selection Method for Efficient Water Pollution Monitoring

- 3.1** Á. Pérez-García, T.H.M. van Emmerik, A. Mata, P.F. Tasserón and J. F. López, “Efficient plastic detection in coastal areas with selected spectral bands,” *Marine Pollution Bulletin*, vol. 207, p. 116914, 2024. DOI: [10.1016/j.marpolbul.2024.116914](https://doi.org/10.1016/j.marpolbul.2024.116914)
- 3.2** Á. Pérez-García, A. Martín Lorenzo, E. Hernández, A. Rodríguez-Molina, T.H.M. van Emmerik and J. F. López, “Developing a Generalizable Spectral Classifier for Rhodamine Detection in Aquatic Environments,” *Remote Sensing*, vol. 16, pp. 1-18, 2024, Art no. 3090. DOI: [10.3390/rs16163090](https://doi.org/10.3390/rs16163090)

4. Unsupervised Hyperspectral Methods for Scalable Monitoring

- 4.1** Á. Pérez-García, M. E. Paoletti, J. M. Haut and J. F. López, “Novel Spectral Loss Function for Unsupervised Hyperspectral Image Segmentation,” *IEEE Geoscience and Remote Sensing Letters*, vol. 20, pp. 1-5, 2023, Art no. 5506505. DOI: [10.1109/LGRS.2023.3288809](https://doi.org/10.1109/LGRS.2023.3288809).

Additional contributions that have not been included in the thesis are several publications in various journals (J) and conferences (C):

- J.1** J. M. Haut, S. Moreno-Alvarez, R. Pastor-Vargas, Á. Pérez-García and M. E. Paoletti, “Cloud-Based Analysis of Large-Scale Hyperspectral Imagery for Oil Spill Detection,” in *IEEE Journal of Selected Topics in Applied Earth Observations and Remote Sensing*, vol. 17, pp. 2461-2474, 2023. DOI: [10.1109/JSTARS.2023.3344022](https://doi.org/10.1109/JSTARS.2023.3344022)

- C.1** Á. Pérez-García, P. Horstrand and J. F. López, “Ndoi, A Novel Oil Spectral Index: Comparisons And Results,” *2022 12th Workshop on Hyperspectral Imaging and Signal Processing: Evolution in Remote Sensing (WHISPERS)*, Rome, Italy, 2022, pp. 1-5. DOI: [10.1109/WHISPERS56178.2022.9955062](https://doi.org/10.1109/WHISPERS56178.2022.9955062)
- C.2** Á. Pérez-García, A. M. Lorenzo and J. F. López, “Spectral Band Selection Methodology for Future Sensor Development,” *2024 47th MIPRO ICT and Electronics Convention (MIPRO)*, Opatija, Croatia, 2024, pp. 152-156. DOI: [10.1109/MIPRO60963.2024.10569699](https://doi.org/10.1109/MIPRO60963.2024.10569699)
- C.3** Á. Pérez-García, A. Rodríguez-Molina, E. Hernández, L. Vera and J. F. López, “Development of Low-Cost Multi-Spectral Cameras for Precision Agriculture,” *IGARSS 2023 - 2023 IEEE International Geoscience and Remote Sensing Symposium*, Pasadena, CA, USA, 2023, pp. 3466-3469. DOI: [10.1109/IGARSS52108.2023.10282072](https://doi.org/10.1109/IGARSS52108.2023.10282072)
- C.4** Á. Pérez-García, T. H. M. Van Emmerik, G. Amanda, M. Russwurm and J. F. López, “River Plastic Monitoring Workflow: From Satellite to Cloud Computing,” *MICRO 2024: Plastic Pollution From Macro to Nano*, Lanzarote, Spain, 2024, p. 1. DOI: sciencesconf.org/micro2024:552946

Table 1.1 provides a summary of the journal publications produced during the thesis, along with the key characteristics of each journal.

Table 1.1: Journal publications.

Reference	Editorial	Journal Name	Year	Impact Factor ⁽²⁰²³⁾	JCR Quartile
2.1	IEEE	JSTARS ¹	2024	4.7	Q1
3.1	Elsevier	Marine Pollution Bulletin	2024	5.3	Q1
3.2	MDPI	Remote Sensing	2024	4.2	Q1
4.1	IEEE	GRSL ²	2023	4.0	Q1
J.1	IEEE	JSTARS	2023	4.7	Q1

¹ JSTARS: Journal of Selected Topics in Applied Earth Observations and Remote Sensing

² GRSL: Geoscience and Remote Sensing Letters

1.5 Justification of the Thematic Unit

This thesis revolves around the critical environmental challenge of aquatic pollution and provides new resilient methods favouring generalization to diverse environments [2, 7, 8]. It addresses essential HSI challenges for environmental monitoring, such as data volume and complexity and the need for rapid and global pollutant detection. By developing a novel spectral index, proposing a band reduction methodology, and presenting a new loss function for

unsupervised methods, this thesis provides solutions that optimize available optical sensors, minimizing data processing requirements without compromising accuracy. The three chapters are closely interconnected and contribute to the overarching goal of developing efficient and transferable methods for pollution monitoring. Each chapter complements the others by tackling different aspects of this challenge.

Chapter 2 introduces the development of a new spectral index for fast oil spill detection. The *Normalized Difference Oil Index (NDOI)* reduces misclassification, particularly in distinguishing oil from sand in suspension, and it's more straightforward to calculate than other spectral indices. Furthermore, since spectral indices are based on a mathematical combination of bands, they involve significantly lower computational costs than AI algorithms, which is crucial for quick responses. This chapter directly supports the thesis's first sub-objective, improving oil spill detection to rapidly and accurately identify aquatic pollutants during environmental crises. These techniques lay the groundwork for practical, real-time monitoring systems that respond swiftly to oil spills. This innovation is particularly vital for environments where speed and accuracy are paramount.

Chapter 3 builds on this foundation by addressing hyperspectral data's high dimensionality and complexity, which hinders model transfer. A new dimensionality reduction methodology combines feature selectors and classifiers to identify the most influential bands for detecting specific contaminants. The research indicates that even by reducing the number of bands to four, high detection accuracy can be maintained for pollutants such as plastics or dye traces like rhodamine. Thus, this chapter supports the second sub-objective: optimizing the number of spectral bands to improve the efficiency and adaptability of detection methods across various environments. The chapter highlights how reducing data complexity while maintaining detection accuracy is essential for generalizing detection models. This work also demonstrates the transferability of spectral bands, which is critical for creating cost-effective multispectral sensors that can be tailored to specific pollutants.

Finally, **Chapter 4** explores unsupervised AI techniques, an essential approach when labelled data is scarce or unavailable. This chapter introduces a novel spectral loss function that enhances the performance of unsupervised neural networks, allowing them to classify HSI based solely on spectral characteristics. This methodology is evaluated on the Deepwater Horizon disaster in the Gulf of Mexico 2010, demonstrating that unsupervised models with this spectral loss function can rival traditional methods like spectral indices. This addresses the third sub-objective of the thesis, improving unsupervised neural networks. Introducing a novel spectral loss function enhances the performance of unsupervised models, allowing for accurate pollution detection in large-scale environments without the need for costly data annotation.

Together, these three chapters form a cohesive suite of methods that progressively advances the monitoring of aquatic pollution using HSI through robust and transferable models. The techniques developed in each chapter complement one another: the NDOI offers rapid, computationally light detection; the band selection techniques reduce data complexity while enhancing adaptability; and the unsupervised methods tackle the challenge of labelled data scarcity. The outcomes of this research have direct implications for the design of next-generation sensors, particularly those intended for specialized camera systems on UAVs or future space missions, where data efficiency and operational precision are crucial. This integrated approach ensures that the proposed solutions are optimized for specific circumstances while also being transferable, thus rendering them suitable for large-scale environmental monitoring.

1.6 Fundings

Pre-doctoral fellowship

This doctoral thesis was conducted while the author was beneficiary of a predoctoral grant given by the “Agencia Canaria de Investigacion, Innovacion y Sociedad de la Informacion (ACIISI)” of the “Consejería de Universidades, Ciencia e Innovación y Cultura”, part-financed by the European Social Fund Plus (FSE+) “Programa Operativo Integrado de Canarias 2021-2027, Eje 3 Tema Prioritario 74 (85%)”, with the ID TESIS2021010059.

Research projects

- **PERSEO** (CPP2021-008527): “Plataforma Aérea Autónoma Solar para la Monitorización de Eventos Contaminantes en el Ecosistema Marino,” is funded by the 2021 Public-Private Collaboration program of the Spanish State Plan for Scientific, Technical, and Innovation Research 2021-2023, as published in Order CIN/1502/2021. The participating entities are the Instituto Universitario de Microelectrónica Aplicada (IUMA) at the Universidad de Las Palmas de Gran Canaria, Instituto Tecnológico de Energías Renovables (ITER), Plataforma Oceánica de Canarias (PLOCAN), and Elittoral S.L. The project runs from October 1, 2022, to October 31, 2025, with a grant amount of 654.779,7€. The author characterized the optical properties of various pollutants and designed AI algorithms to enhance their automatic detection.
- **APOGEO** (MAC2/1.1B/226): “Precision Agriculture for the Improvement of Viticulture in Macaronesia” is funded by the European Commission and the European Regional Development Fund

(FEDER). The participating entities are the Instituto Universitario de Microelectrónica Aplicada (IUMA) at the Universidad de Las Palmas de Gran Canaria, Instituto de Productos Naturales y Agrobiología (IPNA) at the Consejo Superior de Investigaciones Científicas, Banco de Germoplasma, ISOPlexis at the Universidad de Madeira, Dirección General de Agricultura, Gobierno de Canarias of the Cabildo Insular de Gran Canaria, and Cabildo Insular de La Palma. The project runs from November 1, 2019, to October 31, 2023, with a grant amount of 977.357,89€. The author investigated the VNIR spectral response of different vineyards and applied spectral indices to assess their health.

- **TALENT-HExPERIA** (PID2020-116417RB-C42): “HypErsPEctRal Imaging for Artificial intelligence applications”, a subproject of TALENT, is funded by the Ministry of Science and Innovation of the Government of Spain. The participating entities are the Universidad de Las Palmas de Gran Canaria, Universidad Politécnica de Madrid, Universidad de Castilla La Mancha, and Universidad de Cantabria. The project runs from September 1, 2021, to August 31, 2024, with a grant amount of 175.813,00€ for the subproject. The author contributed to the characterization of the spectral response of various pollutants and developed a band selection system to optimize their detection.
- **PTOLOMEO**: “Plataforma de baja altitud para la observación autónoma del medio marino mediante tecnologías térmicas y ópticas”, is funded by the Cabildo Insular de Gran Canaria (Resolution No. 12/22, dated April 20, 2022). The participating entities are the Instituto Universitario de Microelectrónica Aplicada (IUMA) at the Universidad de Las Palmas de Gran Canaria. The project runs from June 13, 2022, to July 31, 2023, with a grant amount of 16.558,88€. The author created a new loss function to improve the learning process of unsupervised neural networks.
- **CubeSat** (C2022/158): “Tecnología Cubesat para la Observación del Medio Marino” is funded by the “Sociedad de Promoción Económica de Gran Canaria” (SPEGC) of the Cabildo Insular de Gran Canaria and managed by “Fundación Parque Científico Tecnológico” of the Universidad de Las Palmas de Gran Canaria. The project runs throughout 2023, with a grant amount of 39.800,00€. The author identified the spectral bands to be measured by the CubeSat sensor to study different water quality parameters.
- **OASIS-HARMONIE** (PID2023-148285OB-C43): “Open AI-driven Stack for enhanced HPEC platforms in Integrated Systems”, a subproject of OASIS, is funded by the Ministry of Science and Innovation of the

Government of Spain. The participating entities are the Universidad de Las Palmas de Gran Canaria, Universidad Politécnica de Madrid, Universidad de Castilla La Mancha, and Universidad de Cantabria. The project runs from September 1, 2024, to August 31, 2027, with a grant amount of 100.000,00€ for the subproject. The author plans to explore new large-scale Earth observation techniques to improve the monitoring of extensive areas.

- **SIROCO** (CPP2023-010858): “Sistema predictivo de presencia de residuos ambientales y corrosión en la superficie de los módulos y sistema estructural de plantas fotovoltaicas, mediante procesamiento automático de imagen térmica e hiperespectral,” is funded by the 2023 Public-Private Collaboration program of the Spanish State Plan for Scientific, Technical, and Innovation Research 2021-2023, as published in Order CIN/1025/2022. The participating entities are the Instituto Universitario de Microelectrónica Aplicada (IUMA) at the Universidad de Las Palmas de Gran Canaria, Instituto Tecnológico de Energías Renovables (ITER), and Fundación Instituto Tecnológico de Galicia. The project runs from December 2, 2024, to December 31, 2027, with a grant amount of 800.171,75€. The author will assist in spectrally characterizing corrosion in various materials and optimize the selection of bands for detecting it.

Other funding support

- **Research network REINFORCED+**: The autor is a member of the National Research Network for Mobile Robotics and Artificial Intelligence for Aquatic Ecosystems Monitoring (REINFORCED+) research network, funded by the Ministry of Science, Innovation and Universities and the State Research Agency of Spain under the “Redes de Investigación 2022” call [111].
- **Invited talk** at the “Drone: Applications in Various Fields” symposium at Wageningen University and Research. The university covered all travel and accommodation expenses for the author to give the talk.
- **ERASMUS+ 2022/2023** to undertake a two and a half month stay at Wageningen University and Research in the Netherlands.
- **ERASMUS+ 2023/2024** to undertake a two month stay at Wageningen University and Research in the Netherlands.
- **ACIISI** (*Agencia Canaria de Investigación, Innovación y Sociedad de la Información*) grant for a short stay in Spain and abroad as part of an official doctoral programme in the Canary Islands, co-financed by the

European Social Fund Plus for the year 2024. A short research stay of one week to continue with previous investigations at Wageningen University and Research.

- **ULPGC:** Grants for developing a research career at ULPGC, *Ayudas para el desarrollo de la carrera investigadora en la ULPGC*, corresponding to the academic year 2021-2022. Attendance at the ESA Living Planet Symposium [112, 113] international conferences.
- **ULPGC:** Grants for developing a research career at ULPGC, corresponding to the academic year 2022-2023. Attendance at the EDUNINE 2023 (VII IEEE World Engineering Education Conference) [114, 115].
- **ULPGC:** Grants for developing a research career at ULPGC, corresponding to the academic year 2023-2024. Attendance at the MIPRO 2024 (47th ICT and Electronics Convention) [116].
- **ULPGC:** Payment support for scientific publications corresponding to the academic year 2024-2025. Article entitled “Spectral Indices Survey for Oil Spill Detection in Coastal Areas” [61].

Chapter 2

Spectral Indices to Reduce Misclassification in Oil Spill Detection

The detection and characterization of marine pollutants, particularly oil spills, have become critical in responding to environmental crises in coastal areas. Spectral remote sensing techniques offer a powerful means of monitoring these pollutants. One of the main challenges in oil spill detection is accurately distinguishing the spectral behaviour of oil from other substances in the water, such as suspended sediments or vegetation, which can lead to misclassification and delayed response times during a crisis.

This chapter addresses Sub-objective 1 of the thesis, which aims to improve oil spill detection with spectral indexes, facilitating a rapid response during an environmental crisis. Although several spectral indices are available for detecting oil spills, many are limited by their tendency to misclassify suspended sand as pollution, leading to inaccurate detection. The author proposed the Normalized Difference Oil Index (NDOI) to overcome this issue in the conference paper **C.1** “NDOI, A Novel Oil Spectral Index: Comparisons and Results”. This new spectral index significantly reduces the misclassification of sand, improving detection accuracy and monitoring of oil spills in coastal areas.

Section **2.1**, “Spectral Indices Survey for Oil Spill Detection in Coastal Areas”, evaluates various spectral indices and their effectiveness in detecting oil spills. Its performance has been analyzed by employing different satellites and estimating the spill’s thickness and volume. By providing a more apparent spectral distinction between oil and other features like suspended sand and using two bands in the VNIR range, NDOI is a more suitable mechanism for fast oil spill detection and response. This survey highlights the strengths and weaknesses of different approaches, reinforcing the need for robust, cost-effective and adaptable spectral tools like NDOI.

2.1 Spectral Indices Survey for Oil Spill Detection in Coastal Areas

- **Á. Pérez-García**, A. Rodríguez-Molina, E. Hernández and J. F. López, “Spectral Indices Survey for Oil Spill Detection in Coastal Areas,” *IEEE Journal of Selected Topics in Applied Earth Observations and Remote Sensing*, vol. 17, pp. 15359-15372, 2024. DOI: [10.1109/JSTARS.2024.3438123](https://doi.org/10.1109/JSTARS.2024.3438123)
- Publisher: IEEE.
- Print ISSN: 1939-1404 (Electronic ISSN: 2151-1535).
- Journal metrics:
 - 2023 Journal Impact Factor: 4.7.
 - Journal Citation Indicator (JCI): 1.13.
 - Rank by Journal Impact Factor:
 - * **Q1**: Engineering, Electrical & Electronic; Remote Sensing; Imaging Science & Photographic Technology; Geography, Physical.

Spectral Indices Survey for Oil Spill Detection in Coastal Areas

Ámbar Pérez-García , Graduate Student Member, IEEE, Adrián Rodríguez-Molina , Emma Hernández, and José Fco López 

Abstract—When oil spills occur at sea, effective detection and monitoring are required to establish a successful response plan, and remote sensing emerges as an appropriate technology to support this process. Furthermore, Earth observation is progressively relying on low-cost multispectral sensors developed for monitoring particular features across various scenarios. However, despite these advancements, the ongoing challenge lies in reducing computational costs, resource requirements, and energy consumption. This work aims to select the spectral index that best detects coastal spills among those documented. The long-term goal is to develop a low-cost multispectral sensor with suitable bands. For this purpose, this study uses data from different sensors that acquired data of the Deepwater Horizon accident in the Gulf of Mexico. The confusion matrices, accuracy, and F1-score generated from the kNN pixel classification based on the indices values are measures of its performance. For this study, the recently introduced normalized difference oil index (NDOI) proves to be the best option for identifying coastal spills since it minimizes the false positives related to suspended sand and is quick to calculate. In addition, it has demonstrated that it helps distinguish different spill thicknesses and estimates the oil volume. Therefore, future research will focus on developing and validating a low-cost multispectral system that uses the NDOI bands to detect spills.

Index Terms—Hyperspectral images (HSIs), oil spill, remote sensing (RS), spectral indices.

I. INTRODUCTION

THE marine environment supports a diverse range of sea life that is extremely important for global biodiversity and quality of life, including climate regulation. Oil spills devastate marine and coastal environments, poisoning and suffocating

marine wildlife, accumulating on the seafloor and beaches, and causing long-term environmental impacts. Remote sensing (RS) and spectral technology are valuable tools for monitoring oil spills and assessing clean-up. However, there are still limitations in processing speed and, therefore, response time. Spectral indices offer a swift response with minimal computational overhead, rendering them a valuable and efficient approximation. This comparative study is noteworthy as it assesses the performance of existing indices and explores their limitations, making it a valuable contribution to the field.

Tanker accidents, refineries, offshore platforms, and minor maritime operations produce tons of crude and oil products that reach the sea yearly [1]. The most common causes of spills are oil exploration, pipeline leaks, and crude oil transfer to tankers. Still, they are also caused by illegal oil extraction or natural causes such as earthquakes or hurricanes [2]. The conventional method for measuring marine pollution before the 1960s was to sail into polluted regions, take in situ measurements at different depths, and then examine them in laboratories to determine water properties. This way, precise results are obtained but at a high cost in terms of human and material resources. Besides, this approach is very time-consuming and is geographically limited due to the inability to survey broad areas [3]. Aircraft and coastguard forces were introduced to improve ocean surveillance. Simple photography and video at short distances are examples of this. However, data acquisition costs remain high for larger areas [4].

Satellite and aerial RS have proven to be adequate tools for detecting and mapping marine pollutants, providing valuable data for time-evolution modeling to track contaminants through space and time [3]. When monitoring large areas, satellites are more efficient than aircraft as they can cover more extensive regions. Hence, they are used to detect spills and lead to a timely response to the incident. Airborne sensors can then conduct exhaustive monitoring, quantify the scale of the disaster, and identify the type of pollutant [5]. In recent years, uncrewed aerial vehicles (UAVs) have become vital in RS, offering high flexibility and resolution for rapid real-time data collection, but face challenges like accurate geo-referencing and real-time processing of hyperspectral images [6]. Therefore, given its broad coverage, satellite monitoring emerges as the optimal choice for oil spill detection.

It is crucial to remember that not all sensors are equally effective because each spectral range has advantages and disadvantages for a specific scenario. Although synthetic aperture radar (SAR) sensors are frequently used for the detection of

Manuscript received 13 March 2024; revised 2 June 2024; accepted 30 July 2024. Date of publication 5 August 2024; date of current version 5 September 2024. The work of Ámbar Pérez-García was supported by “Agencia Canaria de Investigación, Innovación y Sociedad de la Información (ACIISI)” of the “Consejería de Universidades, Ciencia e Innovación y Cultura”, the European Social Fund Plus (FSE+) “Programa Operativo Integrado de Canarias 2021-2027, Eje 3 Tema Prioritario 74 (85%)” under a predoctoral grant. The work of Adrián Rodríguez-Molina and Emma Hernández was supported by the “Vicerrectorado de Investigación y Transferencia de la Universidad de las Palmas de Gran Canaria” under a predoctoral grant during the research. We would also like to thank the TALENT-HEXPERIA project, under contract PID2020-116417RB-C42, the PERSEO project, under contract CPP2021-008527, from “Programa de Colaboración Público-Privada” of “Gobierno de España”, 2023-2025, and the OASIS-HARMONIE project, under contract PID2023-148285OB-C43 from “Proyectos de Generación de Conocimiento” 2023. (Corresponding author: Ámbar Pérez-García.)

The authors are with the Institute for Applied Microelectronics, University of Las Palmas de Gran Canaria, 35001 Las Palmas, Spain (e-mail: ambar.perez@ulpgc.es).

Digital Object Identifier 10.1109/JSTARS.2024.3438123

spillages, over the past decade, optical sensors have outperformed SAR in certain aspects of spill monitoring [7]. Part of this improvement is attributed to the proliferation of multispectral and hyperspectral sensors onboard satellites, which offer unprecedented spectral analysis of scenarios. Progress has also been made in developing low-cost multispectral sensors specialized in monitoring and characterizing a particular surface or features [8], [9], [10]. Optical sensors are a more suitable alternative than radar sensors for continuous monitoring due to their higher repetition time. This advantage stems from the greater presence of optical sensors onboard satellites, resulting in a higher repetition time for optical information from different sensors that can be combined. Optical sensor satellites guarantee a short revisit period, minutes for geostationary satellites, and a few hours for low Earth orbiting polar satellites. Instead, SAR satellites may require dozens of days to revisit midlatitude regions [11].

Multispectral and hyperspectral sensors can capture spectral signature-based 3-D images that provide valuable information about the composition of the surface studied in each pixel. A key feature in the optical detection of oil spills is that under sunglint, they might appear differently in shape, color, and contrast between light and dark [12]. The spectral signature of the spill varies with oil properties, the film thickness, its degree of evaporation, and the meteorological conditions such as sun illumination and air-water content [13]. It is possible to estimate the thickness of oil slicks with optical sensors [14]. Furthermore, due to their capacity to identify the chemical composition in detail and assess its abundance [15], high-spectral resolution sensors can differentiate false positives [5], distinguish oil types [16], [17], and quantify oil volume [18], [19], [20].

Several studies involve machine learning and neural networks (NNs) on high-precision maritime pollution detection with optical and radar sensors [21], [22], [23]. Although some AI methods discriminate between oil-contaminated and nonpolluted regions [24], [25], they are slower than performing a few mathematical operations such as spectral indices. The simplicity, dimensional reduction of the data to be processed, and the calculation speed of spectral indices are significant advantages over machine learning techniques. Furthermore, implementing spectral indices into hardware acceleration devices like graphics processing units (GPUs) and field programmable gate arrays (FPGAs) allows for parallel operations, further reducing processing time and energy consumed. Spectral indices become vital for monitoring in quasi-real-time, especially when working with hyperspectral sensors with hundreds of bands, and a short response time is required, for example, in a spill accident at sea [26].

The Deepwater Horizon (DWH) event-related hyperspectral and multispectral data are the focus of this investigation. The DWH oil spill, also known as the Gulf of Mexico oil spill, started on April 20, 2010, and discharged 780 000 m^3 of oil into the northern Gulf of Mexico for nearly three months [27]. When a spill such as the DWH happens, affecting a large coastal area and lasting for months, response teams cannot efficiently assess and contain all the damage. Thus, RS is crucial in decision-making. The long duration of the DWH event allowed scientists to collect data from a wide range of platforms and sensors, varying

from SAR to optical sensors in the visible and thermal ranges, including multispectral and hyperspectral sensors, both onboard satellites and aircraft [28]. Thus, DWH marked a turning point in developing techniques and algorithms for oil spill monitoring and response.

This work arises from the interest in developing a low-cost multispectral sensor to monitor oil spills along coastlines. Based on the spectral indices, the sensor can be designed with just the essential bands, considerably decreasing cost and enhancing the accessibility of this technology. Therefore, this study aims to select the most suitable spectral index to build such a sensor. For this purpose, a survey of the spectral index documented in the literature that can identify oil spills at sea is presented, along with a section on the distinction of spill thickness and oil volume based on prior works. Due to the difficulty of accessing regions of the ocean contaminated by an oil spill, the cost associated with measuring it, and the hence, they are used to detect spills and rapidly change the event, obtaining ground truth for the images above is challenging. Therefore, relevant pixels are carefully hand-picked from the image and labeled with the region to which they belong. The recently introduced normalized difference oil index (NDOI) [29] has given the best results of the study, with an overall accuracy of 94.5%, and has proven valuable in differentiating oil-in-water spill thicknesses and volume.

II. STATE OF THE ART OF SPECTRAL INDICES FOR OIL SPILL DETECTION

Solar radiation travels through the atmosphere before it is reflected on Earth's surface and reaches the sensor. Therefore, optical RS produces images from the radiation emerging from the Earth's surface-atmosphere system in the direction of observation of the sensor. The intensity of the radiant flux for a given surface and a given wavelength is a physical quantity measured in watts per squared meter steradian ($W/(sr.m^2)$). As this quantity is susceptible to atmospheric disturbances, reflectance—defined as the ratio of the emitted surface flux to the incident flux—obtained after atmospheric correction is used [30]. The spectral reflectance signatures help to distinguish the targets because each material reflects and absorbs light differently for each wavelength. The interaction between electromagnetic waves and water depends on the optical properties of water, absorption, and scattering, which alter its reflectance. This response—captured by remote sensors—is strongly linked to the concentrations, types, and presence of substances in water [31]. RS is crucial in monitoring spills at sea. Hyperspectral sensors with superior spectral and spatial resolution facilitate the discrimination of false positives, and the identification of oil type [32]. However, the high dimension of the hyperspectral and multispectral images complicates their storage and processing. Furthermore, the high correlation of bands decreases the efficiency and accuracy of its analysis and classification [33]. The most relevant bands for the study are selected to solve this data volume problem.

Spectral indices are combinations of bands by simple arithmetic operations to highlight some spectral behavior and suppress the background. The band choice depends on the spectral

TABLE I
MOST CITED INDICES FOR IDENTIFYING SPILLS

Index	Equation	Measured property	Author
NDOI	$(R_{599} - R_{870}) / (R_{599} + R_{870})$	Oil fluorescent characteristics	[29]
RAI	$(\text{Blue} - \text{IR}) / (\text{Blue} + \text{IR}) \sqrt{\sum_{i=1}^N b_i^2}$	Oil fluorescent characteristics	[36]
FI	$(\text{Blue} - \text{Red}) / (\text{Blue} + \text{Red})$	Oil fluorescent characteristics	[36]
HI	$(\lambda_{1729} - \lambda_{1705}) \frac{R_{1741} - R_{1705}}{\lambda_{1741} - \lambda_{1705}} + (R_{1705} - R_{1729})$	Oil-affected soils	[37]
OSI	$(DN_{\lambda_{Red}} - DN_{\lambda_{Yellow}}) / (\lambda_{Red} - \lambda_{Yellow})$	Existence of crude oil	[38]
WAF	$(R_{1343} + R_{1563}) / 2 - R_{1453}$	Seawater characteristics	[39]
CDOM	R_{565} / R_{660}	Seawater characteristics	[40]
CHL	$\log(\max(R_{433,490,510}) / R_{555})$	Surface chlorophyll <i>a</i>	[41]
NDVI	$(\text{NIR} - \text{Red}) / (\text{NIR} + \text{Red})$	Live green vegetation	[42]
NDWI	$(R_{860} - R_{1240}) / (R_{860} + R_{1240})$	Vegetation liquid water	[43]
Ratio B_2/B_{11}	Blue / R_{1614}	Oil presence	[44]

characteristics of the phenomenon under study. Oil spills can be found using a variety of thoroughly tested spectral indices. However, new and improved indices have recently been proposed that can be adapted to a specific satellite sensor image or a specific scene [34]. The pixel misclassification due to sand suspension on the coast is a weakness identified in most spectral indices in the literature [35]. Misclassification is a significant obstacle when spills occur in coastal areas. It makes the initial study of the oil spill, its follow-up, and the analysis of its long-term impact more difficult. Consequently, the NDOI—a new index that can mitigate this impact—was introduced [29].

The spectral index family commonly used to detect spills (see Table I) includes fluorescence index (FI) [36], rotation-absorption index (RAI), where *b* is the pixel radiance for the image band, [36], hydrogen index (HI) [37], and oil slope index (OSI) [38]. Seawater and vegetation indices are also included, such as water absorption feature (WAF) [39] and colored dissolved organic matter (CDOM) [40], or chlorophyll content (CHL) [41], normalized difference vegetation index (NDVI) [42], and normalized difference water index (NDWI) [43]. Band ratios are spectral indices where only two bands are used, partially normalizing the effect of clouds and shadows. Band ratios were born to improve the delineation accuracy provided by single-band pixels. This study will also use a custom ratio designed from Sentinel 2 bands to distinguish between polluted and clean water: ratio B_2/B_{11} [44]. Note that the wavelengths of the indices will not match exactly on all sensors, nor will it be possible to obtain all indices on all sensors due to the spectral ranges of each sensor. As airborne visible infrared imaging spectrometer (AVIRIS) covers the short-wave infrared (SWIR) range, it is possible to calculate spectral indices that are not possible with other sensors: HI, WAF, NDWI, and the ratio B_2/B_{11} .

Three types of spills can be distinguished spectrally by thickness: thin-film spills, thick-film spills, and emulsions (mixing of oil and seawater). Below 50 microns, the spots appear metallic, rainbow, or silver in color and are called sheens [45]. Thin-film

oil has a yellow–orange hue and appears in the vicinity of thick-film oil slicks, which is usually the result of its dispersion. These spots are typically discontinuous and irregular. They are generally between 50 and 200 microns thick. The color of crude oil, dark reddish-brown or black, is visible in thick-film spills [46]. These spots are commonly continuous and compact, with a thickness above 200 microns. Finally, emulsions are water-to-oil mixtures with a red-orange color that appear in the convergence zones of the waves and look like long, narrow bands of oil [47]. Its thickness is difficult to measure precisely but is higher than that of the thick-film oil, exceeding 500 microns.

As mentioned in Section I, although there are several limitations to detecting spills with optical imaging, its potential and applicability are indisputable [44]. In the case of shallow water spills, thin-film spills exhibit the same spectral behavior as the ocean floor [48]. However, in the open sea, it is easier to distinguish the optical characteristics of crude oil. Seawater influences thin oil films (sheens) due to its near translucency. On the contrary, the transparency of thick oil slicks is weak, so their spectra are weakly affected by seawater. Therefore, the hydrocarbon spectral indices (NDOI, FI, RAI, HI, and OSI) help identify emulsions and continuous thick slicks. By contrast, the water and vegetation spectral indices (WAF, CDOM, CHL, NDVI, and NDWI) are more suitable for detecting sheens and seawater [45]. Both are complementary, so their combination improves recognition accuracy. In general, sheens are more easily noticed at viewing directions near the sun-glint zone, while thick films are more likely to be identified at viewing angles away from the sun [49].

Oil weathering processes act on the spills produced on the sea surface, causing their spreading, evaporation, dissolution, emulsion, etc., thus, modifying the volume of oil in the slick. Processes such as evaporation remove much of the volatile parts, but emulsification of the spill with seawater can increase the oil volume [50]. This article uses the Bonn Agreement Oil Appearance Code [51], adopted as a standard method for assessing the volume of oil in water in 2004. It codes the thickness of the slicks

TABLE II
CHARACTERISTICS OF THE STUDY'S SENSORS

Parameter	AVIRIS	HICO	MERIS
Spatial resolution	20 m-1 m	90 m	300 m
Revisit period	—	3 days	3 days
Spectral range (nm)	VNIR-SWIR	VNIR	VNIR
Bandwidth	366–2496	353–1080	412–900
Number of bands	<10 nm	~ 6 nm	10 nm
Band units	224 bands	128 bands	15 bands
Operational	Radiance	LIB	TOA reflectance
Platform	1992–today	2009–2014	2002–2012
Organization	Airborne	ISS	Envisat Satellite
	NASA JPL	ONR and NASA	ESA

from 1-5 in order of increasing thickness for sheens (silver/gray), rainbow, metallic, discontinuous, and continuous true oil colors. The Bonn Agreement Oil Appearance Code does not provide a specific code for emulsions due to their thickness variability and, therefore, volume estimation complexity [51]. Oil sheens have a thickness between 0.04 and 0.3 microns, rainbow-colored slicks between 0.3 and 5.0 microns, metallic-looking slicks are typically between 5.0 and 50 microns, and discontinuous true-color oil slicks can reach up to 200 microns. Thicker thicknesses fit into continuous true-color oil slicks or emulsions, depending on how degraded the oil is by mixing with water.

III. MATERIALS AND METHODS

A. Datasets

In this work, two images from each sensor—AVIRIS, Hyperspectral Imager for the Coastal Ocean (HICO), and Medium Resolution Imaging Spectrometer (MERIS)—have been used to contrast the results of the spectral indices. Table II shows their technical characteristics.

The AVIRIS is an airborne instrument that measures upwelling spectral radiance in 224 contiguous bands at 10 nm intervals across a wavelength range from 366 to 2496 nm (VNIR and SWIR) [52]. NASA's Jet Propulsion Laboratory (JPL) designed and built the sensor in California. Data are available from 1992 to the present. The main objective of the AVIRIS project is to identify, measure, and monitor constituents of the Earth's surface and atmosphere based on molecular absorption and particle scattering signatures [53]. It has flown in four different aircraft. The width, length, and spatial resolution of the recorded images vary with the flight altitude of the vehicle. For example, when flying at an altitude of 20 km, scenes of 11 km in width and 800 km in length are obtained with a spatial resolution of 20 m. The HICO is the first space-borne imaging spectrometer designed to sample the coastal ocean. It was developed by the Naval Research Laboratory (NRL) for the Office of Naval Research (ONR) and later cofunded by NASA's International Space Station (ISS) Program. It was operational between 2009 and 2014. Its purpose was to provide data for coastal scientific research worldwide. The instrument can obtain 2000 scenes each year with a revisit period of approximately three days. HICO has 120 bands between 380 and 960 nm (VNIR) sampled at 5.7 nm, with a spatial resolution of 90 m and a high signal-to-noise ratio



Fig. 1. Geolocation of survey images in the Gulf of Mexico (source: Google Earth V 9.147.0.2).

to resolve the complexity of the coastal ocean [54]. This work uses images with an LIB (sensor units) processing level.

The MERIS was a programmable spectrometer on the European Space Agency (ESA) Envisat mission. Its primary goal was to measure the color of the ocean, although atmospheric and land surface studies were also carried out. MERIS was developed under the leadership of ALCATEL Space Industries and was in operation from 2002 to 2012. One of its most outstanding features was the programmability of its spectral bands in width and position, with 15 bands between 412 and 900 nm and a bandwidth of 10 nm. The images are in top-of-atmosphere (TOA) reflectance units, with a spatial resolution of up to 300 m and a revisit time of around three days [55].

B. Study Area

The DWH oil rig was in the Gulf of Mexico, 93 km southeast of the Mississippi River Delta. When it exploded, a considerable volume of crude oil leaked out [56]. Fig. 1 shows the area covered by each of the images in the study to give the reader an idea of the dimensions of the different sensors. The oil spill studied was between 26° and 30° north and 84° and 92° west. We concentrate exclusively on the region of the image that is of the utmost concern, as the oil spill presents all the characteristics that we consider relevant to the study. Given that this is a dynamic process, we have provided the dates and times of image acquisition (see Table III).

The selected set of images contains thick and thin oil spills to test the effectiveness of the spectral indices against slicks of different characteristics and thicknesses. It is important to note that most of the water surrounding the spillage contains a small part of diluted oil. The whole surface close to the thick stains suffers from this contamination. As this is a near-shore spill, some scenes also show sand suspended in the ocean. We have masked out the clouds in the images following a methodology proposed by [57] that allows us to ensure accurate cloud masking tailored to the specific characteristics of our images.

In the AVIRIS scenes (see Fig. 2), the oil can be seen with the naked eye in the RGB composition. In the image captured on May 17, different thicknesses of oil slicks can be distinguished, with several bright lines running across the bottom half of the

TABLE III
DATE OF THE CAPTURE OF THE STUDY IMAGES

Image	Date	Acquisition (UTC)	Image reference name
AVIRIS 1	May 17	20:46	f100517t01p00r11
AVIRIS 2	May 18	19:59	f100518t01p00r11
HICO 1	May 24	14:55	H2010144145510
HICO 2	May 28	13:21	H2010148132130
MERIS 1	April 26	15:56	ENV_ME_2_FRG_20100426T155651_20100426T160013_0202_088_498_DSI_R_NT_
MERIS 1	May 02	16:08	ENV_ME_2_FRG_20100502T160817_20100502T161126_0188_089_083_DSI_R_NT_

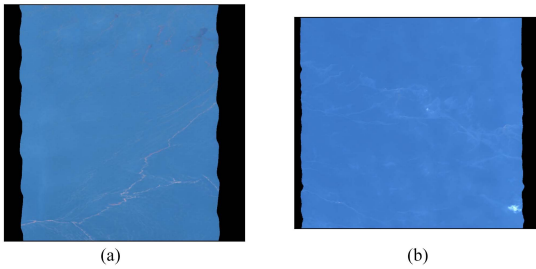


Fig. 2. AVIRIS true color RGB images from 17 May 2010, at 20:46 and 18 May 2010, at 19:59. (a) AVIRIS 1. (b) AVIRIS 2.



Fig. 3. HICO true color RGB images from 24 May 2010, at 14:55 and 28 May 2010, at 13:21. (a) HICO 1. (b) HICO 2.

figure, which correspond to an emulsion. There are also thick oil stains, seen as dark reddish rounded spots in the upper part of the image. In the May 18 image, traces of thin oil are faintly visible in a diagonal direction. There is also a tiny cloud in the lower right part. From now on, the AVIRIS image of 17 May 2010, will be called AVIRIS 1, and that of 18 May 2010, will be AVIRIS 2.

Regarding HICO images (see Fig. 3), in HICO 1, the one corresponding to May 24, the trail of sand in suspension from the Louisiana coast, specifically from the Mississippi River mouth, can be seen on the left side. On the right side of the image, there is also a faint vertical line of oil. In HICO 2, the one taken on May 28, practically no element can be seen, only the clouds in the bottom left corner.

Unlike the scenes shown, MERIS images cover a much larger land area at the cost of losing spatial resolution. The two images of Fig. 4—MERIS 1 and MERIS 2—cover the entire spill. In addition, both show different thicknesses of oil and part of the Mexican coastline. Thus, measuring the affected area and the thickness of the oil film at each point is more complicated. To highlight the spill-affected region effectively, we have masked

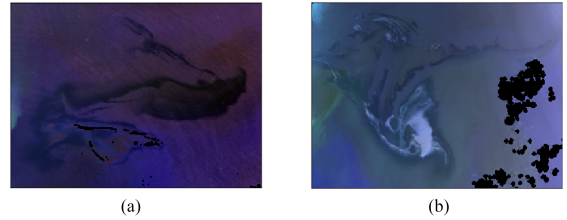


Fig. 4. MERIS false color RGB images from 26 April 2010, at 15:56 and 2 May 2010, at 16:08. (a) MERIS 1. (b) MERIS 2.

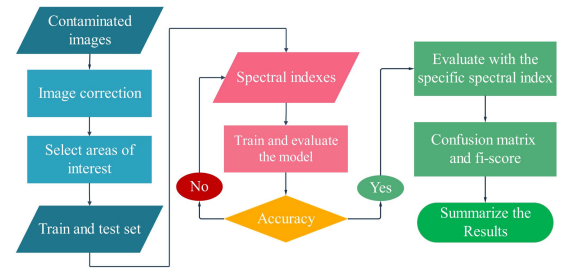


Fig. 5. Flowchart of the experimental process. Blue indicates the initial phase of data preparation, pink represents the algorithm’s training phase, and green denotes the final phase of analysis and presentation of results. The yellow diamond indicates a decision point.

the clouds and the coastline in the image since they exhibit higher reflectivity values than the oil spill area. Both MERIS scenes are affected by sunglint and are thus displayed in a false RGB to facilitate the differentiation of the polluting material. These present an opportunity to explore indices’ behavior and performance under sunglint.

It is interesting to note the rapid dispersal of the spill, deduced from its shape change between 26 April and 2 May. These underline how crucial it is that the clean-up teams and maritime authorities take immediate action.

C. Experimental Process

Fig. 5 provides a flowchart to facilitate the explanation of the experimental procedure. The process has three stages: the preprocessing of the images, the data processing and training of the computational model, and the result evaluation. Once the AVIRIS, HICO, and MERIS images have been selected and downloaded from the corresponding platforms [53], [54], [55], these must be corrected using the information provided in the

image metadata. If necessary, cloud masks are applied. Next, we select the areas of interest from the true-color or false-color images and, create the subsets train (70%) and test (30%) randomly. Although it is not possible to distinguish thicknesses in all the scenes, it is essential to ensure that all three subsets contain different thicknesses of oil slicks and are different from each other to obtain a consistent sample.

We employed the bands of the multispectral and hyperspectral images to calculate the corresponding spectral indices for oil detection and seawater composition. For each spectral index, pixels of the interest areas are extracted and used to train and test the computational kNN model. The kNN algorithm [58], [59] is a popular nonparametric classification method known to have significant classification performance and simple implementation. One of the keys to the success of this algorithm is the hyperparameter k , which allows the selection of the number of neighbors that influence the classification of a given pixel. Different values of k have been tested for the dataset, finding that from k equal to five, the improvement in the accuracy of the indices is insignificant. This method is efficient in classification problems with imbalanced class distributions, a situation in which our scenario is found, given that there are many more water pixels than spill pixels [60]. Combining the index's visual analysis with the calculation of model errors makes it possible to establish which are most effective in each scenario.

The confusion matrices produced by the classification, combined with its corresponding accuracy, F1-score metrics, and a figure of merit, γ , will be used to calculate the error. A confusion matrix illustrates the relationship between predicted and real labels, enabling assessing the classification model's quality. Accuracy is one of the most widely used and favored metrics in classification. It measures the percentage of correct predictions [61]. Moreover, the F1-score is particularly useful with uneven class distribution, giving more importance to smaller classes [62]. Finally, we introduce a figure of merit denoted as γ , which combines the results of the previous metrics

$$\gamma = \text{Accuracy} \cdot \frac{F1^{\text{Oil}}}{F1^{\text{Water}}} \quad (1)$$

where Accuracy is the overall accuracy [61], and $F1^{\text{Oil}}$ and $F1^{\text{Water}}$ denote the F1-scores [62] for the oil and water classes, γ encompasses the error metrics by weighing the accuracy with the ratio between the F1-scores of the oil and water classes. This approach enables γ to account for accuracy relative to the performance of unbalanced classes.

D. Validation

Oil spills at sea vary rapidly due to the movement of currents that disperse the oil and evaporation processes. These circumstances mean that measuring the composition and thickness of spillage in situ in all affected areas is complicated and costly in terms of time and resources. For these reasons, there is often no ground truth of spills against which to test the results of spectral indices and classification algorithms. We propose a technique to validate them based on the Bonn Agreement Oil Appearance Code [51]. To address the lack of ground truth, we hand-pick the

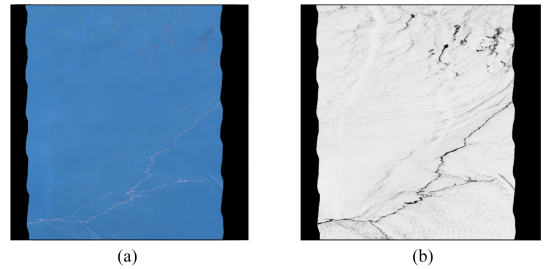


Fig. 6. AVIRIS true color RGB and NDOI from 17 May 2010, at 20:46. (a) AVIRIS 1. (b) NDOI.

pixels that belong to a class, label them, and shuffle them to build a training and test dataset with a sample ratio of 70/30. Second, we use the two sets to train the kNN algorithm and validate its result. These will provide a measure of the effectiveness of the indices. Although the kNN introduces a small error in the classification, the primary importance lies in the indices. So, if the values of a spectral index for a class are similar but different from other classes, we will achieve satisfactory results in the confusion matrix and error metrics.

The validation technique has been used both for evaluating the effectiveness of the indices and for verifying the performance of NDOI in estimating thicknesses and volumes of oil spills. For this purpose, two previous works will be taken as a reference [20], [45]. The authors estimated the thickness and oil volume with AVIRIS and MERIS imagery on dates close to those used in this work. Based on these results as the ground truth, we conducted tests to evaluate the effectiveness of the validation method and the spectral index's capability to estimate the oil spill's thickness and volume. The detailed results and analysis are presented in Section IV-D.

IV. EXPERIMENTAL RESULTS AND DISCUSSION

First, we performed a visual examination of the NDOI about the RGB representation for the representative image of each sensor to illustrate the index characteristics found in previous work [29], [35]. Next, we extend the study by performing a qualitative analysis of spectral indices from the literature for several scenes. Then, its performance is quantified using metric confusion matrices, precision, and F1-score. Finally, we test whether the NDOI can distinguish different thicknesses and volumes of oil at sea.

A. NDOI Qualitative Analysis

The first scene to be studied (see Fig. 6) is AVIRIS 1. This image is of great interest because it shows spots of different thicknesses. The naked eye can see how the NDOI index perfectly highlights the emulsion, which is noticeable in the RGB image as a narrow orange band of spill across it. It also reveals the thicker oil slicks, which can be observed in RGB as dark red-brown spots, although the darker part is not adequately identified. Thinner, discontinuous areas typically produced by the dispersion of an emulsion or thick patches are near them in a

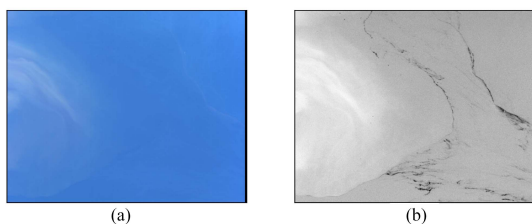


Fig. 7. HICO true color RGB and NDOI from 24 May 2010, at 14:55. (a) HICO 1. (b) NDOI.

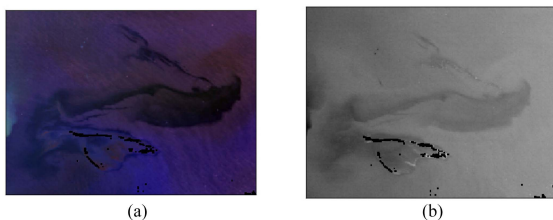


Fig. 8. MERIS false color RGB and NDOI from 26 April 2010, at 15:56. (a) MERIS 1. (b) NDOI.

softer tone. Fine stains appear as a faint, yellowish color in RGB, making them more difficult to discern. Thinner spots, known as sheens, are not detectable with the index—nor are they visible in RGB, as these are semitransparent, usually acquiring a metallic, rainbow, or silver color. It is worth noting that most of the ocean surface surrounding the spills is somehow tainted. Almost the entire surrounding region, unhighlighted by the spectral index (white color), is covered by a thin layer of oil. Because the spectral index can detect several different thicknesses in the AVIRIS image (emulsion, thick spot, and thin spot), it is to be expected that the NDOI can help infer spill thickness in a subsequent scene.

Apart from distinguishing the thickness of the spot, a crucially important aspect of a spectral index is its ability to discriminate look-alikes. As mentioned in Section II, most indices in the literature highlight the suspended sand as if it were part of the spill. This is a handicap in the study of coastal discharges. Fig. 7 shows HICO 1, where it is possible to identify sand from the delta produced by the Mississippi River on the left side. The NDOI index completely dismisses this suspended sand and accentuates the thin strands of the spill to the right of it. Thus, with this spectral index, the oil pathways are clearly defined.

Finally, it is relevant to underline how efficiently the index performs when treating the entire spill. When a slick of this magnitude is involved, the situation is often quite complex. Its characteristics can be subject to variations related to ocean currents or the composition of the water in which it travels. Although the new index does not highlight all the observable details in the false-color image (see Fig. 8), it indicates the thicker spill and the trajectories followed by the thinner spill strips. In this case, it is difficult to identify the complete slick using spectral indices due to its wide variety of spectral behavior

and the sunglint. However, NDOI can detect different mixtures of oil and seawater, which is intricately linked to the volume of oil (further explored in Section IV-D). More elaborate post-processing could be performed to classify regions of different characteristics. At first glance, the novel index distinguishes between three classes. The filament is highlighted in white, corresponding to an emulsion zone. The thick spill is marked in dark gray, and the sea in light gray. The following sections will test whether sunglint affects the ability of the indices to differentiate water from oil and to identify their characteristics.

Because the advanced synthetic aperture radar (ASAR) sensor is also on board the Envisat mission, it was possible to compare the data generated by the radar with the outcomes of the NDOI for MERIS in earlier work [35]. NDOI is said to be robust because its pattern matches the ASAR radar image captured on the same day.

Given the results, the implementation of the NDOI index is broadly satisfactory. We must now compare its effectiveness with the other spectral indices in the literature.

B. NDOI: A Comparative Study

Starting again with AVIRIS 1, Fig. 9 shows a compilation of the literature indices and the RGB image. At first glance, most indices present a similar pattern to that observed in NDOI. Specifically, both RAI, FI, and CDOM seem identical to NDOI. While RAI highlights fine oil slicks less than NDOI, CDOM enhances them more than NDOI. The B2/B11 ratio accurately detects the presence of oil, even highlighting areas with very thin spill thickness. The NDVI exhibits a similar structure to NDOI, though not as pronounced in the sheens. However, the index is inverted, highlighting the unpolluted area. Similarly, the HI and OSI are inverted. These indices only point to the thickest spill zone, the emulsions. The HI index shows banding because it involves AVIRIS bands with wavelengths longer than 1700 nm, in which the signal-to-noise ratio is poor. The WAF and NDWI indices also indicate the thicker regions of the spill. Only the emulsions are identified in the WAF case, whereas, in the case of NDWI, slightly thinner discharges are also discernible. Very thick spill parts that turn dark red or almost black have different spectral behavior and are difficult for the spectral indices to distinguish, except for NDWI and the B2/B11 ratio. Finally, the chlorophyll index, CHL, is the least clear. The emulsion's narrow lines are visible, and the thick spill spots are highlighted in white. However, the rest of the scene seems blurred, so the remaining oil is indistinguishable. It is possible that all indices are valid in certain aspects but are not equally efficient and do not provide the same results for different thickness.

Some indices cannot be determined with HICO since this sensor does not reach the shortwave infrared range: HI, WAF, NDWI, and ratio B2/B11. The most noticeable difference between the spectral indices shown in HICO 1 (see Fig. 10) is how they treat the suspended sand from the delta. As explained before, NDOI discards this sand completely, and the oil path is clearly defined, with two thin lines splitting the image. NDVI presents the same behavior but again inverted. The subsequent index with similar behavior is RAI. However, the two oil

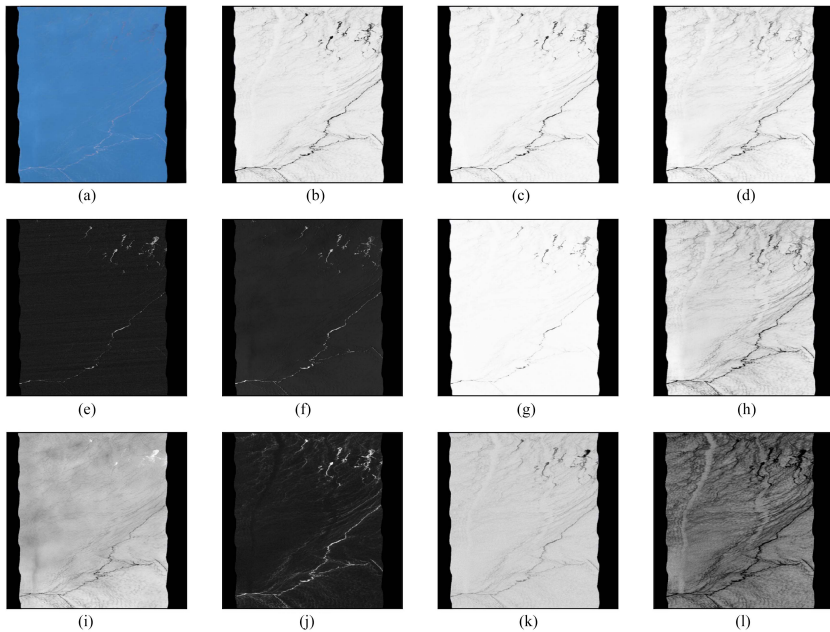


Fig. 9. AVIRIS true color RGB and spectral indices from 17 May 17 at 20:46. (a) RGB AVIRIS 1. (b) NDOI. (c) RAI. (d) FI. (e) HI. (f) OSI. (g) WAF. (h) CDOM. (i) CHL. (j) NDVI. (k) NDWI. (l) RATIO B2/B11.

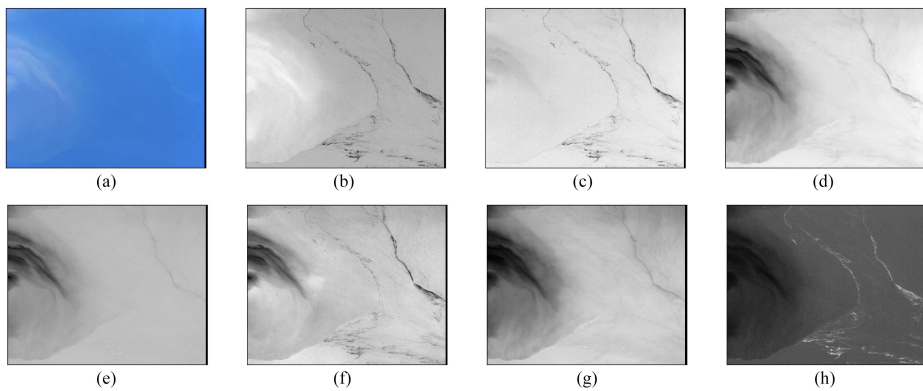


Fig. 10. HICO true color RGB and spectral indices from 24 May 2010, at 14:55. (a) RGB HICO 1. (b) NDOI. (c) RAI. (d) FI. (e) OSI. (f) CDOM. (g) CHL. (h) NDVI.

filaments are not as well defined, and some of the suspended sand could be mistaken for a sheen. The remaining indices mistakenly highlighted the sand in suspension as a spill. For CDOM, the line of the oil spill farthest from the delta can be seen, and the closer one can be intuited. For FI and CHL, just the most distant line from the mouth of the river can be distinguished. In the case of OSI, the oil spill is practically indistinguishable, with only the sand in suspension standing out.

As for HICO, MERIS does not cover the shortwave infrared. Consequently, HI, WAF, NDWI, and ratio B2/B11 cannot be applied either. Since MERIS images cover the entire spill and

the sunglint effect, some spectral behaviors in the image differ significantly from others, making analysis more challenging. Guided by the false-color composition in MERIS 1 (see Fig. 11), two oil cores appear in the discharge. One is at the lower left of the image (principal), and the other is centered on the right (secondary), joined by a strand, and a second strand rises from the secondary one. The principal oil cluster is less homogeneous, and changes in thickness are abrupt, while in the other core, these changes are gradual. Most spectral indices reveal an area of oil accumulation as a white filament in the left area of the image. It is dark in the NDVI but blends into the background in the CHL.

TABLE IV
ERROR METRICS FOR ASSESSING SPECTRAL INDICES

Index	Accuracy	Accuracy IQR	Oil F1-score	Water F1-score	γ
NDOI	0.945	0.044	0.830	0.961	0.816
Ratio B_2/B_{11}	0.921	0.079	0.832	0.948	0.808
RAI	0.940	0.054	0.812	0.957	0.797
NDVI	0.931	0.072	0.786	0.950	0.770
FI	0.955	0.060	0.779	0.968	0.768
NDWI	0.893	0.103	0.734	0.933	0.702
CDOM	0.870	0.140	0.711	0.881	0.702
WAF	0.882	0.116	0.710	0.926	0.677
OSI	0.865	0.056	0.618	0.894	0.593
CHL	0.862	0.082	0.601	0.896	0.578
HI	0.831	0.142	0.550	0.895	0.510

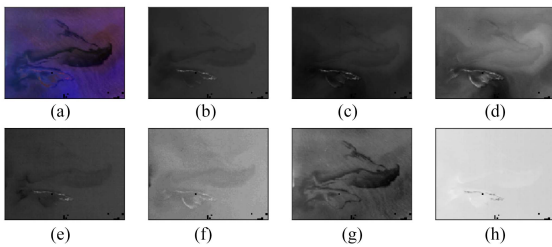


Fig. 11. MERIS false color RGB and spectral indices from 26 April 2010, at 15:58. (a) RGB MERIS 1. (b) NDOI. (c) RAI. (d) FI. (e) OSI. (f) CDOM. (g) CHL. (h) NDVI.

This behavior is probably a consequence of the solar illumination and oil thickness and causes the rest of the image to lose contrast. NDOI, RAI, and CDOM all show the entire silhouette of the spill, with NDOI being the clearest. In RAI, the second core has a lighter film around it, probably produced by sheens. These can be seen more clearly in FI, obstructing the distinction of the main spill. In OSI, the principal accumulation stands out more than the other one. NDVI shows a similar phenomenon, but in that case, it is more challenging to observe because of the stark contrast of the image with the highlighted filament. Finally, CHL has a different pattern from the rest. The right cluster is distinguishable, and the other has many undetected gaps. However, the overall silhouette is still distinguishable.

Fig. 12 shows the effect of masking this filament. The image contrast has improved, and the human eye perceives some spectral indices better. For example, in NDOI and NDVI, it is now possible to appreciate in more detail the spillage. Furthermore, the index indicates changes in spill thickness. This is a purely visual effect of facilitating interpretation, as the pixel values have not changed.

In conclusion, the thorough analysis of spectral indices from AVIRIS, HICO, and MERIS imagery has provided valuable insights into detecting and characterizing oil spills. This study reveals notable similarities and distinctions in the response of the spectral indices across different sensors and varying spill thicknesses. Challenges inherent in specific sensors, such as

the absence of shortwave infrared range in HICO and MERIS, underscore the importance of careful selection and understanding of sensor capabilities for accurate oil spill assessment. It is worth noting that a supplementary spectral analysis of AVIRIS 2, HICO 2, and MERIS 2 is presented in the Appendix, further contributing to the comprehensive understanding of oil spill detection. This qualitative exploration sets the stage for a subsequent quantitative study.

C. NDOI Quantitative Analysis

In addition to the visual analysis, a quantitative analysis of the spectral indices is necessary. For this purpose, we present the confusion matrices, the accuracy, and the F1-score.

Fig. 13 shows the normalized confusion matrices corresponding to the NDOI indices applied to the six spectral images. Most matrices are very close to the identity, thus, indicating the effectiveness of the spectral index, except for the AVIRIS 2 and the HICO 2 matrices. This is because there is almost no coarse spillage in the scenes, and the index cannot distinguish it. The remaining confusion matrices have reasonably high hit rates, exceeding 95% success rate, which is desirable for good quality indices. In some cases, even the totality of the water pixels is correctly classified. Generally, for all images, the precision obtained by the oil class is higher than its recall. The quality of the pixels classified as oil is high, but the number of pixels identified is lower.

The median accuracy and F1-score values for the oil and water classes, as well as the interquartile range (IQR) of the accuracy and γ for each spectral index, are presented in Table IV. The best performance for each metric is in bold. NDOI presents a good compromise among all these values, showing promising results. It has very high accuracy (0.945) along with FI (0.955) and RAI (0.940). Moreover, NDOI is the most compact index, as indicated by its low IQR—noting its robustness. However, accuracy can be misleading when evaluating spectral indices; classes are unbalanced when detecting oil slicks in the vast sea. Therefore, a very accurate result can be obtained associated with a high hit rate for the water class, independently of the hit rate of the oil class. To better understand the indices' performance in

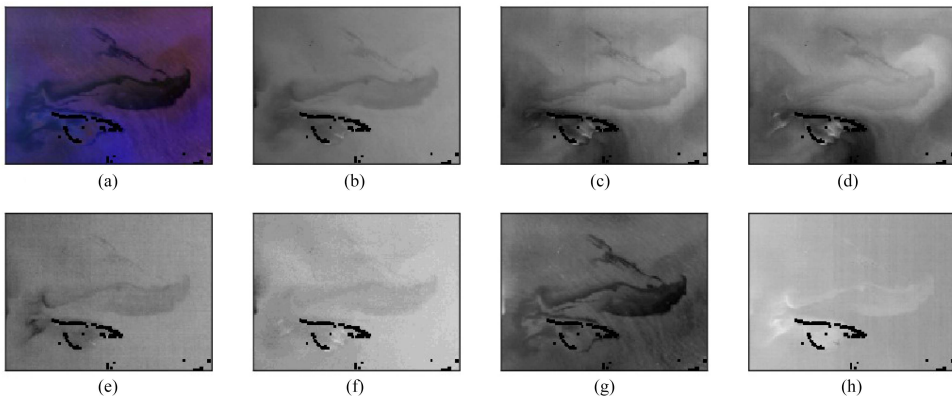


Fig. 12. MERIS false color RGB and spectral indices with masked glints from 26 April 2010, at 15:58. (a) RGB MERIS 1. (b) NDOI. (c) RAI. (d) FI. (e) OSI. (f) CDOM. (g) CHL. (h) NDVI.

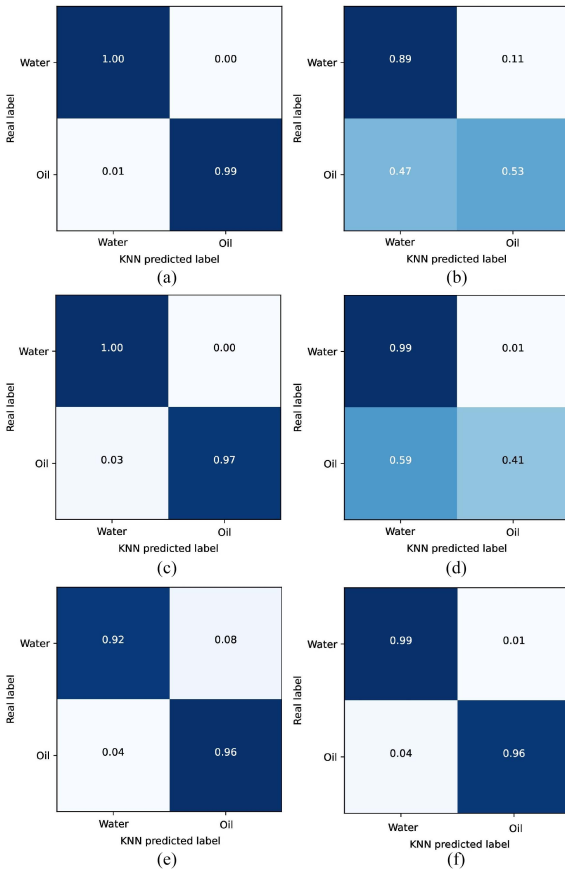


Fig. 13. Normalized confusion matrices of the NDOI spectral index for all spectral images. (a) AVIRIS 1. (b) AVIRIS 2. (c) HICO 1. (d) HICO 2. (e) MERIS 1. (f) MERIS 2.

detecting oil, we have examined the F1-score. This metric gives more importance to smaller classes, becoming more reliable in unbalanced situations. NDOI presents a water F1-score (0.961) that is very close to FI (0.968) and above RAI (0.957). But more relevant for our study, it has the second highest oil F1-score (0.830), which is the element that we want to monitor. NDOI oil F1-score value is after the B2/B11 ratio (0.832), followed by RAI (0.812). Lastly, NDOI shows the best result for γ (0.816), followed by ratio B2/B11 (0.808) and RAI (0.797). Acknowledging the potential bias in the results due to the inability to apply B2/B11, NDWI, HI, and WAF indices to HICO and MERIS is indispensable. The results in the overall accuracy of the best indices—FI, NDOI and RAI—are competitive with those obtained by AI techniques in similar oil spill studies. An accuracy of around 95% is attained with Random Forest (RF) and NN, and higher for support vector machine (SVM) operating directly on hyperspectral features and convolutional NNs [25].

In light of the above, NDOI has the best overall evaluation, as it has the second-best result in several metrics and the best in accuracy IQR and γ . In addition, the best value in the rest of the metrics does not correspond to a specific index but to several. RAI also has a very positive overall assessment, as it has obtained the third-best value in almost all metrics. However, the arithmetic operations involved in RAI calculation are computationally more expensive than in NDOI.

D. Thickness and Volume Differentiation

In this last section, the ability of NDOI to detect different thicknesses of spillage and volumes of oil is analyzed (see Fig. 14). For this purpose, two previous works will be taken as a reference [20], [45], where the authors estimate the thickness and oil volume with AVIRIS and MERIS imagery on dates very similar to those used in this work. Hence, the pixels for the training and test datasets are labeled using the outcomes of the studies as the ground truth. As already mentioned, the Bonn Agreement Oil

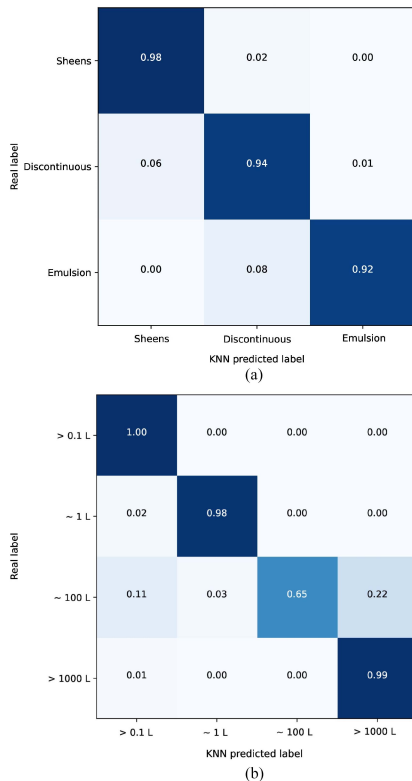


Fig. 14. Normalized confusion matrix of (a) spill thickness and of (b) the volume in liters of oil. (a) Thickness. (b) Volume.

Appearance Code has been adopted in this work to describe oil spills. Considering that the finer parts of the discharge evaporate quickly—those appearing silver, rainbow, and metallic, i.e., the part of the spill thinner than 50 microns—shall be grouped into one category called sheens. Four classes are distinguished: sheens (0.04–50 microns), discontinuous true-color oil (50–200 microns), continuous true-color (>200 microns), and emulsion (>500 microns).

Based on the research by Zhao et al. [45], it is possible to distinguish between three types of oil slicks: sheens, discontinuous true-color oil, and emulsions in AVIRIS 1. However, continuous true-color oil could not be identified, as it is mistaken for discontinuous true-color oil, as could already be guessed from the visual analysis. Denser parts of the spill have different spectral behavior. As shown in Fig. 14, most of the sheen pixels are qualified as such using NDOI. Nevertheless, NDOI misclassifies some discontinuous oil pixels as sheen pixels and assigns some emulsion pixels to the discontinuous oil class. Again, the algorithm obtains higher precision than recall for all categories. F1-score results for sheen, discontinuous true-color oil, and emulsion classes are satisfactory, with 0.977, 0.944, and 0.946, respectively, and an overall accuracy of 0.964 and an F1-score of 0.955.

Hu et al. [20] carried out the second work, where they calculated the oil volume of the spill with MERIS images. Although there are no images of the exact date, the difference is only two days with MERIS 2. As the work covered the complete spill, we estimate that the variations in the volume are not significant in this period, and the article results serve as a reference for us. The success rate of the classes using NDOI is very high (above 95%) except for a volume of about 100 L, which is easily confused with the regions of around 1000 L (65%). The F1-score for the classes from less than 1 L to more than 1000 L is 0.990, 0.987, 0.787, and 0.985, correspondingly, resulting in an overall F1-score of 0.937 and an overall accuracy of 0.985.

Considering that the preceding metrics give very satisfactory results, above 90% in all cases, we consider that NDOI can distinguish between different thicknesses of the spill and among oil volumes. Based on the replication of prior research results, the index’s performance has overcome the effect of sunglint and the optical complexity of analyzing the entire spot. Moreover, AI techniques excel in the differentiation of oil thicknesses at the cost of increased computational time [25]. Spectral indices are thus a safe bet for studies using satellites or airborne sensors.

V. CONCLUSION

NDOI has proven to be effective when applied to different sensor data. It accentuates contaminated parts of medium and high thickness, although it is more challenging to identify sheens and very dense spots where the oil is almost black. With NDOI, we have detected the complete oil spill, with all the difficulties that this entails, and different thicknesses have been identified in several scenes. Its performance on all images is comparable to other indices in the literature, such as FI, CDOM, and NDVI, and is remarkably consistent with RAI. Its main advantage over the other indices is that it does not misclassify the sand in suspension from the Mississippi River delta and the spill. This can be a significant improvement when studying coastal spills. The fewer oil slick look-alikes that can occur, the less likely false spill detection will happen. Another great advantage of NDOI is that the bands used are ubiquitous in optical sensors, and it does not need to cover the infrared range, thus making its applicability wider. Regarding the performance quality, the oil hit rate exceeds 95% in all images with coarse spillage, reaching an average accuracy of 0.945 and an average F1-score of 0.830. Consequently, NDOI achieves the highest overall rating among the spectral indices, with a figure of merit that combines accuracy and F1-score (0.816). In addition, even under the sunglint effect, it has been possible to reproduce the literature estimate of spill thickness and oil volume with metrics results exceeding 90%.

NDOI is more than adequate for detecting spills with thicknesses more significant than 50 microns. It utilizes universal bands in satellites, and due to its ease of use and quick calculation time, its incorporation in hardware acceleration devices is also appropriate, reducing the processing time, the resources needed, and the energy consumed. At a further stage of our research, the efficiency of NDOI on other spills will be assessed, along with the potential for misclassification with other oil slick look-alikes. We have also started to develop low-cost sensors with bands

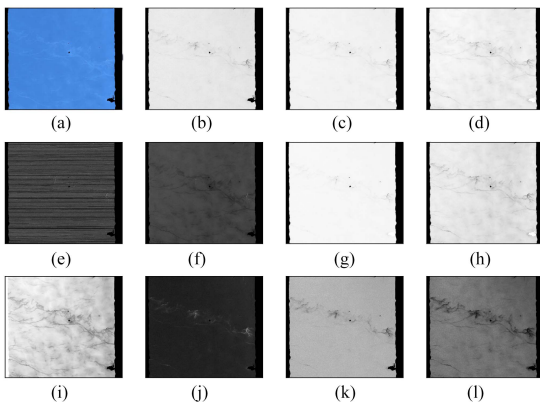


Fig. 15. AVIRIS true color RGB and spectral indices from 18 May 2010, at 19:59. (a) RGB AVIRIS 2. (b) NDOI. (c) RAI. (d) FI. (e) HI. (f) OSI. (g) WAF. (h) CDOM. (i) CHL. (j) NDVI. (k) NDWI. (l) RATIO B2/B11.

tailored to the specific requirements of particular scenarios. The combination of low-cost multispectral sensors and UAVs allows us to respond quickly to environmental crises and minimize their impact. Implementing multispectral sensors with the required wavelengths to obtain NDOI will allow real-time results, further facilitating decision-making in critical situations.

APPENDIX

EXTENSION OF THE QUALITATIVE ANALYSIS

The qualitative analysis of these images is complementary to the investigations conducted in Section IV-B. It enhances our understanding by providing nuanced insights and a visual perspective of AVIRIS 2, HICO 2, and MERIS 2.

AVIRIS 2 (see Fig. 15), taken the following day of AVIRIS 1, shows similar behavior to that already observed. In this scene, the spill is not very thick. The RGB image shows how some low-thickness filaments, perhaps mixed with water, cross the image horizontally. Around them, there is some sheen coming from thin layers of oil. The NDOI, RAI, FI, and CDOM indices highlight the few regions of thicker contamination in the image—which is more noticeable in CDOM. Analogously, the NDVI emphasizes the same pattern but reversed. Once again, the index that most reveals the fine contamination is the B2/B11 ratio, as the shape of the spill is visible, and some sheens are discernible. On this occasion, neither HI nor OSI can be accepted as valid indices. In this scene, the HI banding obstructs the analysis of the image. Part of the spill is visible in OSI, but the difference between oil and water is not evident. Similar issues arise with CHL, where the thin crude oil film can be better distinguished. However, the separation between the sea and the sheen is still hazy, blurring the result and making interpretation difficult. The WAF result is essentially nonexistent because there is no thick film in the scene except for a few minor soft spots. Finally, despite the lack of sheens, the NDWI can still make out the narrow bands of spills.

HICO 2, represented in Fig. 16, has similar characteristics to AVIRIS 2. It is a scene with clouds in which only thin patches are found. Consequently, the behavior of the spectral indices is likely

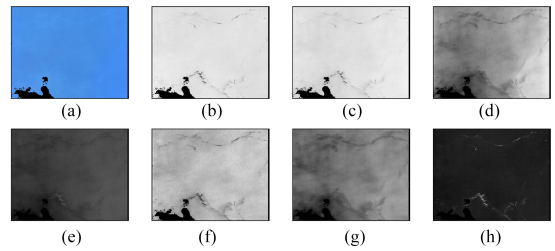


Fig. 16. HICO false color RGB and spectral indices from 28 May 2010, at 13:21. (a) RGB HICO 2. (b) NDOI. (c) RAI. (d) FI. (e) OSI. (f) CDOM. (g) CHL. (h) NDVI.

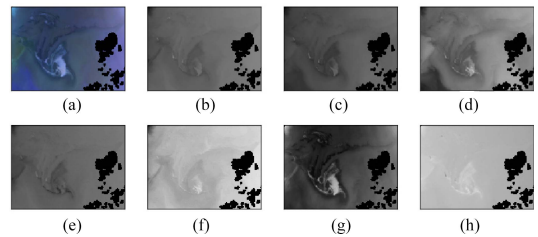


Fig. 17. MERIS false color RGB and spectral indices from 2 May 2010, at 03:51. (a) RGB MERIS 2. (b) NDOI. (c) RAI. (d) FI. (e) OSI. (f) CDOM. (g) CHL. (h) NDVI.

to be similar as well. NDOI and RAI are visually identical, indicating the regions of fuel accumulation. The NDVI reproduces this same behavior. CDOM, as on previous occasions, highlights the thicker areas of the spill and some thinner parts. FI and CHL enhance its fine details even more, reaching a situation where it is difficult to distinguish the main spill path. Likewise, we identify the area with the highest accumulation with OSI, but the distinction with the less polluted area is blurred.

MERIS 2 presents a similar situation to MERIS 1 (see Fig. 17). The spill is complex and shows significant variations in spectral behavior. At first glance, CHL indicates all the core characteristics and upper ridges. Next is FI, which outlines the silhouette of the spill and gives a glimpse of the crests. In RAI and NDOI, it is more difficult to distinguish the peaks from the background. OSI, CDOM, or NDVI cannot accurately detect ridges. However, the core is visible in all three indices, and it is easy to identify with OSI.

REFERENCES

- [1] G. Andreoli, B. Bulgarelli, B. Hosgood, and D. Tarchi, "Hyperspectral analysis of oil and oil-impacted soils for remote sensing purposes," *Eur. Commission Joint Res. Centre: Luxembourg*, vol. 36, pp. 2–30, 2007.
- [2] D. Angelova, I. Uzunov, S. Uzunova, A. Gigova, and L. Minchev, "Kinetics of oil and oil products adsorption by carbonized rice husks," *Chem. Eng. J.*, vol. 172, no. 1, pp. 306–311, 2011. [Online]. Available: <https://www.sciencedirect.com/science/article/pii/S1385894711006954>
- [3] M. Fingas and C. Brown, "Review of oil spill remote sensing," *Mar. Pollut. Bull.*, vol. 83, no. 1, pp. 9–23, 2014. [Online]. Available: <https://www.sciencedirect.com/science/article/pii/S0025326X14002021>
- [4] M. Fingas and C. Brown, "Chapter 5—oil spill remote sensing," in *Oil Spill Science and Technology*, 2nd ed., M. Fingas, Ed. Amsterdam, The Netherlands: Elsevier, 2017, pp. 305–385.

- [5] C. Brekke and A. H. Solberg, "Oil spill detection by satellite remote sensing," *Remote Sens. Environ.*, vol. 95, no. 1, pp. 1–13, 2005. [Online]. Available: <https://www.sciencedirect.com/science/article/pii/S0034425704003724>
- [6] P. Odonkor, Z. Ball, and S. Chowdhury, "Distributed operation of collaborating unmanned aerial vehicles for time-sensitive oil spill mapping," *Swarm Evol. Comput.*, vol. 46, pp. 52–68, 2019. [Online]. Available: <https://www.sciencedirect.com/science/article/pii/S2210650217309288>
- [7] N. Aghaei, G. Akbarizadeh, and A. Kosarian, "Osdes_net: Oil spill detection based on efficient_shuffle network using synthetic aperture radar imagery," *Geocarto Int.*, vol. 37, no. 26, pp. 13539–13560, 2022.
- [8] J. L. E. Honrado, D. B. Solpico, C. M. Favila, E. Tongson, G. L. Tangonan, and N. J. C. Libatique, "UAV imaging with low-cost multispectral imaging system for precision agriculture applications," in *Proc. IEEE Glob. Humanitarian Technol. Conf.*, 2017, pp. 1–7.
- [9] A. Morales et al., "A multispectral camera development: From the prototype assembly until its use in a UAV system," *Sensors*, vol. 20, no. 21, 2020, Art. no. 6129. [Online]. Available: <https://www.mdpi.com/1424-8220/20/21/6129>
- [10] A. Pérez-García, A. Rodríguez-Molina, E. Hernández, L. Vera, and J. F. López, "Development of low-cost multi-spectral cameras for precision agriculture," in *Proc. IEEE Int. Geosci. Remote Sens. Symp.*, 2023, pp. 3466–3469.
- [11] V. Satriano, E. Ciancia, T. Lacava, N. Pergola, and V. Tramutoli, "Improving the RST-oil algorithm for oil spill detection under severe sun glint conditions," *Remote Sens.*, vol. 11, no. 23, 2019, Art. no. 2762. [Online]. Available: <https://www.mdpi.com/2072-4292/11/23/2762>
- [12] C. R. Jackson and W. Alpers, "The role of the critical angle in brightness reversals on sunglint images of the sea surface," *J. Geophysical Research: Oceans*, vol. 115, no. C9, 2010, Art. no. C09019.
- [13] M. Fingas and C. E. Brown, "A review of oil spill remote sensing," *Sensors*, vol. 18, no. 91, pp. 1–18, 2018. [Online]. Available: <https://www.mdpi.com/1424-8220/18/1/91>
- [14] J. Zhao, M. Temimi, H. Ghedira, and C. Hu, "Exploring the potential of optical remote sensing for oil spill detection in shallow coastal waters—a case study in the arabian gulf," *Opt. Exp.*, vol. 22, no. 11, pp. 13755–13772, Jun. 2014. [Online]. Available: <http://www.opticsexpress.org/abstract.cfm?URI=oe-22-11-13755>
- [15] A. J. Brown, "Spectral curve fitting for automatic hyperspectral data analysis," *IEEE Trans. Geosci. Remote Sens.*, vol. 44, no. 6, pp. 1601–1608, Jun. 2006.
- [16] J. Yang, J. Wan, Y. Ma, J. Zhang, and Y. Hu, "Characterization analysis and identification of common marine oil spill types using hyperspectral remote sensing," *Int. J. Remote Sens.*, vol. 41, no. 18, pp. 7163–7185, 2020, doi: [10.1080/01431161.2020.1754496](https://doi.org/10.1080/01431161.2020.1754496).
- [17] M. Fingas, "Visual appearance of oil on the sea," *J. Mar. Sci. Eng.*, vol. 9, no. 97, pp. 1–13, 2021.
- [18] R. N. Clark et al., "A method for quantitative mapping of thick oil spills using imaging spectroscopy," *US Geological Surv. Open-File Rep.*, vol. 1167, no. 2010, pp. 1–51, 2010.
- [19] J. Svejkovsky, M. Hess, J. Muskat, T. J. Nedwed, J. McCall, and O. Garcia, "Characterization of surface oil thickness distribution patterns observed during the deepwater horizon (MC-252) oil spill with aerial and satellite remote sensing," *Mar. Pollut. Bull.*, vol. 110, no. 1, pp. 162–176, 2016.
- [20] C. Hu et al., "Remote sensing estimation of surface oil volume during the 2010 deepwater horizon oil blowout in the gulf of Mexico: Scaling up AVIRIS observations with MODIS measurements," *J. Appl. Remote Sens.*, vol. 12, no. 2, pp. 1–44, 2018, doi: [10.1117/JRS.12.026008](https://doi.org/10.1117/JRS.12.026008).
- [21] L. Xu, J. Li, and A. Brenning, "A comparative study of different classification techniques for marine oil spill identification using radarsat-1 imagery," *Remote Sens. Environ.*, vol. 141, pp. 14–23, 2014. [Online]. Available: <https://www.sciencedirect.com/science/article/pii/S0034425713003805>
- [22] A. Raëisi, G. Akbarizadeh, and A. Mahmoudi, "Combined method of an efficient cuckoo search algorithm and nonnegative matrix factorization of different zernike moment features for discrimination between oil spills and lookalikes in SAR images," *IEEE J. Sel. Topics Appl. Earth Observ. Remote Sens.*, vol. 11, no. 11, pp. 4193–4205, Nov. 2018.
- [23] F. M. Ghara, S. B. Shokouhi, and G. Akbarizadeh, "A new technique for segmentation of the oil spills from synthetic-aperture radar images using convolutional neural network," *IEEE J. Sel. Topics Appl. Earth Observ. Remote Sens.*, vol. 15, pp. 8834–8844, 2022.
- [24] R. Al-Ruzouq et al., "Sensors, features, and machine learning for oil spill detection and monitoring: A review," *Remote Sens.*, vol. 12, no. 20, 2020, Art. no. 3338. [Online]. Available: <https://www.mdpi.com/2072-4292/12/20/3338>
- [25] B. Wang et al., "A spectral-spatial features integrated network for hyperspectral detection of marine oil spill," *Remote Sens.*, vol. 13, no. 8, 2021, Art. no. 1568. [Online]. Available: <https://www.mdpi.com/2072-4292/13/8/1568>
- [26] Z. Xiao, S. Liang, J. Wang, B. Jiang, and X. Li, "Real-time retrieval of leaf area index from modis time series data," *Remote Sens. Environ.*, vol. 115, no. 1, pp. 97–106, 2011. [Online]. Available: <https://www.sciencedirect.com/science/article/pii/S003442571000249X>
- [27] Y. Liu, A. MacFadyen, Z.-G. Ji, and R. H. Weisberg, "Introduction to monitoring and modeling the deepwater horizon oil spill," *Geophys. Monogr. Ser.*, vol. 195, pp. 1–7, 2011.
- [28] O. Garcia-Pineda et al., "Detection of oil near shorelines during the deepwater horizon oil spill using synthetic aperture radar (SAR)," *Remote Sens.*, vol. 9, no. 6, 2017, Art. no. 567. [Online]. Available: <https://www.mdpi.com/2072-4292/9/6/567>
- [29] A. Pérez-García, P. Horstrand, and J. F. López, "Ndoi, a novel oil spectral index: Comparisons and results," in *Proc. 12th Workshop Hyperspectral Imag. Signal Process.: Evol. Remote Sens.*, 2022, pp. 1–5.
- [30] N. Audebert, B. L. Saux, and S. Lefèvre, "Deep learning for classification of hyperspectral data: A comparative review," *IEEE Geosci. Remote Sens. Mag.*, vol. 7, no. 2, pp. 159–173, Jun. 2019.
- [31] S. Hafeez et al., "Detection and monitoring of marine pollution using remote sensing technologies," in *Monitoring of Marine Pollution* (ser. Chapters), H. B. Fouzia, Ed. London, U.K.: IntechOpen, Sep. 2019. [Online]. Available: <https://ideas.repec.org/h/ito/pchaps/163515.html>
- [32] I. Leifer et al., "State of the art satellite and airborne marine oil spill remote sensing: Application to the bp deepwater horizon oil spill," *Remote Sens. Environ.*, vol. 124, pp. 185–209, 2012. [Online]. Available: <https://www.sciencedirect.com/science/article/pii/S0034425712001563>
- [33] B. Zhang, L. Zhao, and X. Zhang, "Three-dimensional convolutional neural network model for tree species classification using airborne hyperspectral images," *Remote Sens. Environ.*, vol. 247, 2020, Art. no. 111938. [Online]. Available: <https://www.sciencedirect.com/science/article/pii/S0034425720303084>
- [34] T. Bijeesh and K. Narasimhamurthy, "A comparative study of spectral indices for surface water delineation using landsat 8 images," in *Proc. Int. Conf. Data Sci. Commun.*, IEEE, 2019, pp. 1–5.
- [35] A. Pérez-García, P. Horstrand, and J. F. López, "A novel spectral index for ocean oil spill detection," in *Proc. ESA Living Planet Symp.*, 2022, p. 1.
- [36] E. Loos, L. Brown, G. Borstad, T. Mudge, and M. Álvarez, "Characterization of oil slicks at sea using remote sensing techniques," in *Proc. Oceans, IEEE*, 2012, pp. 1–4.
- [37] F. K. C. author, K. Oppermann, and B. Hörig, "Hydrocarbon index—An algorithm for hyperspectral detection of hydrocarbons," *Int. J. Remote Sens.*, vol. 25, no. 12, pp. 2467–2473, 2004, doi: [10.1080/01431160310001642287](https://doi.org/10.1080/01431160310001642287).
- [38] Q. Li, L. Lu, B. Zhang, and Q. Tong, "Oil slope index: An algorithm for crude oil spill detection with imaging spectroscopy," in *Proc. 2nd Int. Workshop Earth Observ. Remote Sens. Appl.*, 2012, pp. 46–49.
- [39] W.-Z. Lu et al., "Modern near infrared spectroscopy analytical technology," 2nd ed. Beijing: China Petrochemical Press, 2007.
- [40] T. Kutser, D. C. Pierson, K. Y. Kallio, A. Reinart, and S. Sobek, "Mapping lake CDOM by satellite remote sensing," *Remote Sens. Environ.*, vol. 94, no. 4, pp. 535–540, 2005. [Online]. Available: <https://www.sciencedirect.com/science/article/pii/S0034425704003670>
- [41] C. Hu, Z. Lee, and B. Franz, "Chlorophyll algorithms for oligotrophic oceans: A novel approach based on three-band reflectance difference," *J. Geophysical Res.: Oceans*, vol. 117, no. C1, 2012, Art. no. C01011.
- [42] D. A. Carlson and T. N. Ripley, "On the relation between NDVI, fractional vegetation cover, and leaf area index," *Remote Sens. Environ.*, vol. 62, no. 3, pp. 241–252, 1997.
- [43] B. cai Gao, "NDWI—A normalized difference water index for remote sensing of vegetation liquid water from space," *Remote Sens. Environ.*, vol. 58, no. 3, pp. 257–266, 1996. [Online]. Available: <https://www.sciencedirect.com/science/article/pii/S0034425796000673>
- [44] P. Kolokoussis and V. Karathanassi, "Oil spill detection and mapping using sentinel 2 imagery," *J. Mar. Sci. Eng.*, vol. 6, no. 4, pp. 1–12, 2018. [Online]. Available: <https://www.mdpi.com/2077-1312/6/1/4>
- [45] D. Zhao, X. Cheng, H. Zhang, Y. Niu, Y. Qi, and H. Zhang, "Evaluation of the ability of spectral indices of hydrocarbons and seawater for identifying oil slicks utilizing hyperspectral images," *Remote Sens.*, vol. 10, no. 3, 2018, Art. no. 421. [Online]. Available: <https://www.mdpi.com/2072-4292/10/3/421>

- [46] V. Klemas, "Tracking oil slicks and predicting their trajectories using remote sensors and models: Case studies of the sea princess and deepwater horizon oil spills," *J. Coastal Res.*, vol. 2010, no. 265, pp. 789–797, 2010, doi: [10.2112/10A-00012.1](https://doi.org/10.2112/10A-00012.1).
- [47] L. Cong, B. Nutter, and D. Liang, "Estimation of oil thickness and aging from hyperspectral signature," in *2012 IEEE Southwest Symp. Image Anal. Interpretation*, 2012, pp. 213–216.
- [48] V. Karathanassi, "Spectral unmixing evaluation for oil spill characterization," *Int. J. Remote Sens. Appl.*, vol. 4, pp. 1–17, 2014.
- [49] F. Carnesecci, V. Byfield, P. Cipollini, G. Corsini, and M. Diani, "An optical model for the interpretation of remotely sensed multispectral images of oil spill," *Proc. SPIE*, vol. 7105, pp. 11–22, 2008, doi: [10.1117/12.800304](https://doi.org/10.1117/12.800304).
- [50] A. K. Mishra and G. S. Kumar, "Weathering of oil spill: Modeling and analysis," *Aquatic Procedia*, vol. 4, pp. 435–442, 2015, International Conference on Water Resources, Coastal and Ocean Engineering. [Online]. Available: <https://doi.org/10.1016/j.aapro.2015.02.058>
- [51] B. Agreement, "Bonn agreement website," 2024. [Online]. Available: <https://www.bonnagreement.org/>
- [52] R. O. Green et al., "Imaging spectroscopy and the airborne visible/infrared imaging spectrometer (aviris)," *Remote Sens. Environ.*, vol. 65, no. 3, pp. 227–248, 1998.
- [53] N. Jet Propulsion Laboratory, "Airborne visible infrared imaging spectrometer website," 2021. [Online]. Available: <https://aviris.jpl.nasa.gov/>
- [54] NASA, "Earth data, ocean color web, HICO," 2021. [Online]. Available: <https://oceancolor.gsfc.nasa.gov/data/hico/>
- [55] E. S. A. Signature, "Earth online, envisat, meris," 2021. [Online]. Available: <https://earth.esa.int/cogateway/instruments/meris>
- [56] Y. Mo, M. S. Kearney, and J. C. A. Riter, "Post-deepwater horizon oil spill monitoring of louisiana salt marshes using landsat imagery," *Remote Sens.*, vol. 9, no. 6, 2017, Art. no. 547. [Online]. Available: <https://www.mdpi.com/2072-4292/9/6/547>
- [57] L. Gómez-Chova, G. Camps-Valls, J. Calpe-Maravilla, L. Guanter, and J. Moreno, "Cloud-screening algorithm for ENVISAT/MERIS multi-spectral images," *IEEE Trans. Geosci. Remote Sens.*, vol. 45, no. 12, pp. 4105–4118, Dec. 2007.
- [58] E. Fix and J. L. Hodges, "Discriminatory analysis: Nonparametric discrimination: Consistency properties," *Int. Stat. Rev./Revue Int. de Statistique*, vol. 57, no. 3, pp. 238–247, 1989.
- [59] N. S. Altman, "An introduction to kernel and nearest-neighbor nonparametric regression," *Amer. Statist.*, vol. 46, no. 3, pp. 175–185, 1992. [Online]. Available: <https://www.tandfonline.com/doi/abs/10.1080/00031305.1992.10475879>
- [60] I. Mani and I. Zhang, "kNN approach to unbalanced data distributions: A case study involving information extraction," in *Proc. Workshop Learn. Imbalanced Datasets*, 2003, vol. 126, pp. 1–7.
- [61] M. Hossin and M. N. Sulaiman, "A review on evaluation metrics for data classification evaluations," *Int. J. Data Mining Knowl. Manage. Process.*, vol. 5, no. 2, pp. 1–11, 2015.
- [62] S. Boughorbel, F. Jarray, and M. El-Anbari, "Optimal classifier for imbalanced data using Matthews correlation coefficient metric," *PLoS One*, vol. 12, no. 6, 2017, Art. no. e0177678.



Ámbar Pérez-García (Graduate Student Member, IEEE) was born in Las Palmas de Gran Canaria, Spain, in 1997. She received the B.Sc. degree in physics from the University of La Laguna (ULL), La Laguna, Spain, and the M.Sc. degree in remote sensing from the University of Valencia (UV), Valencia, Spain, in 2019 and 2020, respectively, the M.Sc. degree in education from the University of La Rioja (UNIR), La Rioja, Spain, in 2021. She is currently working toward the Ph.D. degree in telecommunications technologies with the University of Las Palmas

de Gran Canaria (ULPGC), Las Palmas de Gran Canaria, Spain. She is with the Institute for Applied Microelectronics, IUMA, University of Las Palmas de Gran Canaria, Las Palmas de Gran Canaria, Spain. In 2023, she did a research stay on neural network segmentation with HYPERCOMP, University of Extremadura, Spain. She was also with HWM, Wageningen University & Research, The Netherlands, spectrally characterizing plastics. Her research interests include remote sensing, hyperspectral image processing, artificial intelligence, and the detection of marine litter.



Gran Canaria (ULPGC), developing a multipurpose multispectral camera with built-in artificial intelligence.

Adrián Rodríguez-Molina was born in Las Palmas de Gran Canaria, Spain, in 1998. He received the engineering degree in industrial electronics and automatic from the University of Las Palmas de Gran Canaria, Las Palmas de Gran Canaria, Spain, in 2020, and the master's degree in applied electronics and telecommunications from the Institute for Applied Microelectronics, Las Palmas de Gran Canaria, Spain, in 2021. He is currently working toward the Ph.D. degree in telecommunication technologies and computational engineering with the University of Las Palmas de Gran Canaria (ULPGC), developing a multipurpose multispectral camera with built-in artificial intelligence.

Emma Hernández was born in Las Palmas de Gran Canaria in 1997. She received the bachelor's degree in industrial and automatic electronic engineering from the University of Las Palmas de Gran Canaria (ULPGC), Las Palmas de Gran Canaria, Spain, and the master's degree in control and robotics from the Polytechnic University of Madrid (UPM), Madrid, Spain, in 2020 and 2021, respectively. She is currently working toward the Ph.D. degree in telecommunications technologies with the ULPGC.



She is a Researcher with the Institute of Applied Microelectronics, IUMA, University of Las Palmas de Gran Canaria, Las Palmas de Gran Canaria, Spain. In 2023, she conducted a research stay in thermographic image processing at the University of Oviedo, Spain. Her research interests include image processing, unmanned aerial vehicles (UAVs), hyperspectral technology, and thermography technologies and their applications.



José Fco López received the M.S. degree in physics (specializing in electronics) from the University of Seville, Sevilla, Spain, in 1989 and the Ph.D. degree in high-speed integrated systems from the University of Las Palmas de Gran Canaria (ULPGC), Las Palmas de Gran Canaria, Spain, in 1994.

He was with Thomson Composants Microondes, Orsay, France, in 1992. In 1995, he was with the Center for Broadband Telecommunications, Technical University of Denmark (DTU), Lyngby, Denmark. In 1996, 1997, 1999, and 2000, he was a Visiting Researcher with the Edith Cowan University (ECU), Perth, Western Australia. He has conducted investigations with the Institute for Applied Microelectronics (IUMA), where he has acted as Deputy Director since 2009. He is currently a Lecturer with the School of Telecommunication and Electronics Engineering and with an M.Sc. Program of IUMA, ULPGC. He has authored/coauthored around 150 papers in national and international journals and conferences. His current research interests include image processing, UAVs, hyperspectral technology, and their applications.

Dr López has been actively enrolled in more than 50 research projects funded by the European Community, Spanish Government, and international private industries in Europe, the USA, and Australia.

Chapter 3

Band Selection Method for Efficient Water Pollution Monitoring

Hyperspectral sensors provide valuable data across a wide range of the electromagnetic spectrum. However, their high spectral dimensionality, often containing redundant information, presents processing time, resource consumption, and cost challenges. Therefore, machine learning techniques for band reduction play a critical role in efficient water pollutant monitoring. By selecting only the most relevant spectral bands, the complexity and dimensionality of hyperspectral imagery can be reduced while maintaining high detection accuracy.

This chapter supports Sub-objective 2 of the thesis, developing a dimensionality reduction methodology that optimizes the spectral bands for water pollutant monitoring and improves the transferability of results across different environments. Finding bands of interest that allow the identification of contaminants in different scenarios opens the opportunity of transferring results from one scenario to another and generalizing classification models that can be applied across various environments. This approach will enable the classification of different HSI without needing labelled data. Additionally, this sets the stage for developing cost-effective multispectral sensors specialized to study specific pollutants or phenomena, reducing the volume of information and the computational time required to process the images.

A preliminary version of the band selection methodology was presented in the conference paper **C.2** “Spectral Band Selection Methodology for Future Sensor Development”. This conference paper laid the foundation for the approach used in this chapter by introducing a strategy to target specific spectral bands relevant to pollutant classification, aiming to enhance monitoring systems’ efficiency. This work is also related to the conference paper **C.3** “Development of Low-Cost Multi-Spectral Cameras for Precision Agriculture,” which presented an initial prototype of a multispectral sensor with interchangeable optical filters. This prototype allows the selection of spectral bands tailored to specific applications, enabling the sensor to adapt to different monitoring needs.

Section **3.1**: “Efficient Plastic Detection in Coastal Areas with Selected Spectral Bands,” focuses on detecting plastic pollutants in coastal areas. This study builds on the previously presented method and extends the methodology by incorporating the transfer of results between datasets captured under different conditions. The research highlights the significant influence that background elements have on the spectral signature when classifying semi-transparent surfaces. Additionally, it concludes that while the transfer of selected spectral bands between datasets proves effective, the transfer of pre-trained classification models remains limited, indicating that further refinement is needed for robust generalization across varying environmental conditions.

Moreover, Section **3.2**: “Developing a Generalizable Spectral Classifier for Rhodamine Detection in Aquatic Environments” expands the scope to include the detection and estimation of the concentration of Rhodamine, a dye often used as a tracer in hydrodynamics studies in estuaries, rivers and coastal areas. This study further explores the influence of backgrounds on spectral signatures in optically shallow areas, where both the background and the water surface reflect sunlight. The research introduces two techniques to improve the transfer of pre-trained models. First, by training the classification model with a combination of different scenarios that may be encountered, the model’s adaptability is enhanced, and the risk of overfitting is reduced. Second, the study proposes using the first derivative of the spectral signature instead of the signature itself, as the derivative better emphasizes spectral differences between classes. These advancements bring us closer to developing generalizable models capable of classifying new images without requiring labelled data.

This chapter contributes to optimizing water pollutant monitoring by identifying the most influential spectral bands to reduce HSI complexity and improve detection accuracy. It also advances the transferability of results across different environments, moving closer to developing generalizable models and reducing the need for labelled data.

3.1 Efficient Plastic Detection in Coastal Areas with Selected Spectral Bands

- **Á. Pérez-García**, T.H.M. van Emmerik, A. Mata, P.F. Tasserón and J. F. López, “Efficient plastic detection in coastal areas with selected spectral bands,” *Marine Pollution Bulletin*, vol. 207, p. 116914, 2024.
- DOI: [10.1016/j.marpolbul.2024.116914](https://doi.org/10.1016/j.marpolbul.2024.116914)
- Publisher: Elsevier.
- Print ISSN: 1545-598X (Electronic ISSN: 1558-0571).
- Journal metrics:
 - 2023 Journal Impact Factor: 5.3
 - Journal Citation Indicator (JCI): 1.49
 - Rank by Journal Impact Factor:
 - * Q1: Environmental Sciences; Marine & Freshwater Biology.



Contents lists available at ScienceDirect

Marine Pollution Bulletin

journal homepage: www.elsevier.com/locate/marpolbul

Efficient plastic detection in coastal areas with selected spectral bands

Ámbar Pérez-García^{a,b,*}, Tim H.M. van Emmerik^b, Aser Mata^c, Paolo F. Tasseron^{b,d}, José F. López^a

^a Institute for Applied Microelectronics, University of Las Palmas de Gran Canaria, Las Palmas de Gran Canaria, 35001, Spain

^b Hydrology and Environmental Hydraulics Group, Wageningen University, Wageningen, 6708, BP, the Netherlands

^c Digital Innovation and Marine Autonomy, Plymouth, Marine Laboratory (PML), Plymouth, PL1 3DH, United Kingdom

^d Amsterdam Institute for Advanced Metropolitan Solutions, Amsterdam, 1018, JA, the Netherlands

ARTICLE INFO

Keywords:

Remote sensing
Macroplastic detection
Artificial intelligence
Band selection

ABSTRACT

Marine plastic pollution poses significant ecological, economic, and social challenges, necessitating innovative detection, management, and mitigation solutions. Spectral imaging and optical remote sensing have proven valuable tools in detecting and characterizing macroplastics in aquatic environments. Despite numerous studies focusing on bands of interest in the shortwave infrared spectrum, the high cost of sensors in this range makes it difficult to mass-produce them for long-term and large-scale applications. Therefore, we present the assessment and transfer of various machine learning models across four datasets to identify the key bands for detecting and classifying the most prevalent plastics in the marine environment within the visible and near-infrared (VNIR) range. Our study uses four different databases ranging from virgin plastics under laboratory conditions to weather plastics under field conditions. We used Sequential Feature Selection (SFS) and Random Forest (RF) models for the optimal band selection. The significance of homogeneous backgrounds for accurate detection is highlighted by a 97 % accuracy, and successful band transfers between datasets (87 %–91 %) suggest the feasibility of a sensor applicable across various scenarios. However, the model transfer requires further training for each specific dataset to achieve optimal accuracy. The results underscore the potential for broader application with continued refinement and expanded training datasets. Our findings provide valuable information for developing compelling and affordable detection sensors to address plastic pollution in coastal areas. This work paves the way towards enhancing the accuracy of marine litter detection and reduction globally, contributing to a sustainable future for our oceans.

1. Introduction

Marine litter, particularly plastic pollution, has become a pervasive problem affecting terrestrial and aquatic ecosystems globally, leading to significant ecological, economic, and health impacts. Single-use plastics and inadequate waste management practices have led to vast contamination of rivers and oceans Morales-Caselles et al. (2021), posing significant challenges to the environment Meijer et al. (2021). Plastic debris accumulation in marine environments threatens wildlife and habitats and challenges maritime industries and coastal communities Jambeck et al. (2015). Identifying polymer types is relevant because each plastic type has distinct impacts, sources, and transport behaviours, making its identification crucial for a comprehensive understanding Andradý (2011); Rochman et al. (2013). Monitoring plastic pollution is crucial for establishing a baseline understanding to track changes,

and assess the efficacy of implemented measures van Emmerik et al. (2023); Tasseron et al. (2024).

In situ monitoring of floating marine plastic debris, such as net surveys and visual observation, can be expensive, time-consuming, and requires expert supervision Armitage et al. (2022). Recent advances in remote sensing (RS) using multi- and hyperspectral imagery are promising for detecting macroplastics (≥ 0.5 cm) pollution from space Lebret et al. (2018); Topouzelis et al. (2021); Schreyers et al. (2022). RS provides significant advantages over traditional methods by enabling efficient and continuous data acquisition and overcoming geographical and resource limitations Biermann et al. (2020). Additionally, uncrewed aerial vehicles (UAVs) have the potential for long-term plastic monitoring, offering advantages such as improved spatial resolution, quick response time, and lower operational costs Andriolo et al. (2023).

Numerous object detection and classification machine learning tools

* Corresponding author at: Institute for Applied Microelectronics, University of Las Palmas de Gran Canaria, Las Palmas de Gran Canaria, 35001, Spain.

E-mail address: ambar.perez@ulpgc.es (Á. Pérez-García).

<https://doi.org/10.1016/j.marpolbul.2024.116914>

Received 12 July 2024; Received in revised form 29 August 2024; Accepted 29 August 2024

Available online 7 September 2024

0025-326X/© 2024 The Authors. Published by Elsevier Ltd. This is an open access article under the CC BY license (<http://creativecommons.org/licenses/by/4.0/>).

have been developed to monitor plastics in aquatic environments van Lieshout et al. (2020); Cortesi (2021); Rußwurm et al. (2023). Efforts have also been made to enhance detection from space using fusion Kremezi et al. (2022) and unmixing techniques Papageorgiou et al. (2022), and a benchmark dataset with Sentinel-2 images has been created to compare the performance of various artificial intelligence algorithms Kikaki et al. (2022). Nevertheless, there is a need for affordable and standardized plastic detection methods and equipment to address the challenges of monitoring plastic pollution on a global scale Martínez-Vicente et al. (2019); Cózar et al. (2024).

Current hyperspectral sensors are expensive and require considerable computational resources. Most macroplastic studies focus on the near-infrared (NIR) to shortwave infrared (SWIR) range, particularly around 1150 nm, where distinct absorption peaks facilitate plastics identification Garaba and Dierssen (2020). However, as detectors in the SWIR over 1000 nm are more expensive than in the visible and near-infrared (VNIR), between 400 and 1000 nm, implementing a multispectral sensor in the VNIR for plastic detection worldwide would lead to a significant reduction in costs Pérez-García et al. (2023). Several studies suggest that a high level of spectral detail is unnecessary for detecting and classifying other pollutants with gradually changing spectral signatures Legleiter et al. (2019, 2022); Pérez-García et al. (2024b). This indicates that sensors with broader bands could still provide reliable plastic classification. Therefore, we envision an affordable multispectral sensor with selected spectral bands for plastic detection.

We present an assessment of various machine learning models across different datasets to identify the key spectral bands for classifying the most prevalent marine plastics. By evaluating the transferability of these key bands across the datasets, we show that a sensor using these bands could identify plastics in various scenarios and conditions. Therefore, our study explores the feasibility of developing a VNIR multispectral sensor for detecting and identifying coastal macroplastics. This technology aims to enhance plastic recovery efforts in both field and spaceborne remote sensing, supporting the transition towards improved ocean health.

2. Materials and methods

In this paper, we applied a refined band selection methodology to different plastic datasets to select the optimal number of bands and to identify the bands of interest for the detection and classification of plastics. We used spectral information from three datasets covering various scenarios, from laboratory experiments without a background signal to sand and pebble beaches. Based on classification and feature selection methods, we identified bands of interest for plastic detection and evaluated the transferability across the datasets. Finally, we test its applicability by transferring the bands of interest to a fourth new dataset collected for the study.

2.1. Datasets

We focused on plastic polymers that are most common in coastal and marine environments Schwarz et al. (2019); Morales-Caselles et al. (2021); Barry et al. (2023), and which are present across all the datasets used in this study. These include high-density polyethylene (HDPE) for bottles, low-density polyethylene (LDPE) for bags, polypropylene (PP) for containers, and polystyrene (PS), which is represented in both its foamed (expanded polystyrene, EPS) and non-foamed forms. The four datasets contain items from the four plastic classes (HDPE, LDPE, PP, and PS) under different conditions.

We used hyperspectral imagery of virgin rectangular sheets from the HyperDrone (HD) project, where the sheets were placed on two different Scottish beaches: the sandy, seaweed-covered Tynninghame Beach (56.01° N, -2.59° W) in 2020 and the pebble-stone shore near Oban Airport (56.46° N, -5.40° W) in 2021. The measures were made with

The Headwall Co-aligned VNIR and SWIR imager (NERC Field Spectroscopy Facility) Headwall Photonics (2020), which collects about 600 bands ranging from 450 to 2500 nm. The third dataset (WUR) is mainly composed of virgin plastic everyday items from domestic sources Tasseron et al. (2021a). The images were taken in the laboratory using Specim Fx10 and Fx17 cameras (Konica Minolta Company, Oulu, Finland) Specim Spectral Imaging (2019). Together, they range from 400 to 1700 nm, with about 300 bands. Fig. 1 presents an overview of the three datasets used to train the model. These datasets are available for further details; see Plymouth Marine Laboratory; Mata, A. (2023a) (HD20), Plymouth Marine Laboratory; Mata, A. (2023b) (HD21) and Tasseron et al. (2021b) (WUR).

We collected a new dataset comprising everyday plastics, with plastic bags, jars, bottles, and cups similar to those in the WUR dataset. This dataset serves as the testing ground for evaluating the model's applicability. The image was captured on a plain background with the Specim Fx10 and Fx17 cameras, following the WUR dataset procedure Tasseron et al. (2021a). Further information and the mean spectral signatures of this dataset are provided in Section 3.3.

2.2. Band selection methodology

The methodology determines the bands of interest based on a combination of classification and feature selection algorithms (Fig. 2) Pérez-García et al. (2024a).

Half of the data is used to train the classification models, of which 60 % belong to the training dataset, 30 % are for the test dataset, and 10 % for validation. We used Random Forest (RF) Ho (1995) and Support Vector Machine (SVM) Hearst et al. (1998) as classifiers, both with hyperparameter optimization. The feature selection algorithms are trained with the remaining half of the data and provided with the impurity-based feature importance of the classifiers to determine the best bands for classification. The feature selection algorithms used are

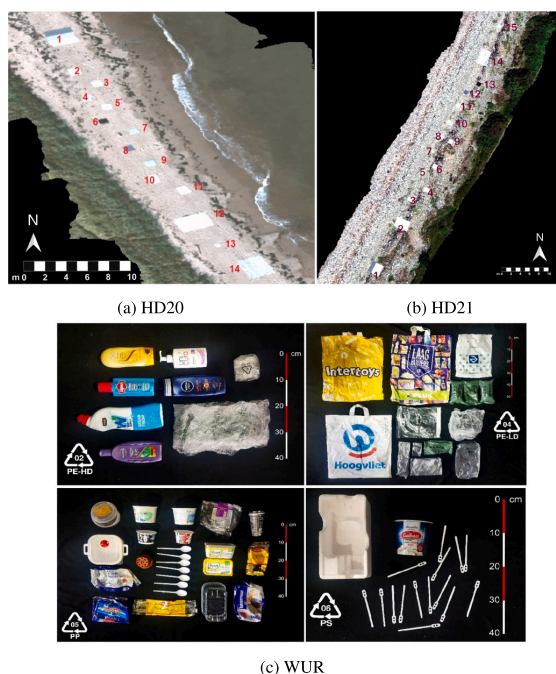


Fig. 1. Datasets overview Plymouth Marine Laboratory; Mata, A. (2023a,b); Tasseron et al. (2021b).

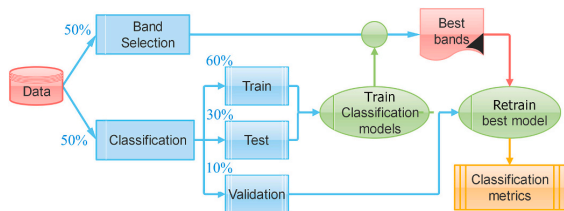


Fig. 2. Band selection methodology diagram Pérez-García et al. (2024a).

Sequential Feature Selector with forward selection (SFS) and Select From Model (SFM), both from the Python Scikit-Learn library Kramer (2016). SFS progressively includes or excludes features to optimize a classifier’s performance, providing the optimized subset of features. SFM evaluates features based on their feature importance for the classifier Kramer (2016).

The optimal number of bands is determined using the elbow method Syakur et al. (2018), identifying the point on the accuracy curve where improvement slows, forming an “elbow.” For the optimal number of bands, all classification metrics were calculated. Using only the best bands, the optimized classification models are re-trained. The validation dataset determines the classification metrics to assess performance. The overall accuracy (OAC) measures the ratio of correct predictions over the total number of samples Hossin and Sulaiman (2015). The F1 score is particularly useful with uneven class distribution, giving more importance to the accuracy of the smaller classes Boughorbel et al. (2017). The Kappa statistic (κ) measures inter-rater agreement for categorical items, correcting the bias that might occur due to chance agreement, especially with imbalanced datasets Cohen (1960).

Finally, we can evaluate the transferability of our results to different scenarios. This includes transferring bands of interest or pre-trained classification models. Transferring bands of interest involves using the identified wavelengths from one scenario to train a classifier in another scenario. The model transfer is challenging, as these models are tailored to specific scenario characteristics. If the spectral behaviour is sufficiently similar across scenarios, models can be effectively transferred, reducing the need for re-training the classifier and the computational time Pérez-García et al. (2024b).

Three measures of homogenization are applied to conduct a comparative study between the three datasets. First, the VNIR spectral range is selected, and the spectral ranges for which there is no data in all datasets are discarded. Therefore, the wavelengths of the study range from 490 to 850 nm. Second, the study only includes those elements of the datasets that match the target plastic types. From HD datasets: virgin EPS (PS class), agricultural PP, white HDPE net, and transparent LDPE, and from WUR: shampoo bottle and soap flask (HDPE), packaging bag (LDPE), bottle cap and food container (PP), and one-use white coffee stirrers (PS). The analysis includes backgrounds such as seaweed, rocks,

and wet and dry sand. Third, to prevent misclassification caused by unbalanced classes, pixels from each dataset are randomly selected until each class contains 2700 samples, matching the number of pixels in the smallest class (PS in HD21).

3. Experiments

We designed three experiments in this study. Experiment 1 includes an individual dataset analysis, which offers insights into its complexity. Furthermore, optimizing the hyperparameters of the band selection model allows for determining the optimal number of bands needed for the multispectral sensor. Experiment 2 focuses on transferring the results and involves applying the findings obtained by training the model with one dataset to another. It is possible to transfer both the bands of interest and the pre-trained models, providing an understanding of the model adaptability. In experiment 3, the results from experiments 1 and 2 are applied to a real case study with a new dataset to quantify its performance.

3.1. Experiment 1: individual dataset analysis

Selecting the optimal number of bands poses one of the most challenging aspects of dataset analysis. Fig. 3 presents the OAC as a function of the number of bands used to train the model. The dataset achieving the highest level of accuracy is HD20 (97 %), whereas HD21 exhibits the lowest accuracy (93 %). The analysis indicates that SFS presents better accuracy than SFM, and its combination with RF further enhances performance. According to the elbow method Syakur et al. (2018), three bands are ideal. However, four bands are selected for the analysis, which is cost-effective and ensures better accuracy in transferring the research results Pérez-García et al. (2023).

The metrics performance is high across all datasets and for the different combinations of the model (0.690–0.959; see Table 1), validating the model adaptability. This substantiates that combining the SFS feature selection model with the RF classifier is the most effective. Therefore, the rest of the analysis concentrates on the results obtained using four bands and the SFS-RF method.

Fig. 3 also shows the confusion matrices for the three datasets, illustrating the performance of the optimized SFS-RF model with the four best bands for each dataset. Across all datasets, the classes with the poorest performance are HDPE and LDPE, between 9 % and 35 % of mutual misclassification. These results are consistent as both are polyethylene materials of different densities and are semi-transparent. The WUR dataset also identifies a 13 % of misclassification between HDPE and PP. Similar results are found in the HD datasets when including the background classes of the two datasets: seaweed, dry sand, wet sand, and rocks. Fig. 4 shows that all the backgrounds exceed 90 % accuracy, except for the rocks that achieve 89 % accuracy.

Combining SFS and RF models yields superior results for selecting key bands. The dataset with the highest performance with 4 bands is HD20, reaching 95.9 % OAC, 95.9 % F1-score, and 94.6 % κ . HD21

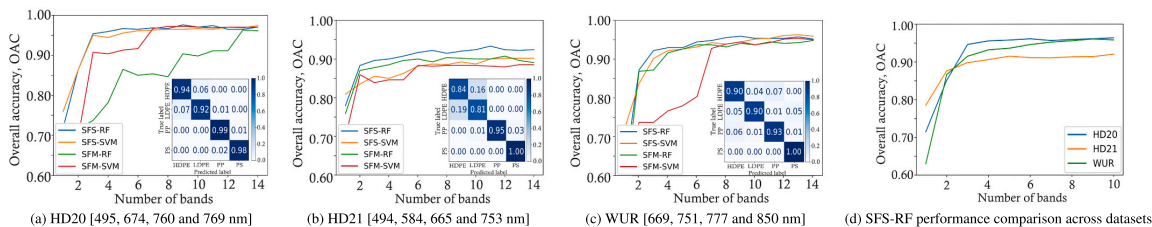


Fig. 3. Overall accuracy of the model combination and confusion matrices for four bands per dataset.

Table 1
Metrics for all models with four bands in the VNIR.

		SFS			SFM		
		OAC	F1	κ	OAC	F1	κ
HD20	RF	0.959	0.959	0.946	0.781	0.781	0.708
	SVM	0.944	0.944	0.926	0.904	0.904	0.872
HD21	RF	0.900	0.900	0.867	0.885	0.885	0.847
	SVM	0.850	0.849	0.800	0.846	0.846	0.795
WUR	RF	0.930	0.929	0.906	0.917	0.917	0.889
	SVM	0.922	0.922	0.896	0.767	0.758	0.690

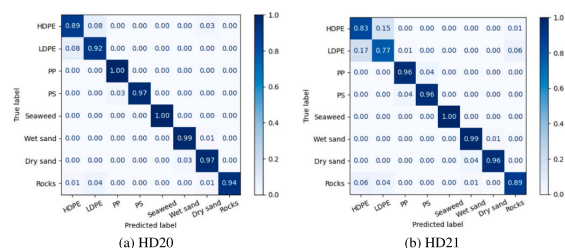


Fig. 4. HD dataset with backgrounds' confusion matrix (SFS-RF 4 bands).

exhibits the lowest performance, with 90.0 % OAC, 90.0 % F1-score, and 86.7 % κ . Moreover, distinguishing between the two densities of transparent polyethylene, HDPE and LDPE, and the rock background poses the most significant challenge in the individual dataset analysis. Section 3.2 discusses the transferability of results and trained models from one dataset to another.

3.2. Experiment 2: transfer learning

When applying a model across different scenarios, its transferability becomes crucial. The greater the model transferability, the broader its range of applications and the lower the computational costs by minimizing retraining efforts.

The initial step requires assessing the transferability of bands, i.e. whether the information resulting from training the model with one dataset can be extended to another without significant accuracy loss. We grouped the wavelengths into 25 nm widths to visualise the results. Fig. 5 shows the number of bands of interest in each designated spectral range. The greatest concentration of bands of interest where the three datasets coincide is in the NIR, between 750 and 800 nm, and in the red, around 650 nm. The two HD datasets also agree that the blue wavelengths between 475 and 500 nm provide relevant information. Finally, for HD21 yellow is of interest, concretely at 584 nm, and another band

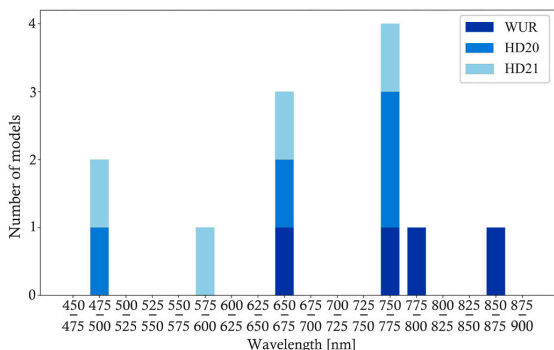


Fig. 5. First four bands of interest for each dataset.

appears in the NIR for WUR at 850 nm. Therefore, we can cover 9 out of the 12 bands of interest in the datasets using a multispectral camera with three bands in the spectral regions of coincidence—475-500 nm, 650-675 nm and 750-775 nm—, demonstrating band transferability.

In general, using the same dataset for both training and validation produces optimal results, as shown in Table 2 (by rows). The two HD datasets have the same plastics in different backgrounds (sand and pebbles). Training with 2021 and validating with 2020 gives better results than training and validating with 2021. The OAC suggests superior transfer occurs when training the model with the most heterogeneous dataset, WUR. This finding was unanticipated because both HD datasets use identical plastics.

The next step requires transferring the complete model and providing only the values of the validation dataset into the already trained classifier. When training with HD20 and transferring to HD21, the model achieves 80.8 % of OAC, while transferring from HD21 to HD20 results in 70.5 %. However, when transferring between HD and WUR datasets, the OAC varies between 25 % and 30 %, potentially attributable to the normalization of WUR spectra contrasted with the absence of normalization in HD spectra. Therefore, this phase is more complex to implement successfully and is more dependent on the dataset.

While band transfer proves effective, model transfer encounters certain limitations. Section 3.3 evaluates whether these limitations restrict its use to identical plastics or allow for broader application in a case study.

3.3. Experiment 3: case study

The final evaluation of the model's applicability involves providing it with entirely novel data, employing the dataset produced with everyday plastics. Fig. 6 (a) illustrates the everyday objects that constitute this dataset. As several objects lack the polymer identification code or recycling number standardized by ASTM (American Society for Testing and Materials), only the ones identified were used to validate the model: HDPE (no. 5, 8), LDPE (no. 13), PP (no. 11, 14), PS (no. 9, 15), with between 5500 and 7000 pixels per plastic type. Fig. 6 also shows the signatures of the objects used for the case study, with a distinct pattern for each plastic type.

Transferring the WUR SFS-RF model with four bands to the new dataset reaches 54.4 % accuracy, higher than that obtained for HD20 and HD21, 47 % and 41 %, respectively. Using the four bands of interest determined with the optimized SFS-RF model for any of the three datasets achieves an accuracy above 90 % in the new dataset. The confusion matrix in Fig. 6 (b) shows high performance, misclassifying only a few HDPE and PP pixels, which are the classes with the most similar spectral signatures and semitransparent in the VNIR range. Consequently, the transfer of results is considered successful.

4. Discussion

Our analysis provides a positive outlook for band transfer and classifying macroplastics in aquatic and coastal environments. Integrating SFS and RF models facilitates the optimal selection of bands of interest. The coincidence of the spectral regions of interest across datasets of different characteristics, coupled with the high accuracy (above 85 %) in terms of the number of bands employed and the transferability of the

Table 2
OAC for SFS-RF with four band transfer.

Dataset validating the model	Datasets providing the bands		
	HD20	HD21	WUR
HD20	0.959	0.902	0.911
HD21	0.889	0.900	0.891
WUR	0.869	0.889	0.930

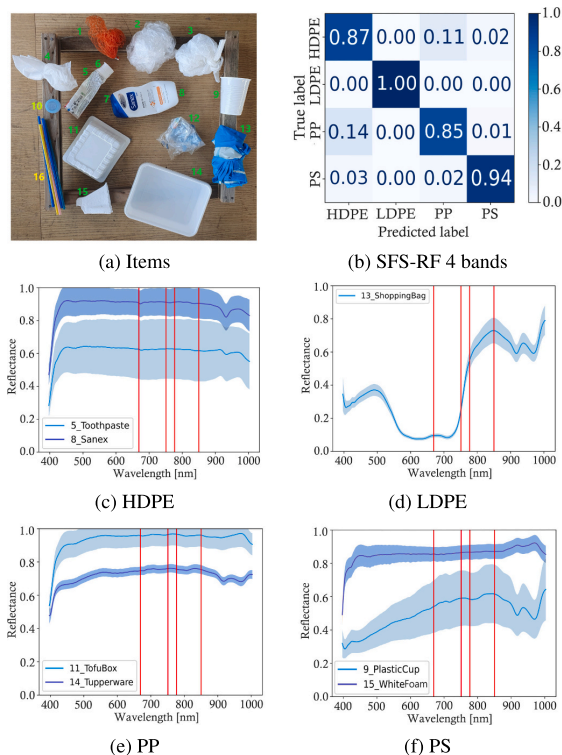


Fig. 6. Spectral analysis of the new dataset: objects, mean spectral signature with red lines indicating WUR best bands. (For interpretation of the references to colour in this figure legend, the reader is referred to the web version of this article.)

bands between datasets, enhances the sensor feasibility regarding efficiency.

The findings in Section 3.1 suggest that accuracy improves when the background is spectrally uniform, such as a sandy beach, where the spectral response is consistent across the area. This is particularly relevant due to the semi-transparent nature of some plastics. In contrast, a heterogeneous background, such as a pebble beach, introduces variability in light reflection both between and within individual pebbles, which introduces noise that hinders the identification of objects. Accordingly, HD21 exhibits the least favourable results in the study with 86.7 % κ . The HDPE and LDPE are usually semi-transparent, making them particularly susceptible to misclassification, reaching 35 % when both added in HD21.

The significance of a uniform background is evident in achieving better results, as also observed in Section 3.2. Training the model with HD20 and validating in HD21 outperforms the outcomes obtained when training and validating with the latter dataset. Training the model with heterogeneous objects helps to improve the transfer of the bands of interest, reducing the risk of the model overfitting. Despite the expectation of better band transfer between HD datasets due to the shared objects, the transfer from WUR to HD outperforms it, suggesting that incorporating heterogeneous objects is a valuable strategy for reducing overfitting.

The successful transfer of bands in the use case in Section 3.3, with an accuracy above 90 %, highlights the validity of the model and the conducted experiments. Since the bands of interest were determined by training the model on a different dataset, it is expected that they may not perfectly align with the spectral signatures of the new dataset. However,

the robustness of the RF classifier allows it to effectively manage the classification of the limited number of objects in the study.

The main limitation lies in the model transfer. Although the accuracy exceeds 50 %, indicating promising performance, it also highlights that achieving high precision when transferring models between different datasets remains a challenge. Another limitation is that object colour can influence its spectral signature in the visible range, potentially leading to false positives or misclassification, particularly with darker-coloured plastics and transparent materials Zhu et al. (2020); Tasseron et al. (2022). Also, the reflectance of floating plastics is highly sensitive to plastic type, transparency, shape, and surface characteristics Martínez-Vicente et al. (2019); this effect is less pronounced for plastics on land. Our study focuses on light-coloured plastics found on land, where these issues are less significant and are not directly addressed. Future research could benefit from expanding the number of datasets and conducting more band transfers to datasets with varied backgrounds. This approach would help avoid overfitting the model to specific data, thereby improving the model transferability to other scenarios.

Within the context of previous research, several studies have explored the detection of macroplastics using similar RS techniques Topouzelis et al. (2021). In contrast to other SWIR-focused work Tasseron et al. (2022), our emphasis on the VNIR range explores the possibility of developing efficient, low-cost sensors. Several studies suggest that a high level of spectral detail is unnecessary for detecting and classifying other pollutants with gradually changing spectral signatures, indicating that sensors with broader bands could still provide reliable classification Legleiter et al. (2019, 2022). Our pipeline, which integrates various classification and feature selection models, enhances the methodology’s effectiveness, surpassing other band selection techniques that need between 10 and 20 bands to achieve optimum accuracy Olyaei and Ebtehaj (2024).

To summarise, our findings contribute to a better understanding of plastics’ spectral behaviour. The experiments’ results advocate the feasibility of transferring bands of interest from one dataset to another for efficient macroplastic identification, highlighting the importance of training with heterogeneous datasets and uniform backgrounds.

5. Conclusion

This letter provides fundamental input for transferring classifiers across datasets to identify the key bands for detecting plastic pollution in aquatic environments. Integrating SFS and RF models optimizes band selection, enhancing sensor feasibility. Uniform backgrounds prove crucial for accurate detection, as seen in the individual findings, with successful differentiation of all polymers and backgrounds. Successful band transfers between datasets, with an accuracy of 90 %, highlight model validity. However, analysis of model transfer is limited, requiring classifier retraining in each dataset to achieve accuracy above 60 %. Consequently, while successful band transfers suggest the potential to develop a sensor capable of detecting plastics across various scenarios, the insufficient precision in model transfer indicates that the classifier must be trained for each scene. The study suggests expanding datasets to address limitations and improve model transferability. For optimal adaptability to various plastics, it is recommended to use a combination of bands from the three main datasets to cover different regions of the spectrum, with the sensor bands centred at 495 nm (blue), 665 nm (red), 777 nm (NIR) and 850 nm (NIR). In the near future, we will explore the effect of several multispectral sensor bandwidths on plastic classification and transferability to non-virgin plastics. In summary, these findings contribute to understanding the spectral behaviour of plastics and the effectiveness of band and model transfer, advocating for developing more targeted and adaptable remote sensing technologies for efficient plastic detection across diverse aquatic environments.

CRedit authorship contribution statement

Ámbar Pérez-García: Writing – review & editing, Writing – original draft, Visualization, Validation, Software, Methodology, Investigation, Formal analysis, Conceptualization. **Tim H.M. van Emmerik:** Writing – review & editing, Visualization, Supervision, Resources, Methodology, Conceptualization. **Aser Mata:** Writing – review & editing, Supervision, Resources, Conceptualization. **Paolo F. Tasserón:** Writing – review & editing, Data curation. **José F. López:** Writing – review & editing, Supervision, Resources, Project administration, Funding acquisition.

Declaration of generative AI and AI-assisted technologies in the writing process

While preparing this work, the authors used ChatGPT and Grammarly to improve the clarity and coherence of writing. The authors reviewed and edited the content as needed and took full responsibility for the publication's content.

Declaration of competing interest

The authors declare that they have no known competing financial interests or personal relationships that could have appeared to influence the work reported in this paper.

Data availability

The HD data collected are available at the CEDA Archive: HD20 is <https://doi.org/10.5285/2485214239134768820ffb50fb5513bc> and HD21 is <https://doi.org/10.5285/e0f6a223220d463ea7a5d2a7520000cf>. The WUR database is available online at <https://doi.org/10.4121/14518278> (accessed on 4TU.ResearchData). The case study data will be made available on request.

Acknowledgements

This work was completed while Ámbar Pérez-García was beneficiary of a predoctoral grant given by the “Agencia Canaria de Investigación, Innovación y Sociedad de la Información (ACIISI)” of the “Consejería de Universidades, Ciencia e Innovación y Cultura”, part-financed by the European Social Fund Plus (FSE+) “Programa Operativo Integrado de Canarias 2021-2027, Eje 3 Tema Prioritario 74 (85%)”. We would also like to thank the OASIS-HARMONIE project, under contract PID2023-148285OB-C43 from “Proyectos de Generación de Conocimiento” 2023 and the PERSEO project, under contract CPP2021-008527, from “Programa de Colaboración Público-Privada” of “Gobierno de España”, 2023-2025. We also extend our gratitude to the reviewers for their valuable insights.

References

Andrady, A.L., 2011. Microplastics in the marine environment. *Mar. Pollut. Bull.* 62, 1596–1605.

Andriolo, U., Topouzelis, K., van Emmerik, T.H., Papakostantinou, A., Monteiro, J.G., Isobe, A., Hidaka, M., Kako, S., Kataoka, T., Gonçalves, G., 2023. Drones for litter monitoring on coasts and rivers: suitable flight altitude and image resolution. *Mar. Pollut. Bull.* 195, 115521.

Armitage, S., Awty-Carroll, K., Clewley, D., Martínez-Vicente, V., 2022. Detection and classification of floating plastic litter using a vessel-mounted video camera and deep learning. *Remote Sens. (Basel)* 14. <https://doi.org/10.3390/rs14143425>.

Barry, J., Rindorf, A., Gago, J., Silburn, B., McGoran, A., Russell, J., 2023. Top 10 marine litter items on the seafloor in european seas from 2012 to 2020. *Sci. Total Environ.* 902, 165997 <https://doi.org/10.1016/j.scitotenv.2023.165997>.

Biermann, L., Clewley, D., Martínez-Vicente, V., Topouzelis, K., 2020. Finding plastic patches in coastal waters using optical satellite data. *Sci. Rep.* 10, 5364.

Boughorbel, S., Jarray, F., El-Anbari, M., 2017. Optimal classifier for imbalanced data using Matthews correlation coefficient metric. *PLoS One* 12, e0177678.

Cohen, J., 1960. A coefficient of agreement for nominal scales. *Educ. Psychol. Meas.* 20, 37–46.

Cortesi, I., 2021. Artificial intelligence applied to multispectral imagery for fluvial macroplastics detection, in: Proceedings of the joint international event 9th ARQUEOLÓGICA 2.0 & 3rd GEORES, pp. 495–497.

Cózar, A., Arias, M., Suarías, G., Viejo, J., Aliani, S., Koutroulis, A., Delaney, J., Bonnelly, G., Macías, D., de Vries, R., et al., 2024. Proof of concept for a new sensor to monitor marine litter from space. *Nat. Commun.* 15, 4637.

van Emmerik, T.H., Kirschke, S., Schreyers, L.J., Nath, S., Schmidt, C., Wendt-Potthoff, K., 2023. Estimating plastic pollution in rivers through harmonized monitoring strategies. *Mar. Pollut. Bull.* 196, 115503.

Garaba, S.P., Dierssen, H.M., 2020. Hyperspectral ultraviolet to shortwave infrared characteristics of marine-harvested, washed-ashore and virgin plastics. *Earth System Science Data* 12, 77–86. <https://doi.org/10.5194/essd-12-77-2020>.

Hearst, M., Dumais, S., Osuna, E., Platt, J., Scholkopf, B., 1998. Support vector machines. *IEEE Intelligent Systems and their Applications* 13, 18–28. <https://doi.org/10.1109/5254.708428>.

Ho, T.K., 1995. Random decision forests, in: proceedings of 3rd international conference on document analysis and recognition, 1, 278–282. <https://doi.org/10.1109/ICDAR.1995.598994>.

Hossin, M., Sulaiman, M.N., 2015. A review on evaluation metrics for data classification evaluations. *International journal of data mining & knowledge management process* 5, 1.

Jambeck, J.R., Geyer, R., Wilcox, C., Siegler, T.R., Perryman, M., Andrady, A., Narayan, R., Law, K.L., 2015. Plastic waste inputs from land into the ocean. *Science* 347, 768–771.

Kikaki, K., Kakogeorgiou, I., Mikeli, P., Raitos, D.E., Karantzalos, K., 2022. Marida: a benchmark for marine debris detection from sentinel-2 remote sensing data. *PLoS One* 17, e0262247.

Kramer, O., 2016. Scikit-learn. *Machine learning for evolution strategies* 45–53.

Kremer, M., Kristollari, V., Karathanassi, V., Topouzelis, K., Kolokoussis, P., Taggio, N., Aiello, A., Ceriola, G., Barbone, E., Corradi, P., 2022. Increasing the sentinel-2 potential for marine plastic litter monitoring through image fusion techniques. *Mar. Pollut. Bull.* 182, 113974.

Lebreton, L., Slat, B., Ferrari, F., Sainte-Rose, B., Aitken, J., Marthouse, R., Hajbane, S., Cunsolo, S., Schwarz, A., Levivier, A., et al., 2018. Evidence that the great pacific garbage patch is rapidly accumulating plastic. *Sci. Rep.* 8, 1–15.

Legleiter, C.J., Manley, P.V., Erwin, S.O., Bulliner, E.A., 2019. An experimental evaluation of the feasibility of inferring concentrations of a visible tracer dye from remotely sensed data in turbid rivers. *Remote Sens. (Basel)* 12, 57.

Legleiter, C.J., Sansom, B.J., Jacobson, R.B., 2022. Remote sensing of visible dye concentrations during a tracer experiment on a large, turbid river. *Water Resour. Res.* 58, e2021WR031396.

van Lieshout, C., van Oeveren, K., van Emmerik, T., Postma, E., 2020. Automated river plastic monitoring using deep learning and cameras. *Earth and space science* 7, e2019EA000960.

Martínez-Vicente, V., Clark, J.R., Corradi, P., Aliani, S., Arias, M., Bochow, M., Bonnelly, G., Cole, M., Cózar, A., Donnelly, R., Echevarría, F., Galgani, F., Garaba, S. P., Goddijn-Murphy, L., Lebreton, L., Leslie, H.A., Lindeque, P.K., Maximenko, N., Martin-Lauzer, F.R., Moller, D., Murphy, P., Palombi, L., Raimondi, V., Reisser, J., Romero, L., Simis, S.G., Sterckx, S., Thompson, R.C., Topouzelis, K.N., van Sebille, E., Veiga, J.M., Vethaak, A.D., 2019. Measuring marine plastic debris from space: initial assessment of observation requirements. *Remote Sensing* 11. <https://www.mdpi.com/2072-4292/11/20/2443>. <https://doi.org/10.3390/rs11202443>.

Meijer, L.J., Van Emmerik, T., Van Der Ent, R., Schmidt, C., Lebreton, L., 2021. More than 1000 rivers account for 80% of global riverine plastic emissions into the ocean. *Science. Advances* 7, eaaz5803.

Morales-Caselles, C., Viejo, J., Martí, E., González-Fernández, D., Pragnell-Raasch, H., González-Gordillo, J.I., Montero, E., Arroyo, G.M., Hanke, G., Salvo, V.S., et al., 2021. An inshore-offshore sorting system revealed from global classification of ocean litter. *Nature Sustainability* 4, 484–493.

Olyaei, M., Ebtahaj, A., 2024. Uncovering plastic litter spectral signatures: a comparative study of hyperspectral band selection algorithms. *Remote Sens. (Basel)* 16. <https://doi.org/10.3390/rs16010172>.

Papageorgiou, D., Topouzelis, K., Suarías, G., Aliani, S., Corradi, P., 2022. Sentinel-2 detection of floating marine litter targets with partial spectral unmixing and spectral comparison with other floating materials (plastic litter project 2021). *Remote Sens. (Basel)* 14, 5997.

Pérez-García, Á., Rodríguez-Molina, A., Hernández, E., Vera, L., López, J.F., 2023. Development of low-cost multi-spectral cameras for precision agriculture. *IGARSS 2023–2023 IEEE International Geoscience and Remote Sensing Symposium* 3466–3469. <https://doi.org/10.1109/IGARSS25108.2023.10282072>.

Pérez-García, Á., Lorenzo, A.M., López, J., 2024a. Spectral band selection methodology for future sensor development. 2024 47th MIPRO ICT and electronics convention (MIPRO) 152–156. <https://doi.org/10.1109/MIPRO60963.2024.10569699>.

Pérez-García, Á., Martín Lorenzo, A., Hernández, E., Rodríguez-Molina, A., van Emmerik, T.H.M., López, J.F., 2024b. Developing a generalizable spectral classifier for rhodamine detection in aquatic environments. *Remote Sens. (Basel)* 16, 1–18. <https://doi.org/10.3390/rs16163090>.

Headwall Photonics, 2020. Spectral imaging instruments. <https://www.headwallphotonics.com>. [online; accessed 22-Jun-2020].

Plymouth Marine Laboratory, Mata, A., 2023a. Hyperdrone flight 20200929 - hyperspectral in situ radiometry and hyperspectral imagery at different altitudes for plastics detection. NERC EDS Centre for Environmental Data Analysis. <https://doi.org/10.5285/2485214239134768820ffb50fb5513bc>.

Plymouth Marine Laboratory, Mata, A., 2023b. Hyperdrone flight 20210722 - hyperspectral in situ radiometry and hyperspectral imagery at different altitudes for

- plastics detection. NERC EDS Centre for Environmental Data Analysis. <https://doi.org/10.5285/e0f6a223220d463ea7a5d2a7520000cf>.
- Rochman, C.M., Hoh, E., Hentschel, B.T., Kaye, S., 2013. Long-term field measurement of sorption of organic contaminants to five types of plastic pellets: implications for plastic marine debris. *Environ. Sci. Technol.* 47, 1646–1654.
- Rußwurm, M., Venkatesa, S.J., Tuia, D., 2023. Large-scale detection of marine debris in coastal areas with sentinel-2. *iScience*.
- Schreyers, L., van Emmerik, T., Biermann, L., van der Ploeg, M., 2022. Direct and indirect river plastic detection from space. *IGARSS 2022–2022 IEEE International Geoscience and Remote Sensing Symposium* 5539–5542. <https://doi.org/10.1109/IGARSS46834.2022.9883379>.
- Schwarz, A., Ligthart, T., Boukris, E., Van Harmelen, T., 2019. Sources, transport, and accumulation of different types of plastic litter in aquatic environments: a review study. *Mar. Pollut. Bull.* 143, 92–100.
- Specim Spectral Imaging, 2019. FX Series hyperspectral cameras. <http://www.specim.fi/fx/>. [Online; accessed 06-Oct-2019].
- Syakur, M., Khotimah, B., Rochman, E., Satoto, B.D., 2018. Integration k-means clustering method and elbow method for identification of the best customer profile cluster. *IOP conference series: materials science and engineering*, IOP publishing 336, 012017.
- Tasseron, P., van Emmerik, T., Peller, J., Schreyers, L., Biermann, L., 2021a. Advancing floating macroplastic detection from space using experimental hyperspectral imagery. *Remote Sens. (Basel)* 13. <https://doi.org/10.3390/rs13122335>.
- Tasseron, P., van Emmerik, T., Schreyers, L., Biermann, L., Peller, J., 2021b. Hyperspectral plastics dataset supplementary to the paper 'advancing floating plastic detection from space using hyperspectral imagery'. 4TU.ResearchData. <https://doi.org/10.4121/14518278.V3>.
- Tasseron, P.F., Schreyers, L., Peller, J., Biermann, L., van Emmerik, T., 2022. Toward robust river plastic detection: combining lab and field-based hyperspectral imagery. *Earth and space. Science* 9, e2022EA002518.
- Tasseron, P.F., van Emmerik, T.H., Vriend, P., Hauk, R., Alberti, F., Mellink, Y., van der Ploeg, M., 2024. Defining plastic pollution hotspots. *Sci. Total Environ.* 934, 173294 <https://doi.org/10.1016/j.scitotenv.2024.173294>.
- Topouzelis, K., Papageorgiou, D., Suaria, G., Aliani, S., 2021. Floating marine litter detection algorithms and techniques using optical remote sensing data: a review. *Mar. Pollut. Bull.* 170, 112675 <https://doi.org/10.1016/j.marpolbul.2021.112675>.
- Zhu, C., Kanaya, Y., Nakajima, R., Tsuchiya, M., Nomaki, H., Kitahashi, T., Fujikura, K., 2020. Characterization of microplastics on filter substrates based on hyperspectral imaging: laboratory assessments. *Environ. Pollut.* 263, 114296 <https://doi.org/10.1016/j.envpol.2020.114296>.

3.2 Developing a Generalizable Spectral Classifier for Rhodamine Detection in Aquatic Environments

- **Á. Pérez-García**, A. Martín Lorenzo, E. Hernández, A. Rodríguez-Molina, T.H.M. van Emmerik and J. F. López, “Developing a Generalizable Spectral Classifier for Rhodamine Detection in Aquatic Environments,” *Remote Sensing*, vol. 16, pp. 1-18, 2024, Art no. 3090.
- DOI: [10.3390/rs16163090](https://doi.org/10.3390/rs16163090)
- This article belongs to the Special Issue Coastal and Littoral Observation Using Remote Sensing of MDPI Remote Sensing.
- Publisher: MDPI.
- ISSN: 2072-4292
- Journal metrics:
 - 2023 Journal Impact Factor: 4.2.
 - Journal Citation Indicator (JCI): 0.97.
 - Rank by Journal Impact Factor:
 - * **Q1**: Geoscience, Multidisciplinary.
 - * **Q2**: Remote Sensing; Environmental Sciences; Imaging Science & Photographic Technology.

Article

Developing a Generalizable Spectral Classifier for Rhodamine Detection in Aquatic Environments

Ámbar Pérez-García ^{1,*}, Alba Martín Lorenzo ¹, Emma Hernández ¹, Adrián Rodríguez-Molina ¹,
Tim H. M. van Emmerik ² and José F. López ¹

¹ Institute for Applied Microelectronics, University of Las Palmas de Gran Canaria, 35001 Las Palmas, Spain; alba.martin12@alu.ulpgc.es (A.M.L.); ehernandez@iuma.ulpgc.es (E.H.); armolina@iuma.ulpgc.es (A.R.-M.); lopez@iuma.ulpgc.es (J.F.L.)

² Hydrology and Environmental Hydraulics Group, Wageningen University, 6708 BP Wageningen, The Netherlands; tim.vanemmerik@wur.nl

* Correspondence: ambar.perez@ulpgc.es

Abstract: In environmental studies, rhodamine dyes are commonly used to trace water movements and pollutant dispersion. Remote sensing techniques offer a promising approach to detecting rhodamine and estimating its concentration, enhancing our understanding of water dynamics. However, research is needed to address more complex environments, particularly optically shallow waters, where bottom reflectance can significantly influence the spectral response of the rhodamine. Therefore, this study proposes a novel approach: transferring pre-trained classifiers to develop a generalizable method across different environmental conditions without the need for in situ calibration. Various samples incorporating distilled and seawater on light and dark backgrounds were analyzed. Spectral analysis identified critical detection regions (400–500 nm and 550–650 nm) for estimating rhodamine concentration. Significant spectral variations were observed between light and dark backgrounds, highlighting the necessity for precise background characterization in shallow waters. Enhanced by the Sequential Feature Selector, classification models achieved robust accuracy (>90%) in distinguishing rhodamine concentrations, particularly effective under controlled laboratory conditions. While band transfer was successful (>80%), the transfer of pre-trained models posed a challenge. Strategies such as combining diverse sample sets and applying the first derivative prevent overfitting and improved model generalizability, surpassing 85% accuracy across three of the four scenarios. Therefore, the methodology provides us with a generalizable classifier that can be used across various scenarios without requiring recalibration. Future research aims to expand dataset variability and enhance model applicability across diverse environmental conditions, thereby advancing remote sensing capabilities in water dynamics, environmental monitoring and pollution control.

Keywords: dye tracking; rhodamine; artificial intelligence; band selection



Citation: Pérez-García, Á.; Martín Lorenzo, A.; Hernández, E.; Rodríguez-Molina, A.; van Emmerik, T.H.M.; López, J.F. Developing a Generalizable Spectral Classifier for Rhodamine Detection in Aquatic Environments. *Remote Sens.* **2024**, *16*, 3090. <https://doi.org/10.3390/rs16163090>

Academic Editor: Akira Iwasaki

Received: 30 June 2024

Revised: 9 August 2024

Accepted: 15 August 2024

Published: 22 August 2024



Copyright: © 2024 by the authors. Licensee MDPI, Basel, Switzerland. This article is an open access article distributed under the terms and conditions of the Creative Commons Attribution (CC BY) license (<https://creativecommons.org/licenses/by/4.0/>).

1. Introduction

Understanding the water movement and particle transport in the ocean and rivers is crucial for giving a fast response to environmental disasters. Although numerous mathematical models predict how these agents are transported, they often come with high computational costs and may not be adaptable to the highly variable conditions encountered in real-world scenarios, limiting their effectiveness for quick responses [1]. Thus, to understand and track hazardous agents in oceans and waterways, new techniques and tools are necessary [2].

Dye tracers offer a simpler and effective solution. They are widely used to study the transport and dispersion of particles in aqueous environments, such as in the ocean [3], coastal areas [4,5], rivers [6], and lakes [7]. Rhodamine is a synthetic dye commonly used as a tracer in environmental studies due to its distinctive colour and high visibility. Its applications include monitoring water flow, tracking pollutant dispersion, and studying

hydrodynamic processes in aquatic environments. Rhodamine is a key tool for understanding complex water movement and contamination patterns. Current methods of measuring rhodamine concentration involve collecting samples for later laboratory analysis [8] or using fluorimeters for in situ measurements [9]. However, these techniques are costly and spatially limited, capturing information only at the local levels [10]. In this context, aerial and near-field remote sensing emerges as a promising alternative, offering greater spatial coverage than traditional in situ sampling methods [11].

Multispectral and hyperspectral remote sensing have proven to be effective in detecting and mapping the concentrations of dye tracers in aquatic environments [12]. Several studies successfully utilized multispectral and hyperspectral sensors onboard piloted aerial platforms to identify rhodamine, also in diverse aquatic environments, including the ocean [13–15], coasts [16], rivers [10,17], and lakes [1]. Some studies focused on comparing the intensity of RGB images [18,19], while others utilized hyperspectral sensors to capture surface reflectance [20]. Combining spectral technology with the emerging use of uncrewed aerial vehicles (UAVs) allows for conducting studies in much detail, with greater flexibility and detecting patterns at sub-meter resolution [12]. In addition, the development of lighter and more specialized optical sensors represents an opportunity to have a sensor with specialized spectral bands for rhodamine detection and concentration estimation at a low price [21].

Despite these advancements, several knowledge gaps remain. The widely used Optimum Band Ratio Analysis (OBRA) [10,22] method for selecting bands in hyperspectral and multispectral sensors to detect rhodamine requires in situ concentration measurements for calibration, limiting its transferability to different locations. Furthermore, most rhodamine studies are conducted in controlled environments, such as experimental channels, water tanks, or deep lakes, where the impact of background reflections is minimized (optically deep waters) [12]. Only a few studies have analyzed real-world scenarios, such as rivers with varying degrees of turbidity or optically shallow waters where the bottom reflects light [12,22]. The optical characterization of rhodamine in aquatic environments presents several challenges, especially in coastal areas, shallow rivers or turbid environments. As a semi-transparent solution, its spectral signature captured by sensors is influenced by the optical properties of suspended components and background reflections. However, more in-depth work is needed to understand the effect of water properties and bottom reflections of optically shallow waters on rhodamine's spectral signature and the transferability of detection models across varied conditions.

In this study, we conducted experiments to measure rhodamine concentrations with the goal of improving detection methods. We first spectrally analyzed the rhodamine in the laboratory with different backgrounds and water types. Using artificial intelligence algorithms, specifically Sequential Feature Selection (SFS) and Random Forest (RF) models, we identified the key spectral bands for rhodamine detection and concentration estimation. We then evaluated the transferability of these bands and the trained classifiers across different water types and backgrounds. This approach aimed to minimize the need for in situ calibration and enhance the robustness of detection models.

In our paper, we present the identification of key spectral bands for rhodamine estimation, the influence of background types on spectral signatures, and the transferability of detection models. We found that combining all samples to train the classification model, and also applying the first derivative [23] to favor the distinction of spectral signatures, improved the transfer of the models to all samples. These findings provide valuable insights for developing effective and affordable remote sensing tools to monitor rhodamine and, by extension, other pollutants in aquatic environments, especially in optically shallow waters. This research is particularly significant, as it supports the development of low-cost, multispectral cameras for environmental monitoring, contributing to more efficient and scalable pollution reduction strategies.

2. Materials and Methods

The methodology followed in this experiment can be divided into preparing the rhodamine samples, performing their spectral analysis, and employing the band selection methodology for classifying rhodamine concentrations. Rhodamine samples were prepared in beakers with distilled and seawater at concentrations of 1 mg/L, 15 mg/L, and 30 mg/L. The spectral signatures of samples on two different backgrounds were obtained with hyperspectral cameras. The spectral signatures of each concentration were provided to the band selection algorithm to obtain the most influential bands for classifying the rhodamine concentration.

2.1. Rhodamine Samples

The Rhodamine Water Tracer, hereafter referred to as rhodamine, is a fluorescent dye primarily used as a tracer in aquatic environments. The company Elittoral [24] from Las Palmas de Gran Canaria, Spain, has procured the rhodamine from ThermoFisher Scientific [25] from Massachusetts, USA, identified by the chemical codes CAS 37299-86-8 and 7732-18-5, with catalogue number 446971000. Initially, the rhodamine is highly concentrated at 20%, or 200 g/L, requiring dilution in water to achieve an appropriate concentration for its discharge into the sea. The beakers are from Labbox [26] in Barcelona, Spain, reference BKT3-250-012. They have a measurable volume of 250 mL, an outer diameter of 60 mm, and a height of 123 mm. When the beaker is filled with 250 mL of liquid, the height of the fluid will be 100 mm.

This study uses 250 mL solutions of seawater and distilled water with varying concentrations of rhodamine provided by Elittoral. Solutions with different concentrations of rhodamine are produced: 1 mg/L, 15 mg/L, and 30 mg/L (Figure 1). In addition to the rhodamine dilutions, pure seawater and distilled water samples are also included in the study. These pure samples serve as reference spectra and are essential for the comparative analysis of rhodamine-contaminated samples.

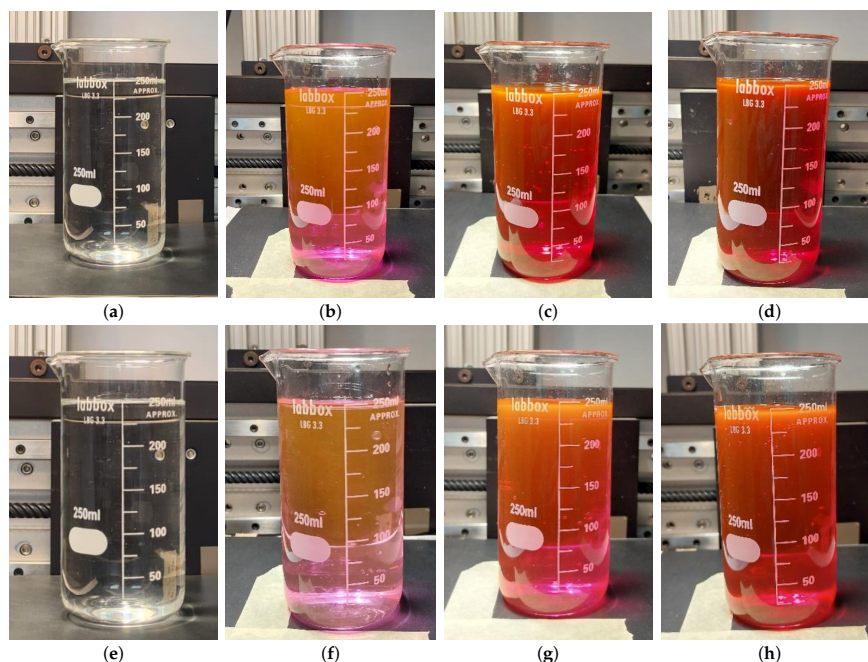


Figure 1. Rhodamine samples for distilled and seawater at different concentrations. (a) Distilled 0 mg/L; (b) Distilled 1 mg/L; (c) Distilled 15 mg/L; (d) Distilled 30 mg/L; (e) Seawater 0 mg/L; (f) Seawater 1 mg/L; (g) Seawater 15 mg/L; (h) Seawater 30 mg/L.

Hyperspectral signatures of all samples were collected over two different backgrounds. Since the rhodamine solutions are semi-transparent, the background signature likely influences the signature captured by the sensor. We placed two backgrounds underneath the beaker to observe these differences: a white sheet of paper as the light background and a low-reflective black foam material [27] as the dark background.

2.2. Hyperspectral Setup

We took images of the rhodamine samples in the Hyperspectral Laboratory at IUMA [27] in Las Palmas de Gran Canaria, Spain. The system shown in Figure 2 aims to acquire images with pushbroom hyperspectral cameras. It includes a motorized linear stage for linear motion and a light source emitting uniformly. Illumination comes from a 150 W Quartz Tungsten-Halogen (QTH) lamp with broadband emission between 400 nm and 2500 nm (VIS and NIR spectral range). Images were captured using a Specim FX10 camera (Konica Minolta Company, Oulu, Finland) [28]. The FX10 is a hyperspectral camera covering the visible and near-infrared range (VNIR) from 400 nm to 1000 nm, with 224 bands, a spectral resolution of 5.5 nm, a spatial sampling of 1024 pixels, and a field of view (FoV) of 38 degrees. This spectral range was chosen because rhodamine has the greatest response in the VNIR.

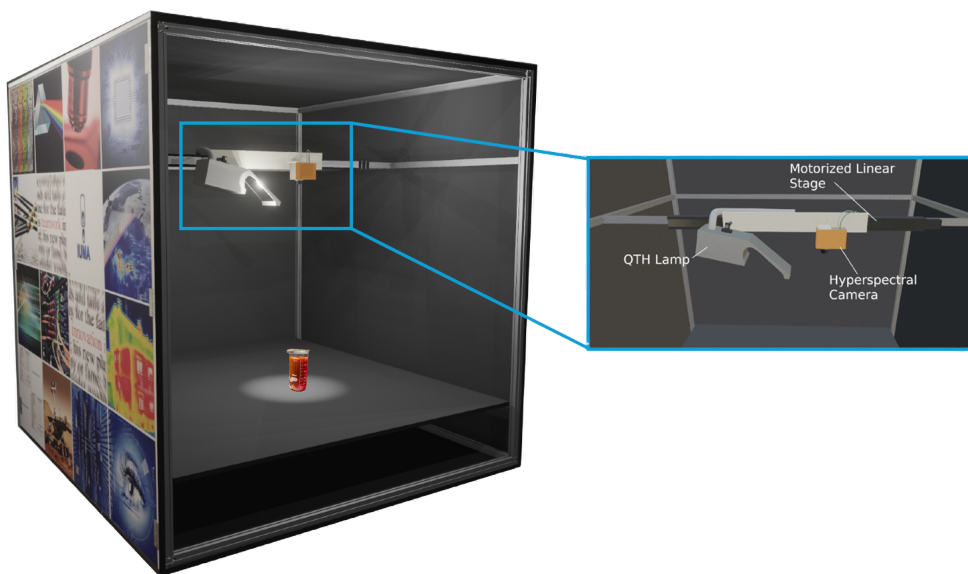


Figure 2. A 3D model of the acquisition system (adapted with permission from [27], under a Creative Commons Attribution (CC BY) 4.0 license. Copyright 2022).

We performed single-point reflectance calibration (Equation (1)) before starting measurements to avoid sensor saturation. This pre-processing involves white and dark (0-photon) references to calculate the reflectance of each pixel from its radiance. The white reference is a high-reflectance Zenith Polymer [29], and the dark reference is obtained by covering the camera lens:

$$\text{reflectance} = \frac{\text{radiance} - \text{dark}}{\text{white} - \text{dark}} \quad (1)$$

The measurements are taken by scanning the FX10 camera over the different beakers. Since the light source is positioned ahead of the camera as shown in Figure 2, this setup produces glints on the beaker, shadows in certain areas, and increased intensity in others due to internal reflections and external refractions of the glass.

The datasets used for the artificial intelligence model are generated by extracting pixels from the bottom areas of the beaker where no glints are present, while avoiding shadows. However, due to the varying brightness within the beaker, the standard deviation of the classes will be high, indicating variation in intensity, though not in the shape of the spectral signature. The number of pixels per class will not be uniform, as shown in Table 1.

Table 1. Number of pixels per class.

	Dark Background		Light Background		Total
	Distilled	Sea	Distilled	Sea	
0 mg/L	346	624	233	299	1502
1 mg/L	857	668	821	545	2891
15 mg/L	1302	406	965	650	3323
30 mg/L	924	346	866	750	2886

Efforts have been made to balance the glints and shadowed areas within the beaker. However, the primary goal of this study was to develop a generalizable classifier, and having data with variability is advantageous, as it better reflects the reality of experimental conditions.

2.3. Methodology

The methodology is divided into training, result analysis, and transfer (Figure 3). During training, data are provided to the band selection model. This model provides evaluation metrics, which are analyzed to determine the optimal number of bands. The band selection model [30] also identifies the best bands and provides pre-trained classifiers for the optimal number of bands. The final stage involves transferring the best bands and pre-trained models to other scenarios to assess their performance and determine if the classifier is generalizable.

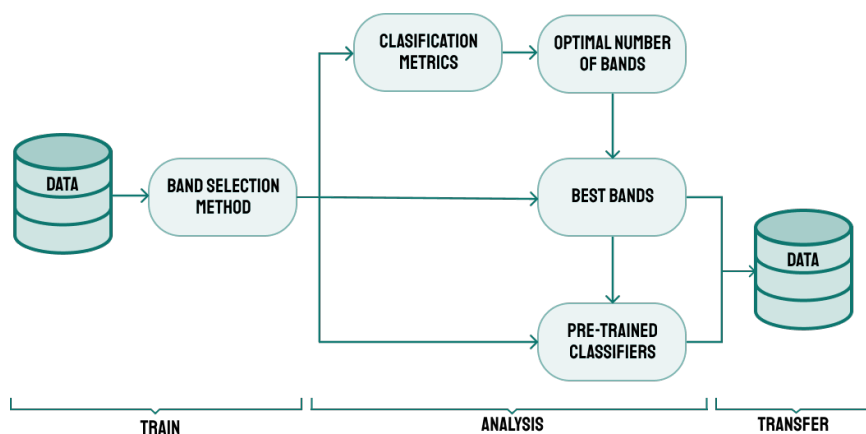


Figure 3. Methodology for transferring results and obtaining a generalizable classifier.

The methodology integrates hyperparameterized classifiers with feature selectors to provide optimized bands of interest for classification [30]. The procedure is illustrated in Figure 4. The data are divided into training sets for the feature selectors and classifiers, as well as a validation set. Employing the information provided by the classifiers, the feature selectors determine the bands of interest. Subsequently, the classifiers are retrained exclusively with these bands. Finally, the performance of the updated classifiers is assessed using the validation dataset to obtain classification metrics.

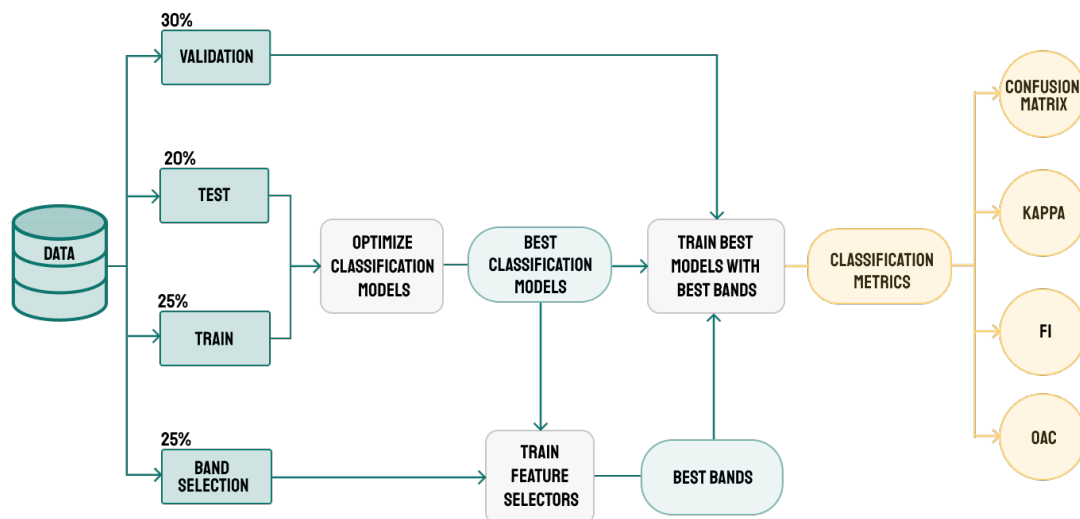


Figure 4. Band selection method (adapted with permission from [30], Copyright 2024, IEEE).

For this study, we combined two feature selectors, Sequential Feature Selector (SFS) and Select From Model (SFM) [31], with three classifiers, Random Forest (RF) [32], Logistic Regression (LR) [33], and Linear Support Vector Machine (SVM) [34]. SFS is a sequential search technique that iteratively adds or removes features to improve the classifier's performance. SFM ranks features based on a model's coefficients or importance, facilitating the selection of efficient feature subsets [31]. RF is a widely used classifier, employing ensemble learning to combine predictions from multiple decision trees [35]. LR is a linear model for binary classification [36]. Linear SVM identifies hyperplanes for optimal class separation [37].

We evaluated the performance of rhodamine concentration classification using the classification metrics on the validation dataset. The overall accuracy (OAC), also called accuracy, represents the proportion of correct predictions out of the total samples [38]. The F1 score is particularly useful with imbalanced class distributions, as it emphasizes the accuracy of the smaller classes [39]. The Kappa statistic (κ) measures inter-rater agreement for categorical items, adjusting for chance agreement, and is particularly relevant for uneven datasets [40]. The confusion matrix provides a detailed decomposition of predicted classification labels versus real labels [41].

The performance of all pairs of feature selectors and classifiers was evaluated for different numbers of bands of the FX10 camera [28]. By plotting the accuracy values for each band on a graph, we were able to use the elbow method [42] to determine the optimal number of bands. This method selects the number of bands at the point where the curve bends, forming an elbow and indicating a slowdown in accuracy improvement [42]. For the optimal number of bands, all classification metrics were calculated.

We also analyzed whether the different feature selector–classifier pairs identify the optimal bands in the same area of the electromagnetic spectrum. For this purpose, we grouped the wavelengths into sections of 25 nm wide for several reasons. First, the spectral signatures of different concentrations of rhodamine are continuous and do not exhibit abrupt changes, making it practical to group the wavelengths for better visualization of large-scale behavior. Second, grouping the bands helps us understand their potential utility in multispectral sensors. The hyperspectral camera used in this study has a spectral resolution of 5.5 nm [28], so it is appropriate to group them, given that multispectral sensors typically have a bandwidth of approximately 20 nm or 30 nm. Third, several studies support that a high level of spectral detail is unnecessary for rhodamine detection, indicating that sensors with broader bands could still provide reliable concentration estimates [20,22].

Finally, we can assess the transferability of the results to different scenarios. We can define different levels of transfer, such as the transfer of the bands of interest or the transfer of pre-trained classification models. Transferring the bands of interest is a straightforward way to transmit part of the knowledge acquired from one sample to another. It involves using the bands identified by the classification model in one scenario to train the classifier (exclusively with those wavelengths) with another scenario, whether it has a different type of water or a different background.

Transferring pre-trained classification models is more complex because these models learn the specific characteristics of each scenario, i.e., the reflectance value of the spectral signature. One strategy that can be employed to improve the transfer of pre-trained models is to provide the classifier with a combination of samples from all types of water and backgrounds for training. Another strategy is calculating the first derivative of the spectral signatures, which helps identify variations and trends in the data, thereby aiding in the differentiation of spectral signatures.

If the spectral behavior is similar enough across different scenarios, it is possible to successfully transfer the models, and the classifiers can be used in multiple scenarios without retraining. This would decrease the required in situ calibration measurements and reduce computational time.

3. Results

3.1. Spectral Analysis—Beaker Influence

An important aspect to consider during the analysis of the results is the influence of the beaker on the spectral signature of its liquid content. The reflections and refractions caused by the glass lead to non-uniform spectral intensity throughout the beaker, resulting in a higher standard deviation in the spectral signatures of each class.

To elaborate on the reflections caused by the beaker, Figure 5 compares the spectral behaviour of the light and dark backgrounds, both with and without the beaker filled with seawater. The results indicate that the primary effect of the background is to modulate the intensity of the reflectance, with greater influence between 400 nm and 500 nm. Therefore, the importance of this spectral range will vary depending on the illumination of the scene and the scattering capacity of the water and the background. It should also be noted that the reflectance value of the dark background increases when the beaker is placed, indicating that reflections and refractions occur in the beaker, which increases the reflectance.

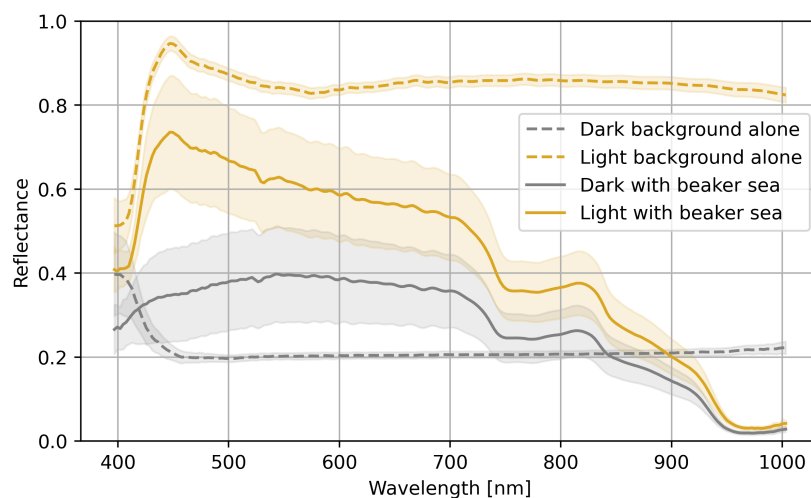


Figure 5. Mean spectral signature and standard deviation (shaded in the corresponding colour) of the backgrounds with and without the beaker.

3.2. Spectral Analysis—Rhodamine

We observed variations in spectral response to rhodamine concentrations at different wavelengths (Figure 6). We had four samples that combined distilled and seawater with light and dark backgrounds. In all samples, an increase in rhodamine concentration resulted in a shift of the reflectance peak around 600 nm towards longer wavelengths, giving the solution an increasingly orange hue. Initially, no differences were observed between distilled water and seawater samples, but noticeable differences emerged between light and dark backgrounds, especially at low rhodamine concentrations or when it was absent.

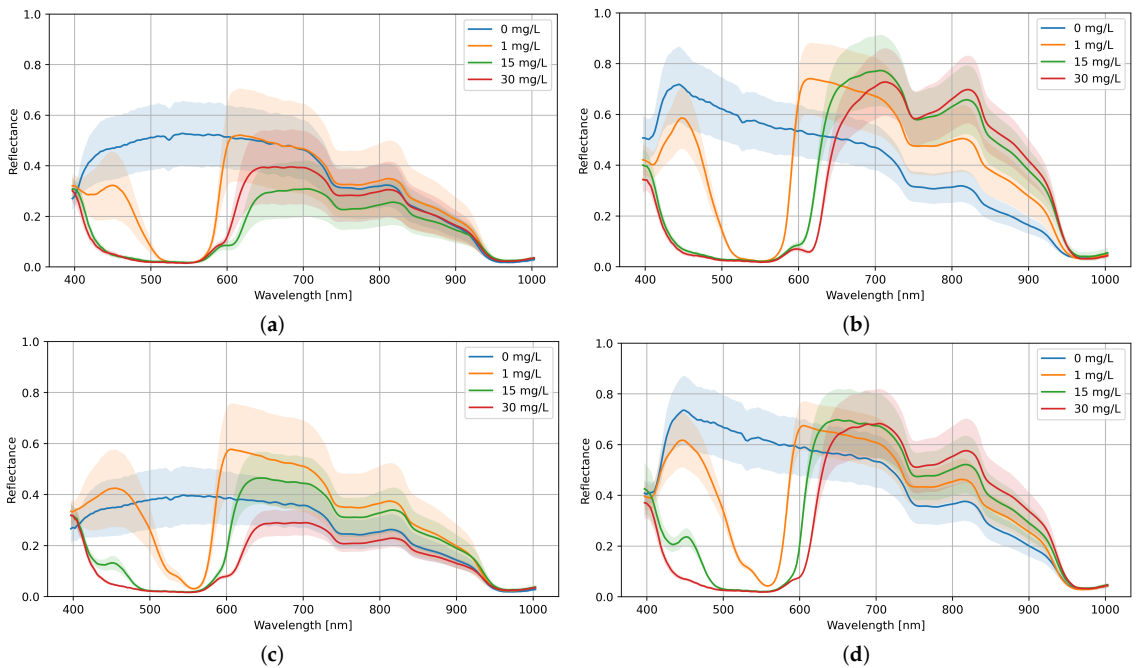


Figure 6. Mean spectra with standard deviation (shaded in the corresponding colour) for each concentration and sample. (a) Distilled water with a dark background; (b) distilled water with a light background; (c) sea water with a dark background; (d) sea water with a light background.

The most significant difference for both backgrounds was found at a concentration of 15 mg/L, specifically in the wavelength range of 600 nm to 650 nm (Figure 7). The samples exhibited a spectral difference of between 0.1 and 0.3 reflectance units; only the 15 mg/L sample with a light background with 0.37 reflectance units exceeded this value. The spectral differences between the two types of water were insufficient to conclusively distinguish between them.

More significant differences were observed when comparing the same water sample on the two different backgrounds, with discrepancies varying between 0.2 and 0.47 reflectance units. In Figure 8, a substantial decrease in reflectance is observed in the samples on a dark background, particularly pronounced in the red and near-infrared range (600 nm to 900 nm). The 15 mg/L and 30 mg/L samples show the most noticeable drops, reaching a difference between the spectral signatures of 0.47 and 0.41 for distilled water. Additionally, in the pure seawater samples, there is a reflectance peak associated with the blue colour, around 450 nm, on the light background that is not observed on the dark background, resulting in a difference in the spectral responses of 0.39.

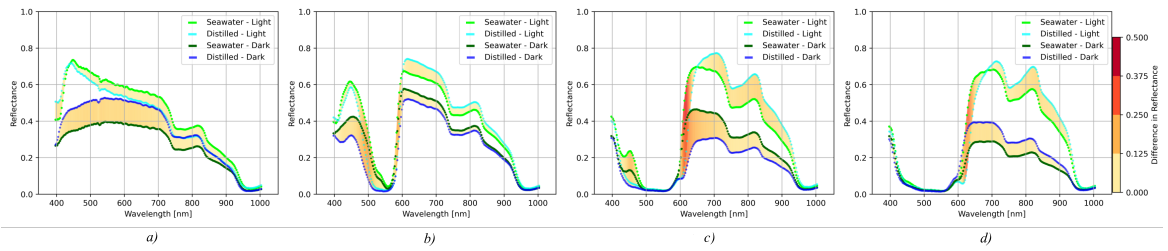


Figure 7. Spectral difference between distilled and seawater for the two backgrounds: (a) 0 mg/L; (b) 1 mg/L; (c) 15 mg/L; (d) 30 mg/L.

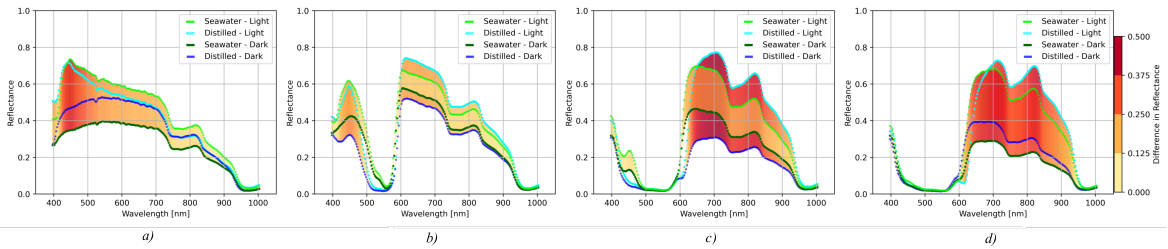


Figure 8. Spectral difference between backgrounds: (a) 0 mg/L; (b) 1 mg/L; (c) 15 mg/L; (d) 30 mg/L.

These findings highlight the influence of background type on the spectral signature of rhodamine and emphasize the need to consider background effects in remote sensing applications to improve rhodamine detection accuracy.

3.3. Classification

The first step is identifying the optimal number of bands for detecting rhodamine concentrations. As illustrated in Figure 9, OAC increases with the number of bands provided to each feature selector–classifier pair. The OAC achieved is above 80% with few bands across all samples, demonstrating the strong differentiating power of the classifiers. There is no apparent difference between the performance of distilled water and seawater. The models performed better with a light background than with a dark one, achieving greater accuracy faster. Additionally, it is evident that classifiers combined with the SFS feature selector yielded more satisfactory OAC. The optimal number of bands for detecting rhodamine using the elbow method [42] was two for all samples.

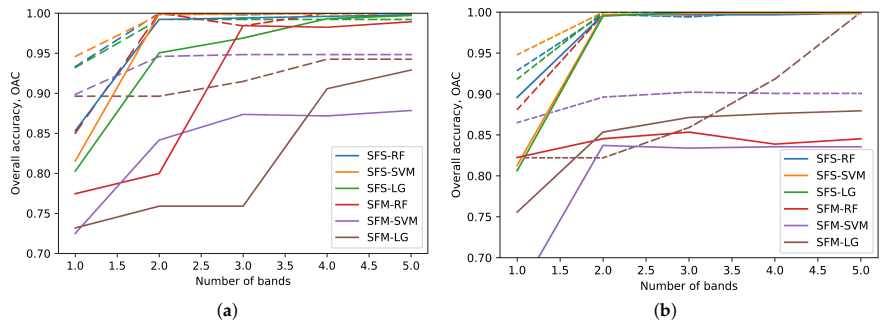


Figure 9. OAC of all model combinations for dark (solid line) and light (dashed line) backgrounds. (a) Distilled water; (b) seawater.

The SFS feature selector outperformed SFM, and both RF and SVM classifiers demonstrated excellent performance as Table 2 shows. For the light background, perfect performance was achieved in the three metrics, indicating a correct classification of all pixels in the validation subset. These results were to be expected, as the four classes are well differentiated and the number of pixels is limited.

Table 2. Metrics for all models with two bands of interest. The best result for each sample is marked in bold.

		SFS			SFM		
		OAC	F1	κ	OAC	F1	κ
Distilled water Dark background	RF	0.992	0.992	0.989	0.800	0.797	0.716
	LR	0.950	0.950	0.930	0.759	0.721	0.652
	SVM	0.999	0.999	0.999	0.842	0.799	0.773
Distilled water Light background	RF	1.000	1.000	1.000	1.000	1.000	1.000
	LR	0.992	0.992	0.989	0.896	0.863	0.850
	SVM	0.998	0.998	0.997	0.946	0.941	0.923
Seawater Dark background	RF	0.997	0.997	0.995	0.845	0.844	0.785
	LR	0.995	0.995	0.993	0.853	0.854	0.798
	SVM	0.997	0.997	0.995	0.837	0.838	0.775
Seawater Light background	RF	0.997	0.997	0.996	0.997	0.997	0.996
	LR	1.000	1.000	1.000	0.822	0.764	0.748
	SVM	1.000	1.000	1.000	0.896	0.880	0.856

We identified the optimal bands for each model (Figure 10). Two spectral areas of interest are highlighted, ranging from 400 nm to 500 nm and from 550 nm to 650 nm. These findings align with the regions of interest identified in the spectral analysis of different rhodamine concentrations. Samples with light backgrounds show more bands of interest in the blue region of the spectrum, whereas those taken on dark backgrounds tend to have significant bands in the yellow-orange region.

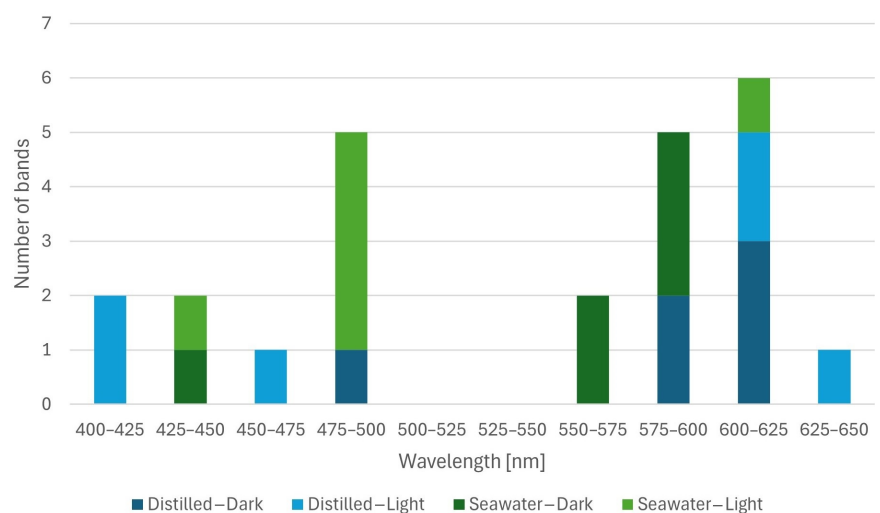


Figure 10. Spectral areas of interest, identified by grouping the two most significant bands for each combination of SFS with RF, LR, and SVM.

The background affects the spectral signature of the rhodamine and the band selection. However, transferring the trained artificial intelligence model from one scenario to another with a different background may be possible.

3.4. Transferability

We differentiated a section for the transfer of the bands of interest (Section 3.4.1) and another for the transfer of the pre-trained models (Section 3.4.2). In addition, a third section (Section 3.4.3) was included, where we improved the model transfer by combining all the samples and calculating the first derivative to train the classifier.

3.4.1. Band Transfer

The two most influential bands obtained with each model and sample were transferred to the rest of the samples to analyze the effectiveness of transferring spectral bands between different samples in the dataset. Section 3.3 shows that combining SFS with different classifiers led to the best results. Therefore, for this experiment, we exclusively analyzed the results of the SFS-RF combination. The other classifier combinations yielded similar results without a significant impact on the transferability of the bands and required more computational time.

The band transfer was successful for all samples as shown in Figure 11. The best results were obtained when validating the models with seawater samples, with superior performance observed when transferring from models trained with dark background samples. For distilled water samples, better performance was achieved when transferring bands from models trained also with distilled water samples.

		Dataset to validate			
		Distilled Dark	Distilled Light	Seawater Dark	Seawater Light
Dataset to train the model	Distilled - Dark	98	99	100	100
	Distilled - Light	94	100	95	98
	Seawater - Dark	88	83	100	100
	Seawater - Light	99	98	97	100

Figure 11. Accuracy obtained by transferring bands of interest from one sample to another. The colours indicate performance: green tones for accuracies above 80%, yellowish for 60–80%, orange for 40–60%, and red for accuracy below 40%.

3.4.2. Train Model Transfer

Transferring pre-trained classification models is complex due to the limited variability in the training samples of the dataset, which can easily lead to overfitting and lack of generalization. The accuracy results obtained differ significantly from those seen in band transfer. As shown in Figure 12, the model trained on distilled water with a dark background is not transferable to other samples, achieving an accuracy between 32% and 37%. However, the model trained on distilled water with a light background transfers perfectly to seawater with a light background, with an accuracy of 95%. This model also achieved 68% accuracy when transferred to seawater with a dark background. The model trained on seawater with a light background shows 97% accuracy when validated on distilled water with a light background and 86% accuracy when validated on seawater with a dark background. Meanwhile, the model trained on seawater with a dark background achieved 70% accuracy on both distilled water samples but fell below 50% on seawater with a light background.

The average accuracy, considering all transferred models, was 70%. Models show higher accuracy when transferring within the same background type, achieving 76% average accuracy for dark background samples and 98% accuracy for light ones. In contrast,

models trained on dark backgrounds achieved only 47% accuracy when applied to light background samples, and those trained on light backgrounds achieved 57% accuracy when transferred to dark background samples. This indicates that model transfer is performed effectively with the same background but different water types. Additionally, better results are obtained with light backgrounds compared to dark backgrounds, whereas performance decreases with different backgrounds.

		Dataset to validate			
		Distilled Dark	Distilled Light	Seawater Dark	Seawater Light
Dataset to train the model	Distilled - Dark	98	37	32	33
	Distilled - Light	37	100	68	95
	Seawater - Dark	72	70	100	46
	Seawater - Light	36	97	86	100

Figure 12. Accuracy obtained by transferring trained classifiers from one sample to another. The colours indicate performance: green tones for accuracies above 80%, yellowish for 60–80%, orange for 40–60%, and red for accuracy below 40%.

3.4.3. Improving Model Transfer Combining the Samples and Applying the First Derivative

Two approaches improve the model transfer. The first involves creating a new dataset that combines all types of samples with different water types and backgrounds, thereby avoiding overfitting the classifier. Secondly, the first derivative highlights variations in spectral signatures, enhancing the identification of concentrations. These new datasets will be referred to as combined sample (CS) and combined derivative (CD), respectively.

Analyzing the average spectral signature of CS (Figure 13), we can already anticipate that distinguishing between the 15 mg/L and 30 mg/L samples will be challenging because their spectral signatures are very similar. This similarity occurs because darker backgrounds attenuate light reflection, causing the reflectance of the 30 mg/L sample on a dark background to resemble the reflectance of the 15 mg/L sample on a light background. In the average spectrum of the first derivative, 15 mg/L and 30 mg/L are the closest concentrations, whereas the signature of the 1 mg/L concentration is well differentiated. The bands of interest are 580 nm and 610 nm for the combined samples and 591 nm and 607 nm for their first derivative.

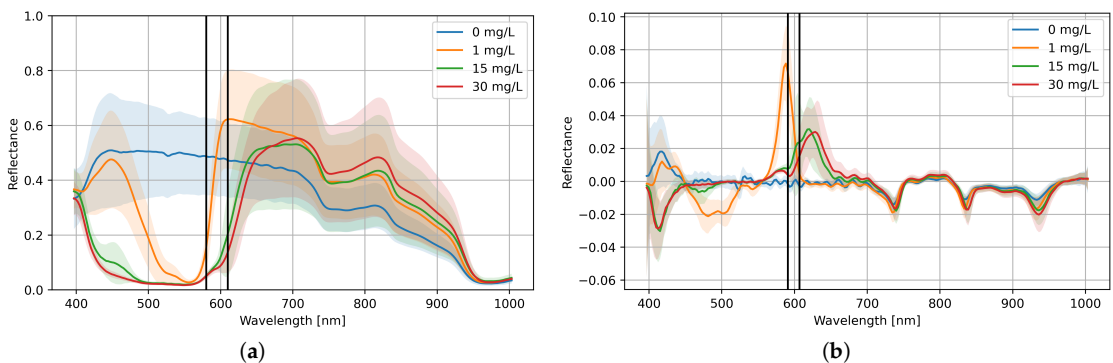


Figure 13. Mean spectra and standard deviation (shaded in the corresponding colour). The two best bands are indicated with black vertical lines. (a) Combined samples (580 and 610 nm); (b) the first derivative of the combined samples (591 and 607 nm).

The transfer of models trained with CS shows higher accuracy than the results presented in earlier sections. When applying the first derivative, the results are excellent, surpassing 85% accuracy in all cases except for the distilled samples with a light background, which only reaches 50%.

The confusion matrices for the best and worst cases provide additional insight into how the CS and the derivative influence classification (Figure 14). When training with CS and validating with light background samples, there is significant misclassification between the 15 mg/L and 30 mg/L, especially for distilled water. The separation of these two concentrations improves notably when the derivative (CD) is applied.

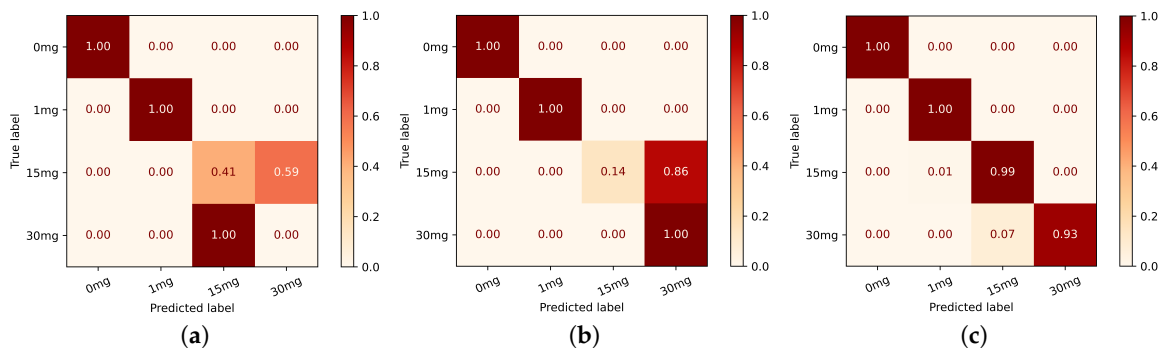


Figure 14. Confusion matrix training with CS and CD for the best and worst scenarios in Figure 15. (a) CS validating on distilled light; (b) CS validating on seawater light; (c) CD validating on seawater light.

This experiment again demonstrates that the background affects the reflectance of translucent solution spectral signatures. However, training a model with varied samples enhances classification performance, and using the first derivative aids in better identifying rhodamine concentrations.

		Dataset to validate			
		Distilled Dark	Distilled Light	Seawater Dark	Seawater Light
Dataset to train the model	Combined samples	88	50	69	75
	Combined - Derivative	86	56	89	97

Figure 15. Accuracy obtained by transferring trained classifiers from the combined sample. The colours indicate performance: green tones for accuracies above 80%, yellowish for 60–80%, orange for 40–60%, and red for accuracy below 40%.

4. Discussion

Significant differences were observed in the spectral response of samples with light and dark backgrounds in Section 3.2, with discrepancies of nearly 0.5 reflectance units. Small differences were observed based on the water type, but they are not sufficiently representative (between 0.1 and 0.3) to determine their influence. A curve around 810 nm appeared in all samples, consistent with studies [12,22], likely due to a local minimum in liquid water absorption common in shallow waters. The spectral regions most affected by rhodamine concentration were between 550 nm and 650 nm and from 400 nm to 500 nm, independently of the sample. These results aligned with the findings of Clark et al. [11], who observed that upwelling spectral radiance from a water body containing dye decreases in the green portion of the visible spectrum (530–570 nm) due to dye absorption and increases in the red and near-infrared wavelengths (570–750 nm) due to dye reflectance.

It should be noted that the influence of the 400 to 500 nm range is affected by the scene's illumination and the scattering properties of the water and the background. In our case study, this range is particularly impacted by the high reflectance caused by the reflections from the beaker.

The use of classifiers demonstrated high accuracy in differentiating rhodamine concentrations and determining that the optimal number of bands for the classification is two (Section 3.3). Classifiers combined with the SFS feature selector yielded more satisfactory results than SFM, with all classification metrics exceeding 90%. Several samples even achieved 100% accuracy, indicating that all pixels in the validation subset were correctly classified. These results were expected, as the dataset consists of controlled samples measured in a laboratory setting, with a limited number of pixels. This dataset will be extended to include more variability in future work, leading to more realistic classification metrics.

The study identified that for all the samples, the two most influential spectral bands were consistently within the 400–500 nm and 550–650 nm regions, corresponding to the regions identified in the spectral analysis of Section 3.2. We combined the bands identified by the best models (SFS + RF, LR, and SVM) to obtain enough data to determine if any patterns emerged in the bands of interest. A notable difference was observed between samples with light and dark backgrounds regardless of water type. Specifically, the 400–500 nm wavelengths are more relevant on light backgrounds, while the 550–650 nm range is more influential on dark backgrounds. This is a direct consequence of the background's influence and the rhodamine's semi-transparency, which is more critical on dark backgrounds due to lower reflection.

Transferring the results is a crucial phase of the study, as one of the primary objectives is to estimate the rhodamine concentration without specific scene calibration (Section 3.4). The successful transfer of bands of interest determined from one sample to another demonstrated that band transfer is feasible. The transfer of pre-trained models has been highly effective among light background samples, achieving an accuracy exceeding 95%. Nevertheless, the transfer of models between samples with different background types was not as effective, which was expected, given the difference in spectral areas of interest between light and dark backgrounds analyzed in Section 3.3. Also, the spectral range between 600 nm and 650 nm was both an area of interest for the classifiers and a region of significant discrepancy between the spectral signatures of distilled and seawater as shown in Section 3.2. This discrepancy further complicated the transfer between water types.

To overcome the impediments in model transfer caused by background reflectance differences and spectral signature variations due to water type, two essential measures were implemented: training the classifier with samples from different backgrounds and water types, and calculating the first derivative. When applying this approach, accuracy surpassed 85% in all cases except for the distilled light sample (50%). The optimal bands were between 580 and 610 nm. The primary difficulty improved by the first derivative was the differentiation between the 15 mg/L and 30 mg/L concentrations, as the reflectance of the 30 mg/L samples on dark backgrounds decreased, making it resemble the 15 mg/L samples on light backgrounds. This approach in Section 3.4.3 prevented overfitting in the classifier and highlighted variations in the spectral trends, improving the generalizability of the models.

This new proposed methodology can achieve a generalizable model that overcomes the limitations of current models. Clark et al. [11] show that band ratio linearity with rhodamine concentration becomes nonlinear above 0.03 mg/L, a problem that our method overcomes. Additionally, the Optimum Band Ratio Analysis (OBRA) [20], the most widely used method for determining rhodamine concentration, still requires on-site calibration for each specific scenario. Furthermore, the identified spectral areas of interest (400–500 nm and 550–650 nm) and the transfer of models had direct applications in the design and optimization of multispectral cameras [21]. These findings can be integrated into existing camera systems to enhance the detection and quantification of dye concentrations, which is crucial for applications such as tracking pollutant dispersion in water bodies.

Another approach to consider is radiative transfer models (RTMs), such as Hydro-light [43], which simulate light propagation through water and provide insights into environmental factors like depth, bottom types, and constituent concentrations. These models can be useful for predicting the behavior of substances like rhodamine in various aquatic environments, but they rely on precise input parameters that may not fully capture real-world complexity [44]. While complementary to laboratory measurements, which offer controlled and empirical data, RTMs may struggle with the complexity of optically shallow environments, where factors like bottom reflectance and water column effects introduce significant variability [2]. Given these challenges, we chose to rely on laboratory measurements combined with artificial intelligence models in our study. This approach allowed us to more effectively manage the inherent variability and complexity of optically shallow environments, providing a more robust and generalizable method for detecting and analyzing rhodamine in such settings.

Our study presents an exhaustive spectral analysis of different water types and backgrounds to improve the identification of various rhodamine concentrations. The key findings reveal significant spectral discrepancies based on the background type, highlighting the importance of considering background reflectivity in optically shallow waters. The transfer of bands of interest was successful, ensuring that multispectral cameras with a few bands can effectively determine rhodamine concentration. Additionally, training the classification model with combined samples and applying the first derivative enabled the successful transfer of pre-trained classification models. This advancement aimed to develop a classifier that works in several scenarios without the need for on-site calibration, bringing us one step closer to improving the remote detection of dye in aquatic environments.

Future research should focus on further refining the classification models by incorporating more diverse sample types and environmental conditions. Additionally, there is an interest in testing the implementation of a regressor to estimate rhodamine concentration and conducting experiments with lower concentrations in real-world scenarios. Exploring advanced machine learning techniques and integrating them with hyperspectral imaging can provide deeper insights and better transference. Expanding the spectral analysis to include other fluorescent dyes and pollutants can broaden the applicability of this research. Moreover, the development of real-time monitoring systems using these enhanced models could significantly benefit environmental monitoring, pollution control, and water quality assessment.

5. Conclusions

This study provided new insights into the generalization of spectral semi-transparent solutions detection across different water types and backgrounds. The spectral analysis identified relevant regions for rhodamine classification between 400 nm and 500 nm, and 550 nm and 600 nm, related to solution concentration. These wavelengths are commonly found in sensors and satellites such as Landsat 8 [45], Sentinel-2 [46], and WorldView-2 [47]. The significant differences observed between samples on dark and light backgrounds, especially with maximum reflectance captured, underscore the necessity of the spectral characterization of backgrounds when using rhodamine in optically shallow waters.

The classification results are promising, indicating the feasibility of transferring classification results with high accuracy, especially when integrated with the SFS feature selector. Our study identified the two most influential spectral bands consistently within the 400–500 nm and 550–650 nm regions for all samples, correlating with regions identified in the spectral analysis. While the transfer of spectral bands was successful (>80%), the transfer of trained models was only successful among light background samples. To improve these results, a model was trained by combining all samples to avoid overfitting, and applying the first derivative to enhance the identification of variations in the spectral signature. As a result, accuracy surpassed 85% in all cases except for the distilled light sample, where the concentrations of 15mg/L and 30mg/L were misclassified.

Therefore, the transfer of pre-trained classifiers between different backgrounds is feasible. This would potentially eliminate the need for on-site calibration each time rhodamine dispersion is studied in aquatic environments, saving materials and providing a generalizable classifier. Future research will focus on extending the dataset to include more variability and backgrounds, exploring the practical applicability of the models in outdoor scenarios. This expansion will ensure that the model can accurately generalize across diverse aquatic environments. By doing so, we can advance towards establishing standardized protocols for remote sensing and monitoring solutions dispersion, facilitating broader applications in environmental monitoring and water dynamics.

Author Contributions: Conceptualization, Á.P.-G., T.H.M.v.E. and J.F.L.; methodology, Á.P.-G. and A.M.L.; software, Á.P.-G. and A.M.L.; validation, A.R.-M. and E.H.; formal analysis, Á.P.-G. and A.M.L.; investigation, Á.P.-G. and A.M.L.; resources, E.H. and J.F.L.; data curation, A.R.-M. and A.M.L.; writing—original draft preparation, Á.P.-G. and A.M.L.; writing—review and editing, A.R.-M. and E.H.; visualization, Á.P.-G. and A.M.L.; supervision, T.H.M.v.E. and J.F.L.; project administration, J.F.L.; funding acquisition, J.F.L. All authors have read and agreed to the published version of the manuscript.

Funding: This work was completed while Ámbar Pérez-García was beneficiary of a predoctoral grant (ID: TESIS2021010059) given by the “Agencia Canaria de Investigación, Innovación y Sociedad de la Información (ACIISI)” of the “Consejería de Universidades, Ciencia e Innovación y Cultura”, part-financed by the European Social Fund Plus (FSE+) “Programa Operativo Integrado de Canarias 2021–2027, Eje 3 Tema Prioritario 74 (85%)”. Adrián Rodríguez-Molina and Emma Hernández have benefited from a predoctoral grant given by the “Vicerrectorado de Investigación y Transferencia de la Universidad de las Palmas de Gran Canaria” during the research. We would also like to thank the OASIS-HARMONIE project, under contract PID2023-148285OB-C43 from “Proyectos de Generación de Conocimiento” 2023, and the PERSEO project, under contract CPP2021-008527, from “Programa de Colaboración Público-Privada” of “Gobierno de España”, 2023–2025.

Data Availability Statement: The dataset used in this study is publicly available on IEEE Dataport. It can be accessed using the following DOI: 10.21227/n788-te91.

Acknowledgments: We would like to thank Elittoral for the preparation and provision of the rhodamine samples in different concentrations used in this study. We would also like to thank Guillermo Valentín Socorro Marrero for his valuable advice.

Conflicts of Interest: The authors declare no conflicts of interest. The funders had no role in the design of the study; in the collection, analyses, or interpretation of data; in the writing of the manuscript; or in the decision to publish the results.

References

1. Powers, C.; Hanlon, R.; Schmale, D.G., III. Tracking of a fluorescent dye in a freshwater lake with an unmanned surface vehicle and an unmanned aircraft system. *Remote Sens.* **2018**, *10*, 81. [[CrossRef](#)]
2. Ji, C.; Beegle-Krause, C.J.; Englehardt, J.D. Formation, detection, and modeling of submerged oil: A review. *J. Mar. Sci. Eng.* **2020**, *8*, 642. [[CrossRef](#)]
3. Okubo, A. Oceanic diffusion diagrams. In *Deep Sea Research and Oceanographic Abstracts*; Elsevier: Amsterdam, The Netherlands, 1971; Volume 18, pp. 789–802.
4. Pritchard, D.W.; Carpenter, J. Measurements of turbulent diffusion in estuarine and inshore waters. *Hydrol. Sci. J.* **1960**, *5*, 37–50. [[CrossRef](#)]
5. Fong, D.A.; Stacey, M.T. Horizontal dispersion of a near-bed coastal plume. *J. Fluid Mech.* **2003**, *489*, 239–267. [[CrossRef](#)]
6. González-Pinzón, R.; Haggerty, R.; Dentz, M. Scaling and predicting solute transport processes in streams. *Water Resour. Res.* **2013**, *49*, 4071–4088. [[CrossRef](#)]
7. Csanady, G. Turbulent diffusion in lake huron. *J. Fluid Mech.* **1963**, *17*, 360–384. [[CrossRef](#)]
8. Atkinson, T.; Davis, P. Longitudinal dispersion in natural channels: I. Experimental results from the River Severn, UK. *Hydrol. Earth Syst. Sci.* **2000**, *4*, 345–353. [[CrossRef](#)]
9. Drummond, J.; Davies-Colley, R.; Stott, R.; Sukias, J.; Nagels, J.; Sharp, A.; Packman, A. Retention and remobilization dynamics of fine particles and microorganisms in pastoral streams. *Water Res.* **2014**, *66*, 459–472. [[CrossRef](#)]
10. Legleiter, C.J.; McDonald, R.R.; Nelson, J.M.; Kinzel, P.J.; Perroy, R.L.; Baek, D.; Seo, I.W. Remote sensing of tracer dye concentrations to support dispersion studies in river channels. *J. Ecohydraulics* **2019**, *4*, 131–146. [[CrossRef](#)]

11. Clark, D.B.; Lenain, L.; Feddersen, F.; Boss, E.; Guza, R. Aerial imaging of fluorescent dye in the near shore. *J. Atmos. Ocean. Technol.* **2014**, *31*, 1410–1421. [CrossRef]
12. Köppl, C.J.; McKnight, U.S.; Lemaire, G.G.; Nørregaard, A.M.; Thiim, T.C.; Bjerg, P.L.; Bauer-Gottwein, P.; García, M. Tracer concentration mapping in a stream with hyperspectral images from unoccupied aerial systems. *Adv. Water Resour.* **2023**, *182*, 104567. [CrossRef]
13. Valerio, C.; Llebaria, A. A quantitative multispectral analysis system for aerial photographs applied to coastal planning. *Int. J. Remote Sens.* **1982**, *3*, 181–197. [CrossRef]
14. Spitzer, D.; Wernand, M. Multispectral remote-sensing of fluorescent tracers-theory and experiments. *Oceanol. Acta* **1983**, *6*, 201–210.
15. Hally-Rosendahl, K.; Feddersen, F.; Clark, D.B.; Guza, R. Surfzone to inner-shelf exchange estimated from dye tracer balances. *J. Geophys. Res. Oceans* **2015**, *120*, 6289–6308. [CrossRef]
16. Filippi, M.; Hanlon, R.; Rypina, I.I.; Hodges, B.A.; Peacock, T.; Schmale, D.G., III. Tracking a surrogate hazardous agent (rhodamine dye) in a coastal ocean environment using in situ measurements and concentration estimates derived from drone images. *Remote Sens.* **2021**, *13*, 4415. [CrossRef]
17. Nekouee, N.; Roberts, P.J.; Schwab, D.J.; McCormick, M.J. Classification of buoyant river plumes from large aspect ratio channels. *J. Hydraul. Eng.* **2013**, *139*, 296–309. [CrossRef]
18. Baek, D.; Seo, I.W.; Kim, J.S.; Nelson, J.M. UAV-based measurements of spatio-temporal concentration distributions of fluorescent tracers in open channel flows. *Adv. Water Resour.* **2019**, *127*, 76–88. [CrossRef]
19. Johansen, K.; Dunne, A.F.; Tu, Y.H.; Almashharawi, S.; Jones, B.H.; McCabe, M.F. Dye tracing and concentration mapping in coastal waters using unmanned aerial vehicles. *Sci. Rep.* **2022**, *12*, 1141. [CrossRef]
20. Legleiter, C.J.; Manley, P.V.; Erwin, S.O.; Bulliner, E.A. An experimental evaluation of the feasibility of inferring concentrations of a visible tracer dye from remotely sensed data in turbid rivers. *Remote Sens.* **2019**, *12*, 57. [CrossRef]
21. Pérez-García, A.; Rodríguez-Molina, A.; Hernández, E.; Vera, L.; López, J.F. Development of Low-Cost Multi-Spectral Cameras for Precision Agriculture. In Proceedings of the IGARSS 2023—2023 IEEE International Geoscience and Remote Sensing Symposium, Pasadena, CA, USA, 16–21 July 2023; pp. 3466–3469. [CrossRef]
22. Legleiter, C.J.; Sansom, B.J.; Jacobson, R.B. Remote sensing of visible dye concentrations during a tracer experiment on a large, turbid river. *Water Resour. Res.* **2022**, *58*, e2021WR031396. [CrossRef]
23. Developers, N. NumPy Gradient Function. 2024. Available online: <https://numpy.org/doc/stable/reference/generated/numpy.gradient.html> (accessed on 26 June 2024).
24. Elittoral. 2024. Available online: <https://www.elittoral.es/> (accessed on 16 June 2024).
25. Scientific, T. ThermoFisher Scientific Official Website. 2024. Available online: <https://www.patheon.com/us/en/home.html> (accessed on 28 June 2024).
26. Labbox. Lab Supplies. Available online: <https://labbox.eu/> (accessed on 7 August 2024).
27. Morales, A.; Horstrand, P.; Guerra, R.; Leon, R.; Ortega, S.; Díaz, M.; Melián, J.M.; López, J.F.; Callico, G.M.; et al. Laboratory hyperspectral image acquisition system setup and validation. *Sensors* **2022**, *22*, 2159. [CrossRef] [PubMed]
28. Specim Spectral Imaging. FX Series Hyperspectral Cameras. Available online: <http://www.specim.fi/fx/> (accessed on 6 October 2019).
29. SphereOptics. Zenith Polymer Diffusers. Available online: <https://sphereoptics.de/en/product/zenith-polymer-diffusers/?c=79> (accessed on 6 October 2019).
30. Pérez-García, A.; Lorenzo, A.M.; López, J. Spectral Band Selection Methodology for Future Sensor Development. In Proceedings of the 2024 47th MIPRO ICT and Electronics Convention (MIPRO), Opatija, Croatia, 20–24 May 2024; pp. 152–156. [CrossRef]
31. Kramer, O.; Kramer, O. Scikit-learn. In *Machine Learning for Evolution Strategies*; Springer: Berlin/Heidelberg, Germany, 2016; pp. 45–53.
32. Ho, T.K. Random decision forests. In Proceedings of the 3rd International Conference on Document Analysis and Recognition, Montreal, QC, Canada, 14–16 August 1995; Volume 1, pp. 278–282. [CrossRef]
33. Wright, R.E. Logistic regression. *Circulation* **1995**, *117*, 18.
34. Hearst, M.; Dumais, S.; Osuna, E.; Platt, J.; Scholkopf, B. Support vector machines. *IEEE Intell. Syst. Their Appl.* **1998**, *13*, 18–28. [CrossRef]
35. Breiman, L. Random forests. *Mach. Learn.* **2001**, *45*, 5–32. [CrossRef]
36. Hosmer, D.W., Jr.; Lemeshow, S.; Sturdivant, R.X. *Applied Logistic Regression*; John Wiley & Sons: Hoboken, NJ, USA, 2013; Volume 398.
37. Suthaharan, S.; Suthaharan, S. Support vector machine. In *Machine Learning Models and Algorithms for Big Data Classification: Thinking with Examples for Effective Learning*; Springer: Berlin/Heidelberg, Germany, 2016; pp. 207–235.
38. Hossin, M.; Sulaiman, M.N. A review on evaluation metrics for data classification evaluations. *Int. J. Data Min. Knowl. Manag. Process.* **2015**, *5*, 1.
39. Boughorbel, S.; Jarray, F.; El-Anbari, M. Optimal classifier for imbalanced data using Matthews Correlation Coefficient metric. *PLoS ONE* **2017**, *12*, e0177678. [CrossRef]
40. Cohen, J. A coefficient of agreement for nominal scales. *Educ. Psychol. Meas.* **1960**, *20*, 37–46. [CrossRef]
41. Sammut, C.; Webb, G.I. *Encyclopedia of Machine Learning*; Springer Science & Business Media: Berlin/Heidelberg, Germany, 2011.
42. Syakur, M.; Khotimah, B.; Rochman, E.; Satoto, B.D. Integration k-means clustering method and elbow method for identification of the best customer profile cluster. In *IOP Conference Series: Materials Science and Engineering*; IOP Publishing: Bristol, UK, 2018; Volume 336, p. 012017.
43. Moble, C.D.; Sundman, L.K. *HydroLight 5 Ecolight 5*; Sequoia Scientific Inc.: Bellevue, WA, USA, 2008; Volume 16.

44. Salesin, K.; Knobelspiesse, K.D.; Chowdhary, J.; Zhai, P.W.; Jarosz, W. Unifying radiative transfer models in computer graphics and remote sensing, Part I: A survey. *J. Quant. Spectrosc. Radiat. Transf.* **2024**, *314*, 108847. [[CrossRef](#)]
45. Morfitt, R.; Barsi, J.; Levy, R.; Markham, B.; Micijevic, E.; Ong, L.; Scaramuzza, P.; Vanderwerff, K. Landsat-8 Operational Land Imager (OLI) radiometric performance on-orbit. *Remote Sens.* **2015**, *7*, 2208–2237. [[CrossRef](#)]
46. Pahlevan, N.; Sarkar, S.; Franz, B.; Balasubramanian, S.; He, J. Sentinel-2 MultiSpectral Instrument (MSI) data processing for aquatic science applications: Demonstrations and validations. *Remote Sens. Environ.* **2017**, *201*, 47–56. [[CrossRef](#)]
47. Corporation, S.I. WorldView-2 Satellite Sensor. 2024. Available online: <https://earth.esa.int/eogateway/missions/worldview-2> (accessed on 7 August 2024).

Disclaimer/Publisher's Note: The statements, opinions and data contained in all publications are solely those of the individual author(s) and contributor(s) and not of MDPI and/or the editor(s). MDPI and/or the editor(s) disclaim responsibility for any injury to people or property resulting from any ideas, methods, instructions or products referred to in the content.

Chapter 4

Unsupervised Hyperspectral Methods for Scalable Monitoring

A significant challenge limiting HSI's large-scale application is the need for vast amounts of labelled data to train supervised algorithms effectively. Obtaining labelled data in aquatic environments is challenging due to field deployment requirements, high personnel and equipment costs, and logistical constraints. This lack of labelled data creates a bottleneck, restricting the scalability and generalization of current models and hindering their adoption for broader monitoring applications.

Sub-objective 3 of this thesis aims to improve HSI processing through a new loss function for unsupervised neural networks. Developing unsupervised methods capable of classifying images without large labelled datasets has become crucial in overcoming large-scale environmental monitoring. Unsupervised neural networks offer a promising approach. They identify patterns and classify objects based solely on the data's spectral characteristics, eliminating the need for ground truth, which is often unavailable open ocean and other aquatic environments. However, these methods are still in the early stages and require optimization to reach the performance levels of supervised models.

In Section 4.1: "Novel Spectral Loss Function for Unsupervised Hyperspectral Image Segmentation," the spectral loss function (Sl) is introduced, a novel approach to enhance unsupervised neural networks. This loss function enables the algorithm to learn how to differentiate between spectral signatures of pixels, allowing it to compare them and determine whether they belong to the same class. Sl improved the performance of the best current unsupervised segmentation neural network. The proposed approach outperforms spectral indices, which rely on a few spectral bands and expert-set thresholds, by using an unsupervised neural network that classifies based on the full spectral response, enabling direct differentiation of surfaces and transferability across environments. Unsupervised techniques also help generate ground-truth data without significant investment in human or material resources, making these models a more viable solution for large-scale monitoring.

4.1 Novel Spectral Loss Function for Unsupervised Hyperspectral Image Segmentation

- **Á. Pérez-García**, M. E. Paoletti, J. M. Haut and J. F. López, “Novel Spectral Loss Function for Unsupervised Hyperspectral Image Segmentation,” *IEEE Geoscience and Remote Sensing Letters*, vol. 20, pp. 1-5, 2023, Art no. 5506505.
- DOI: [10.1109/LGRS.2023.3288809](https://doi.org/10.1109/LGRS.2023.3288809)
- Paper is published in ”IEEE Geoscience and Remote Sensing Letters”.
- Publisher: IEEE.
- Print ISSN: 1545-598X (Electronic ISSN: 1558-0571).
- Journal metrics:
 - 2022 Journal Impact Factor: 4.0.
 - Journal Citation Indicator (JCI): 1.08.
 - Rank by Journal Impact Factor:
 - * **Q1**: Geochemistry & Geophysics.
 - * **Q2**: Engineering, Electrical & Electronic; Remote Sensing; Imaging Science & Photographic Technology.

Novel Spectral Loss Function for Unsupervised Hyperspectral Image Segmentation

Ámbar Pérez-García^{1b}, Mercedes E. Paoletti^{1b}, *Senior Member, IEEE*,
Juan M. Haut^{1b}, *Senior Member, IEEE*, and José F. López^{1b}

Abstract—Neural networks (NNs) have gained importance in hyperspectral image (HSI) segmentation for earth observation (EO) due to their unparalleled data-driven feature extraction capability. However, in many real-life situations, ground truth is not available, and the performance of unsupervised NNs is still susceptible to enhancement. To overcome this challenge, this letter presents a new loss function to improve the performance of unsupervised HSI segmentation models. The spectral loss function, *SL*, which can be included in different models, is based on the purity of the unmixing endmembers and the spectral similarity of the clusters provided by the NN to determine the classes. It is incorporated into a 3-D convolutional autoencoder (AE) to validate its performance on four standard HSI benchmarks. Furthermore, its performance has been qualitatively examined in a real case study, an oil spill without ground truth. The results show that *SL* is a breakthrough in unsupervised HS segmentation, obtaining the best overall performance and highlighting the importance of spectral signatures. Additionally, the dimensional reduction is also vital in compacting the spectral information, which facilitates its segmentation. The source code is available at <https://github.com/mhaut/HSI-3DSpLoss>.

Index Terms—Autoencoder (AE), hyperspectral images (HSIs), semantic segmentation, unsupervised learning.

I. INTRODUCTION

HYPERSPECTRAL imaging (HSI) contributes to many fields regarding Earth observation (EO), such as precision agriculture, risk prevention, environmental studies, and natural resources management. Depending on the atomic structure of the surface, solar radiation is reflected differently at each wavelength. Thus, a distinct spectral signature is

Manuscript received 20 March 2023; revised 13 June 2023; accepted 20 June 2023. Date of publication 22 June 2023; date of current version 5 July 2023. This work has been funded by the PTOLOMEO project (Platform for Thermal and Optical Low-altitude Marine Environment autonomous Observations) financed by the “Cabildo de Gran Canaria” and FDCAN (Fondo de Desarrollo de Canarias). It also was partially funded by the European Regional Development Fund (ERDF/FEDER) and by “Junta de Extremadura” under grant GR21040 and the project Ref. IB20040. The Spanish Government have also funded this work as part of the APOGEO project (Precision Agriculture for the Improvement of Viticulture in Macaronesia, grant number MAC/1.1.b/226), Interreg Program (MAC 2014-2020), and the TALENTHExPERIA project, under contract PID2020-116417RB-C42. This work was completed while Ámbar Pérez-García was beneficiary of a predoctoral grant given by the “Agencia Canaria de Investigación, Innovación y Sociedad de la Información (ACIISI)” of the “Consejería de Economía, Conocimiento y Empleo,” part-financed by the European Social Fund (FSE). (*Corresponding author: Ámbar Pérez-García.*)

Ámbar Pérez-García and José F. López are with the Institute for Applied Microelectronics, University of Las Palmas de Gran Canaria, 35001 Las Palmas, Spain (e-mail: ambar.perez@ulpgc.es).

Mercedes E. Paoletti and Juan M. Haut are with the Hyperspectral Computing Laboratory, Department of Technology of Computers and Communications, Escuela Politécnica, University of Extremadura, 10003 Cáceres, Spain (e-mail: juanmariohaut@unex.es).

Digital Object Identifier 10.1109/LGRS.2023.3288809

obtained for each material depending on its physical and chemical characteristics and its roughness. Collected scenes are organized in large 3-D cubes, where each pixel is an N -dimensional vector (spectral signature) of N -bands [1]. Thus, processing this rich spectral information provides valuable knowledge of the observed materials. Due to strong intraclass and low interclass spectral variability, HSI classification has remained difficult [2].

Spectral unmixing, classification, and segmentation are popular HSI processing methods. Unmixing methods analyze the pixel content considering it as a mixture of pure spectral signatures (endmembers) and decomposing its signature into a set of endmembers and their corresponding abundances. Classifiers assign a label from a group of land cover categories to every pixel in the scene, while segmentation models divide the scene into multiple regions or segments, providing the boundaries of existing objects. Traditionally, these methods were based on the spectral features of the scene. Nevertheless, in EO, it is usual to observe large areas of homogeneous land cover. Consequently, it is possible to presume that surrounding regions of a pixel are constituted of the same materials and exhibit similar spectral behavior. Furthermore, remote-sensing (RS) data are geolocated, and each pixel corresponds to a spatial coordinate. As a result, information from spatially adjacent pixels improves the accuracy of methods, removing uncertainties caused by spectral variability [3].

Regarding the learning strategy, these methods can be mainly performed in a supervised or unsupervised manner [4], where the former needs substantial and properly annotated datasets to effectively analyze HSIs, especially for data-hungry techniques like neural networks (NNs) [5]. Ground-truth generation requires expert knowledge, is time-consuming, inefficient, and costly and is limited or unavailable in real scenarios. Some strategies deal with the lack of labeled data, such as data augmenting, transfer learning, and semisupervised analysis. Nevertheless, a modest collection of labeled data is needed to conduct all of them, which makes them unfeasible in the absence of labeled data. Thus, HSI analysis significantly benefits from the use of unsupervised approaches, as they do not require reference data nor prior knowledge, employing specific measures to assess the segmentation quality [6].

In general, the core of the design of unsupervised methods depends on the metrics or distances used to compare the generated and the desired data, and a correct design of the loss function is critical. RS scientists have used the feature extraction ability of deep learning (DL) to automatically discover hidden patterns in images to meet the demands of

new EO applications and research [7]. Recently, convolutional NNs (CNNs) [8], fully convolutional networks (FCNs) [9], and autoencoders (AEs) [10] have significantly increased unsupervised semantic segmentation efficiency compared to previous approaches [11].

The lack of more accurate unsupervised classification and segmentation methods has motivated this work, where a new loss function is proposed to address the problems of no ground-truth HSI sets. Based on unmixing basics, the proposed spectral loss function, Sl , analyzes the spectral homogeneity of the NN output clusters. The contributions of this work are the following.

- 1) A novel loss function that employs spectral signatures to characterize surfaces and facilitate their segmentation.
- 2) The best-performing unsupervised model for HSI segmentation.

The unsupervised HSI segmentation procedure is enhanced by exploiting feature representation through DL architectures and by the proposed loss function that heightens spectral characteristics. Segmentation analysis is conducted over four different HSI benchmark datasets, that is, Pavia University (PU), Salinas Valley (SV), Indian Pines (IP), and University of Houston (UH2018), and a real use case using an AVIRIS image. For comparative purposes, the 3D convolutional autoencoder (3D-CAE) architecture for end-to-end unsupervised HSI segmentation [6] is considered as the baseline, and its performance is improved by incorporating the proposed spectral loss function in the decoder phase.

II. METHOD

The pixel spectral signature in the HSI is one of the keys to classifying them into different land cover categories. Each substance is known to have a pure spectral signature, the so-called endmembers in unmixing. A pixel can gather information from a variety of sources. Thus, it is acknowledged as a collection of pure signatures that may be decomposed into its endmembers. This served as the foundation of the proposed spectral loss function design. The NN provides a distribution of pixels into clusters of similar spectral properties. Each output neuron of the network will determine which pixels belong to one of the clusters. The spectral loss function measures the spectral homogeneity of the clusters provided by the NN. For this purpose, the average spectral signature of each cluster is calculated and compared with each pixel of the corresponding cluster. If the clusters are well defined, the average spectral signature of each cluster should be comparable to the signatures of its pixels. Ideally, the average signatures would be identical to the individual pixel signatures. Theoretically, this process can be differentiable to calculate the loss gradient relative to the source, that is, the model weights.

Regarding the spectral loss function, its two input parameters are the HSI scene to be segmented, $\mathbf{H} \in \mathbb{R}^{R \times C \times B}$, where R is the number of rows in the image, C is the number of columns, and B is the number of spectral bands, and the NN output weights, $\vec{z} \in \mathbb{R}^{R \times C \times K}$, where K is the number of neurons in the last layer, which determines the number of classes. It is recommended that both the HSI and the NN output be restructured in the format $R \cdot C \times B$ and $R \cdot C \times K$

accordingly to operate efficiently. Hence, \mathbf{H} may be seen as a collection of hyperspectral pixels, with p_i denoting the i th pixel and N the total number of pixels ($N = R \cdot C$). Similarly, the NN output provides the weights of each neuron for each pixel. In the mathematical formulations, the subscript j indicates the operation performed for each output neuron, $j = 1, 2, \dots, K$. First, the following equation presents the softmax function:

$$\sigma_i(\vec{z}) = \frac{e^{z_i}}{\sum_{j=1}^K e^{z_j}} \quad (1)$$

with $i = 1, 2, \dots, N$. The softmax function is applied to the NN output weights. It converts each pixel NN output into a normalized class membership probability vector, formally expressed by the following equation:

$$\forall p_i \in \mathbf{H} : \sum_{j=1}^K P_j(p_i) = 1 \quad (2)$$

where P_j is the probability of belonging to class j . The vector shall be of dimension K , equal to the number of classes of the multiclass classifier. This shows the likelihood that a particular pixel belongs to each neuron, that is, class membership. Thus, it is straightforward to know the class with the highest membership probability. The composition of class vectors of all the pixels is the class probability matrix, \mathbf{Mc} . Each row of the \mathbf{Mc} corresponds to the probability of a pixel belonging to each class.

The weighted mean spectral signature, $\mathbf{Ws} \in \mathbb{R}^{K \times B}$, is obtained by multiplying the class probability matrix by the image, as shown follows indicates:

$$\mathbf{Ws} = \mathbf{Mc}^T \cdot \mathbf{H} \quad (3)$$

where each $w_{i,j}$ is the mean average of band i weighted with the probability of pixels belonging to a class j . Thus, each row in \mathbf{Ws} contains the weighted mean spectral signature of a particular output neuron.

The total of the probabilities associated with each neuron is required to determine the class centroids. Each column of \mathbf{Mc} represents the probability of each pixel belonging to a given class, P_j . The total probability regarding a class is obtained by summing over all column elements of \mathbf{Mc} , that is, summing over all the pixels. The centroids of each cluster are then calculated in the following equation through an element-wise division of the weighted average spectral signature, $w_{i,j}$, by the sum of the probabilities of belonging to each cluster, P_j :

$$c_{i,j} = \frac{w_{i,j}}{\sum_{i=1}^N P_j(p_i)} \quad (4)$$

Elements $c_{i,j}$ form the centroid matrix, $\mathbf{C} \in \mathbb{R}^{K \times B}$. Each row contains the spectral signature of a centroid.

The original image is reconstructed in (5) from the centroids and the probability of belonging to each cluster. Each element of the reconstructed image, $\hat{\mathbf{H}} \in \mathbb{R}^{N \times B}$, represents a pixel obtained by weighting the centroids of each class with the

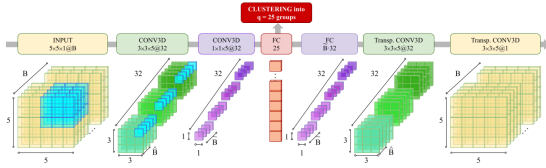


Fig. 1. Graphical representation of the 3-D-CAE model for HSI segmentation.

probability of belonging to that class

$$\begin{aligned} \hat{H} &= Mc \cdot C \\ &= \begin{pmatrix} P_1(p_1) & \dots & P_K(p_1) \\ \vdots & \ddots & \vdots \\ P_1(p_N) & \dots & P_K(p_N) \end{pmatrix} \cdot \begin{pmatrix} C_{1,1} & \dots & C_{1,B} \\ \vdots & \ddots & \vdots \\ C_{K,1} & \dots & C_{K,B} \end{pmatrix}. \end{aligned} \quad (5)$$

Finally, the spectral loss, Sl , is computed as follows:

$$Sl = \sum_{i=1}^N |p_i(B) - \hat{p}_i(B)| \quad (6)$$

where p_i is the original pixel and \hat{p}_i is the reconstructed pixel.

A. Three-Dimensional Convolutional AE

A network with a 3D-CAE architecture is used as a baseline (Fig. 1). This model has proven to be the best-performing in the unsupervised HSI segmentation method [6]. The network encoding phase captures spectral and spatial features inside an input 3-D patch of size $5 \times 5 \times B$ by comprising two 3-D convolution layers with unit stride, which extract the embedded features. Then, an input to a fully connected (FC) layer, that is, embedding layer, is created by reshaping the patch central-pixel features into a 1-D vector. Previous work has shown that 3-D-CAE is stable and robust against the number of neurons of the FC layer. The NN produces the best results when it possesses between 20 and 30 neurons; therefore, 25 neurons are considered. Furthermore, it matches the size of the reference model, ensuring a fair and valid comparison of cluster performance. This first stage uses the original reconstruction loss and runs until reaching convergence or the stopping condition (25 epochs). In the decoding phase of the CAE, the embedded features are converted back to the original 3-D patch. This second phase integrates the spectral loss function to reconstruct the clusters. The opposite steps are conducted as in the encoder, with the transposed convolutions. Thus, a segmented image with the original dimensions ($R \times C \times 1$) is obtained.

III. EXPERIMENTS

The improvement of incorporating the proposed spectral loss function (Section III-A) is evaluated by comparing the modified 3-D-CAE with state-of-the-art methods (Section III-B) and studying its effectiveness in a real case study (Section III-C). Experimental parameters of [12] are replicated using the same datasets and suggested models for comparative purposes. The objective is to improve the performance of the best-unsupervised segmentation AE using the spectral loss function, Sl , for HSI data. The experiments are

conducted on four popular HSI datasets: **PU**, acquired in Italy (340×610 pixels, ROSIS, nine classes, 103 bands, 1.3 m); **SV**, gathered in USA (217×512 pixels, AVIRIS sensor, 16 classes, 224 bands, 3.7 m); **IP**, also collected in USA (145×145 pixels, AVIRIS sensor, 16 classes, 200 bands, 20 m), and **UH2018**, USA (4172×1202 pixels, ITRES CASI 1500, 20 classes, 48 bands, 1 m).

Two clustering-quality measures evaluate the results and quantify the performance of the unsupervised techniques. On the one hand, the normalized mutual information (NMI) [13] is a normalization of the mutual information (MI) that gives a measure of the correlation between the clusters. On the other hand, the adjusted rand index (ARI) computes a similarity measure between two clusters. It is the corrected-for-chance version of the rand index (RI) [14]. The range of values that the NMI and ARI may take is 0 to 1, with 1 being a perfect score. Both metrics are unaffected by a permutation of a class or cluster label values since these measures are independent of the labels' absolute values. NMI and ARI calculations do not include unknown pixels.

Experiments have been run on a hardware platform with an Intel i9-12900KS processor with 128 GB of DDR4 RAM and NVidia 4090RTX with 24 GB of RAM. The source code of the framework was implemented with the Keras library.

A. Improvement of the Loss Function

The first experiment compares the performance of the original 3-D-CAE network with the proposed network. Both run under identical conditions. The algorithms are tested on the full image and over spectrally reduced versions to see the performance. Principal component analysis (PCA), independent component analysis (ICA), and multispectral simulation from HSI (S-MSI) are employed for HSI reduction. For every case, the feature dimensionality is reduced to 25, which corresponds to the quantity of embedded 3-D-CAE features.

Table I indicates that the spectral loss function improves the NN performance. The best result for each case, full image or reduced versions for the two models, is marked in bold. The best dataset result, that is, for each column, is outlined in green. In PU, performance has not improved, probably because it is the simplest dataset and, therefore, less influenced by spectral differentiation. In general, it is worth noting that when using dimensional reduction with PCA, the acquired segmented image results in higher quality. The idea is that segmenting an HSI becomes more problematic when the model receives information from the entire spectrum due to the high spectral variability and redundancies. Dimensional reduction algorithms compact the spectral data, making spectral differences between classes more noticeable.

B. Comparisons With Other Methods

Additionally, another experiment compares the proposed method with other techniques, such as k -means, where k is the number of classes in the dataset. Gaussian mixture modeling (GMM) is an extension of k -means that integrates knowledge of the data's covariance structure and the centers of latent Gaussians. A variational AE (VAE) is also explored with 2 FC

TABLE I

AVERAGE RESULTS AFTER FIVE RUNS OF ALL THE METRICS OF THE ORIGINAL AND THE PROPOSED MODEL

Algorithm	PU		SV		IP		UH2018	
	NMI	ARI	NMI	ARI	NMI	ARI	NMI	ARI
3D-CAE	0.553	0.339	0.714	0.533	0.431	0.231	0.277	0.047
Proposed	0.563	0.360	0.773	0.589	0.460	0.265	0.279	0.080
3D-CAE+PCA	0.639	0.546	0.746	0.527	0.467	0.263	0.260	0.038
Proposed+PCA	0.580	0.428	0.855	0.672	0.517	0.283	0.294	0.067
3D-CAE+ICA	0.538	0.316	0.839	0.644	0.504	0.278	0.293	0.064
Proposed+ICA	0.552	0.377	0.855	0.669	0.514	0.279	0.288	0.065
3D-CAE+S-MSI	0.601	0.450	0.728	0.531	0.442	0.241	0.268	0.045
Proposed+S-MSI	0.554	0.412	0.778	0.590	0.458	0.270	0.270	0.083

in encoding (512 and 25 activations) and decoding (512 and $25 \cdot B$ activations) parts. VAE is trained with 5×5 patches over ten epochs.

Lastly, it is compared with three recurrent NNs (RNNs), which act as asymmetric AEs. The simple recurrent unit (SRU), the long short-term memory RNNs (LSTM), and the recurrent gated units (GRUs). Unsupervised results derived from a supervised 1-D-CNN model are presented (using the ADAM optimizer with a learning rate of 10^{-4} , $\beta_1 = 0.9$, and $\beta_2 = 0.999$) for better comprehension. Network training implements Monte-Carlo cross-validation with balanced training and validation sets. The training, validation, and test sets consist respectively of 80%, 10%, and 10% of the pixels of each class selected randomly and without overlapping. The presented NMI and ARI values have been calculated only on labeled pixels. The proposed method is abbreviated as CAE-SL to simplify terminology. All models have been applied to both the full HSI and the various scaled-down versions of it. After determining that the number of components in the PCA has no significant effect on 3-D-CAE performance, it has been set to 25 for all models, allowing a fair comparison.

Table II provides the experimental results obtained over all sets. The first row, referring to the supervised trained 1-D-CNN, is presented as a benchmark framework, and the best model performance for each dataset is underlined in Table II. The metrics corroborate that the spectral loss function provides the best segmentation results. CAE-SL obtains the best performance for the IP dataset and the best NMI for PU and SV. GRU comes second, with the highest ARI in the PU, SV, and UH2018 datasets. For UH2018, GMM holds the best NMI value, and LSTM ties GRU in ARI. Two interesting facts about the results are worth noting. First, the idea that dimensional reduction favors segmentation is reinforced, with the PCA technique standing out among the three studied. Second, SV leads the metrics ranking. In this dataset, the methods have generally performed well, and the CAE-SL proposal rivals the result of the supervised method. Moreover, Table III shows how the complexity of the proposed model is significantly lower than that of other models, with only 409 K parameters. In light of the above, it can be concluded that SL provides a nonnegligible advantage when segmenting HSIs.

To summarize, the results of experiments in Sections III-A and III-B place our model as the best-performing, highlighting the importance of the spectral loss function, *Sl*. Considering pixels as combinations of pure spectral signatures and the influence of the spectral similarity of the clusters helps improve the HSI segmentation algorithm's performance. The last experiment explores a real scenario without labeled data.

TABLE II

UNSUPERVISED SEGMENTATION MEASURES OVER ALL BENCHMARKS

Algorithm	PU		SV		IP		UH2018	
	NMI	ARI	NMI	ARI	NMI	ARI	NMI	ARI
1D-CNN*	<u>0.786</u>	<u>0.771</u>	<u>0.885</u>	<u>0.725</u>	0.705	0.586	<u>0.586</u>	<u>0.569</u>
PCA	0.360	0.215	0.860	0.685	0.640	0.493	0.417	0.354
ICA	0.616	0.556	0.873	0.723	0.641	0.502	0.484	0.441
S-MSI	0.784	0.759	0.880	0.723	0.718	0.609	0.563	0.546
k-means	0.546	0.350	0.752	0.538	0.437	0.211	0.252	0.043
PCA	0.545	0.324	0.724	0.524	0.430	0.204	0.251	0.043
ICA	0.477	0.263	0.730	0.535	0.381	0.178	0.247	0.035
S-MSI	0.546	0.325	0.712	0.496	0.430	0.208	0.256	0.043
GMM	0.514	0.290	0.819	0.642	0.445	0.229	0.343	0.088
PCA	0.530	0.404	0.830	0.654	0.443	0.235	0.349	0.099
ICA	0.522	0.396	0.838	0.665	0.436	0.212	0.054	0.000
S-MSI	0.532	0.407	0.848	0.673	0.456	0.248	0.336	0.081
VAE	0.505	0.286	0.703	0.554	0.396	0.247	0.269	0.068
PCA	0.423	0.297	0.648	0.496	0.202	0.131	0.301	0.101
ICA	0.297	0.120	0.694	0.540	0.260	0.161	0.273	0.086
S-MSI	0.394	0.234	0.722	0.584	0.429	0.275	0.262	0.065
SRU	0.503	0.393	0.647	0.510	0.386	0.251	0.270	0.058
PCA	0.407	0.245	0.733	0.561	0.436	0.241	0.240	0.042
ICA	0.427	0.268	0.736	0.562	0.433	0.246	0.259	0.056
S-MSI	0.516	0.450	0.732	0.583	0.431	0.240	0.276	0.057
LSTM	0.564	0.463	0.717	0.547	0.406	0.248	0.279	0.051
PCA	0.499	0.295	0.802	0.630	0.478	0.253	0.345	0.098
ICA	0.549	0.446	0.830	0.654	0.467	0.243	0.334	0.103
S-MSI	0.569	0.463	0.710	0.570	0.434	0.265	0.292	0.054
GRU	0.509	0.466	0.677	0.526	0.414	0.274	0.290	0.062
PCA	0.523	0.312	0.825	0.626	0.515	0.276	0.348	0.103
ICA	0.524	0.280	0.818	0.675	0.467	0.243	0.342	0.097
S-MSI	0.518	0.483	0.721	0.570	0.414	0.236	0.313	0.070
CAE-SL	0.563	0.360	0.773	0.589	0.460	0.265	0.279	0.080
PCA	0.580	0.428	0.855	0.672	0.517	0.283	0.294	0.067
ICA	0.552	0.377	0.855	0.669	0.514	0.279	0.288	0.065
S-MSI	0.554	0.412	0.778	0.590	0.458	0.270	0.270	0.083

TABLE III

COMPARISON IN TERMS OF PARAMETERS (MODELS USED IN [6])

Model	Parameters	Model	Parameters
1D-CNN [6]	10,105K	LSTM [6]	1,325K
GRU [6]	1,324K	3D-CAE [6]	409K
SRU	1,322K	Proposed	409K

C. Real Use Case: Oil Spill

Oil spills are a good case study for unsupervised methods as obtaining a ground truth of the phenomenon is challenging because it is often far offshore, currents displace and dilute it, and it is dangerous to collect samples [15]. In this experiment, the best segmentation method is applied on a real HSI scene, of which no ground truth is available. The Airborne Visible Infrared Imaging Spectrometer (AVIRIS) captured the study image on 17 May 2010 in the Gulf of Mexico. The sensor detects 224 contiguous bands at 10-nm intervals across a wavelength range from 366 to 2496 nm (VNIR and SWIR). The study image is a fragment of the **f100517t01p00r11** HSI scene, which is freely available in [16]. The scene shows part of an oil spill caused by the Deepwater Horizon drilling rig.

In Fig. 2(a), the oil can be seen with the naked eye in the RGB composition. The image shows different levels of oil spill thickness. The bright lines across the bottom half of the figure are emulsions. There are also true color oil stains, seen as dark reddish rounded spots in the upper part of the image. Emulsions and continuous true-color oil slicks are considered thick spills since their thickness exceeds $200 \mu\text{m}$. Medium-thickness spills, also called discontinuous true color oil slicks, are yellowish in the RGB and have thicknesses between 50 and $200 \mu\text{m}$. Finally, the rest of the scene is covered by a thin film of oil called sheens. Lastly, sheens are thin oil films that cover the rest of the scene. These are less than $50\text{-}\mu\text{m}$ -thick and are not visible in the RGB.

Fig. 2(b) shows the normalized difference oil index (NDOI) [17]. This spectral index detects oil spills and

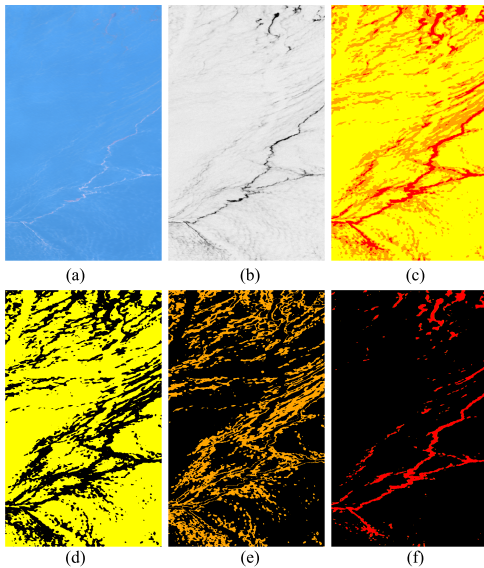


Fig. 2. Image f100517t01p00r11 by AVIRIS on 17 May 2010. (a) RGB. (b) NDOI. (c) Spill map. (d) Thin spill. (e) Medium spill. (f) Thick spill.

distinguishes their thickness. In NDOI, the areas of thicker spillage are highlighted darker. Qualitatively, it can be seen how the network classification map [Fig. 2(c)] separates the spillage by thickness. The Thick Spill class highlights the emulsion lines running through the scene and the dark spots in the upper corner. The Medium Spill class has the same grainy appearance as the discontinuous spots. The Thin Spill class indicates the sheens. As a result, the map is reasonably accurate compared to the RGB and NDOI sceneries. In addition, NNs outperformed spectral indexes in segmenting HSI by learning their complex spectral and spatial features.

IV. CONCLUSION

In this letter, a new spectral loss function is presented. It utilizes spectral information for HSI segmentation employing unsupervised 3-D-CAE. To validate the effectiveness of our approach, experiments on PU, SV, IP, and University of Houston datasets have been conducted, as well as an AVIRIS image used as a real case study. According to the numerical and visual evidence, the suggested technique's findings point to a valuable improvement in the performance of HSI semantic segmentation utilizing the spectral loss function, SI . Incorporating SI into the 3-D-CAE model yields the best-performing unsupervised model for HSI segmentation. The real use case consolidates SI as a loss function for unsupervised HSI segmentation, as it reproduces the spill detection spectral index NDOI behavior. Results underline the significance of considering pixels as blends of pure spectral signatures, the impact of the clusters' spectral similarity, and the importance of dimensional reduction. Continuing to improve unsupervised methods is of utmost importance in RS and EO. The amount of unlabeled data is overwhelming

and unsupervised techniques help to generate ground-truth data without the need to invest a lot of time and resources, both human and material. The proposed framework can be further improved in future work by strengthening dimensional reduction techniques. We want to test different dimensionality reduction methods and make combinations and modifications of those already tested. Enhancing this aspect of the framework will not only reduce computational time but will also boost performance.

REFERENCES

- [1] J. L. García, M. E. Paoletti, L. I. Jiménez, J. M. Haut, and A. Plaza, "Efficient semantic segmentation of hyperspectral images using adaptable rectangular convolution," *IEEE Geosci. Remote Sens. Lett.*, vol. 19, pp. 1–5, 2022.
- [2] P. Duan, P. Ghamisi, X. Kang, B. Rasti, S. Li, and R. Gloaguen, "Fusion of dual spatial information for hyperspectral image classification," *IEEE Trans. Geosci. Remote Sens.*, vol. 59, no. 9, pp. 7726–7738, Sep. 2021.
- [3] J. Liu, Z. Xiao, Y. Chen, and J. Yang, "Spatial-spectral graph regularized kernel sparse representation for hyperspectral image classification," *ISPRS Int. J. Geo-Inf.*, vol. 6, no. 8, p. 258, Aug. 2017.
- [4] M. E. Paoletti, J. M. Haut, J. Plaza, and A. Plaza, "Deep learning classifiers for hyperspectral imaging: A review," *ISPRS J. Photogramm. Remote Sens.*, vol. 158, pp. 279–317, Dec. 2019. [Online]. Available: <https://www.sciencedirect.com/science/article/pii/S0924271619302187>
- [5] D. Fitton, E. Laurens, N. Hongkarnjanakul, C. Schwob, and L. Mezeix, "Land cover classification through convolutional neural-net model assembly: A case study of a local rural area in Thailand," *Remote Sens. Appl., Soc. Environ.*, vol. 26, Apr. 2022, Art. no. 100740.
- [6] J. Nalepa, M. Myller, Y. Imai, K. Honda, T. Takeda, and M. Antoniuk, "Unsupervised segmentation of hyperspectral images using 3-D convolutional autoencoders," *IEEE Geosci. Remote Sens. Lett.*, vol. 17, no. 11, pp. 1948–1952, Nov. 2020.
- [7] L. Mou, P. Ghamisi, and X. X. Zhu, "Unsupervised spectral-spatial feature learning via deep residual conv-deconv network for hyperspectral image classification," *IEEE Trans. Geosci. Remote Sens.*, vol. 56, no. 1, pp. 391–406, Jan. 2018.
- [8] Y. Duan, F. Luo, M. Fu, Y. Niu, and X. Gong, "Classification via structure-preserved hypergraph convolution network for hyperspectral image," *IEEE Trans. Geosci. Remote Sens.*, vol. 61, 2023, Art. no. 5507113.
- [9] L. Wang, R. Li, C. Duan, C. Zhang, X. Meng, and S. Fang, "A novel transformer based semantic segmentation scheme for fine-resolution remote sensing images," *IEEE Geosci. Remote Sens. Lett.*, vol. 19, pp. 1–5, 2022.
- [10] T. Guo, R. Wang, F. Luo, X. Gong, L. Zhang, and X. Gao, "Dual-view spectral and global spatial feature fusion network for hyperspectral image classification," *IEEE Trans. Geosci. Remote Sens.*, vol. 61, 2023, Art. no. 5512913.
- [11] X. X. Zhu et al., "Deep learning in remote sensing: A comprehensive review and list of resources," *IEEE Geosci. Remote Sens. Mag.*, vol. 5, no. 4, pp. 8–36, Dec. 2017.
- [12] L. Tulczyjew, M. Kawulok, and J. Nalepa, "Unsupervised feature learning using recurrent neural nets for segmenting hyperspectral images," *IEEE Geosci. Remote Sens. Lett.*, vol. 18, no. 12, pp. 2142–2146, Dec. 2021.
- [13] A. Collignon, F. Maes, D. Delaere, D. Vandermeulen, P. Suetens, and G. Marchal, "Automated multi-modality image registration based on information theory," *Inf. Process. Med. Imag.*, vol. 3, no. 6, pp. 263–274, 1995.
- [14] L. Hubert and P. Arabie, "Comparing partitions," *J. Classification*, vol. 2, no. 1, pp. 193–218, Dec. 1985.
- [15] P. Duan, X. Kang, P. Ghamisi, and S. Li, "Hyperspectral remote sensing benchmark database for oil spill detection with an isolation forest-guided unsupervised detector," *IEEE Trans. Geosci. Remote Sens.*, vol. 61, 2023, Art. no. 5509711.
- [16] NASA Jet Propulsion Laboratory. (2021). *Airborne Visible Infrared Imaging Spectrometer Website*. [Online]. Available: <https://aviris.jpl.nasa.gov/>
- [17] Á. Pérez-García, P. Horstrand, and J. F. López, "Ndoi, a novel oil spectral index: Comparisons and results," in *Proc. 12th Workshop Hyperspectral Imag. Signal Process., Evol. Remote Sens. (WHISPERS)*, Sep. 2022, pp. 1–5.

Chapter 5

Conclusions

This thesis presents a suite of transferable HSI methodologies for environmental pollution monitoring in aquatic environments. To achieve this, several HSI challenges, such as hyperspectral data complexity, the need for efficient dimensionality reduction, and the scarcity of labelled datasets for training supervised models, had to be overcome [93–96]. Each chapter offers a unique strategy for improving HSI-based aquatic pollutant detection. Chapter 2 introduces a quick-calculating spectral index for rapid decisions. Chapter 3 optimizes dimensionality reduction for broader adaptability to various environments through band and model transfer. Chapter 4 enhances unsupervised learning to address data scarcity. These approaches tackle specific gaps and improve transferability across diverse scenarios, advancing towards standardized HSI methods for environmental monitoring.

Chapter 2 proposes a new spectral index, the Normalized Difference Oil Index (NDOI), to improve coastal oil spill detection. NDOI fills a critical gap in the literature by providing a more general solution that discriminates between oil and sand in suspension under coastal conditions. Thanks to its simplified mathematical operation, which requires only two spectral bands, the NDOI offers a faster calculation than similar indices. This approach is precious when a rapid decision is needed, and computational resources are limited [101]. Additionally, the spectral bands used by NDOI are centred at 599 nm and 870 nm—wavelengths commonly available on multispectral sensors in scientific missions, for example, Landsat 8 [105]. Although spectral indices can reduce HSI complexity, they still face limitations, such as reliance on manual thresholding—sensitive to changing environmental conditions—and difficulty distinguishing between multiple object types using a single index [102]. Given these limitations and the advancement of AI methodologies, choosing a more sophisticated method is preferable when time and computing power allow [69].

Chapter 3 addresses hyperspectral data’s high dimensionality by introducing a band selection methodology that identifies the most relevant spectral bands for detecting target items, such as plastics or rhodamine. Combining selected spectral bands with a classifier offers richer information than a spectral index,

as it enables the identification of multiple classes and the assessment of the method's accuracy [99]. Other commonly used dimensionality reduction methods, such as Principal Component Analysis (PCA) [117, 118], do not yield specific spectral bands, making them less suitable for developing generalizable methods. This research demonstrated the effective transfer of spectral bands between hyperspectral datasets. However, further investigation is needed to apply this method to multispectral sensors, as their wider bandwidths lack the finer resolution of HSI [42]. Studies indicate that detecting and classifying pollutants with gradually changing spectral signatures may not require high spectral detail, suggesting that sensors with broader bands could still effectively classify some pollutants [91, 107]. Applying the first derivative has proven helpful in enhancing the transfer of pre-trained classification models, as it highlights subtle spectral features and improves class separability. Nevertheless, using the first derivative does not reduce dimensionality, as it depends on the entire spectra and is unsuitable for multispectral sensors, where the spectral signature is discontinuous [119]. The transfer of pre-trained models requires further refinement, highlighting the need for broader datasets and a deeper understanding of background reflections' influence isemitransparentnt objects and optically shallow waters spectra. To address this, emerging workflows that facilitate the acquisition of large, varied datasets for training and validation hold promise in improving model generalization and reliability [120].

Chapter 4 presents the spectral loss function (Sl) that enhances the performance of unsupervised neural networks. This loss function tackles one of the most critical challenges in HSI and AI-based environmental monitoring: the scarcity of labelled data [78]. Sl improves the performance of the currently best-performing unsupervised segmentation neural network [83] and outperforms spectral indices in detecting oil spills. DL models, especially deep convolutional neural networks, require more data than traditional ML algorithms due to the number of parameters they need to optimize [71]. Shallow ML models (such as SVM or RF) obtain a nice performance with less data, but they may struggle to capture the full complexity of HSI data [79, 80]. The new approach offers a significant advantage when labelled datasets are unavailable, as it can help automatically generate labelled data, reducing the reliance on expensive and time-consuming manual annotation [81]. Despite their advantages, unsupervised methods still lag behind supervised techniques in performance [110]. Nevertheless, supervised models require large datasets, which are difficult to obtain in hazardous areas such as the open ocean, where manual labelling is challenging and resource-intensive [70, 108]. Therefore, this research highlights the potential of unsupervised methods to improve monitoring systems' adaptability, especially in data-scarce environments.

Each chapter of the thesis confronts and addresses a specific aspect of current HSI knowledge gaps, contributing valuable advancements toward efficient and

transferable environmental monitoring solutions. Spectral indices, such as the NDOI, offer a simple and effective solution when rapid responses are needed with limited computational capacity. [101] They can be quickly calculated, making them ideal for decision-making in real-time applications. However, they require manual thresholding to identify classes, which can reduce precision [102]. In contrast, classification algorithms directly assign classes based on spectral signatures, eliminating the need for manual interpretation and improving detection accuracy in complex scenarios [78]. Band selection algorithms identify influential spectral bands that can be used to create more refined spectral indices and train classifiers that generalize better across different environments [99]. This last approach is promising for decreasing reliance on labelled data [89]. However, further research is needed to deepen our understanding of model transfer. Finally, unsupervised methods add a crucial dimension by generating labelled data where none exists, enabling quick predictions and serving as a foundation for training classifiers [81]. While they do not match the precision of supervised models, they offer significant potential for addressing data scarcity in remote monitoring scenarios [69]. Together, these methods create a cohesive framework that balances speed, accuracy, and transferability in hyperspectral image analysis.

In conclusion, this thesis has successfully developed novel techniques that enhance the detection and monitoring of aquatic pollutants using remote sensing hyperspectral images and artificial intelligence. After a thorough analysis of these techniques, a clear understanding of their strengths and weaknesses has been achieved, applying the most appropriate method based on the specific circumstances of each study. The outcomes of this research can help design next-generation sensors for UAVs and space missions, where data efficiency and precision are essential. Additionally, the techniques developed in this thesis have direct implications for environmental management, with potential applications in early spill detection, coordination of beach cleanup efforts, and support of new data-driven policies.

5.1 Future work

Future efforts should prioritize refining automatic techniques and advancing the transferability of artificial intelligence models. These are essential for achieving efficient, transferable and scalable environmental monitoring with minimal manual intervention and reduced computational demands. Building upon the promising methodologies introduced in this thesis, future research should focus on enhancing the adaptability and robustness of unsupervised models across environments. By addressing challenges related to model transfer—particularly for complex scenarios like optically shallow waters or

semitransparent pollutants—we can further streamline detection processes, reduce the need for in-situ validation, and support the rapid deployment of these tools in urgent environmental crises [109]. Optimizing post-processing techniques and integrating cloud-based processing frameworks could also enable large-scale data handling, making monitoring extensive geographic areas feasible [121, 122]. Through these advancements, we move closer to achieving a more automated and accessible environmental monitoring system, empowering data-driven decisions for the conservation and protection of ecosystems.

The future of AI-driven environmental monitoring will revolutionize efforts to address urgent issues such as oil spills and plastic pollution. By combining advanced remote sensing with automated detection, upcoming satellite missions—with reduced computational costs—could enable onboard processing for large-scale, near-real-time assessments [106]. Novel specialized sensors and reliable ground truth data will be crucial in refining these models, enhancing their accuracy across diverse environmental settings [120]. The band selection model and custom loss function developed here are highly transferable. They can be applied to other fields of Earth observation such as precision agriculture and mineralogy, but also to medical imaging and other fields where data volume reduction is needed. The following subsections outline several key initiatives I aim to pursue shortly.

Band transferability across multispectral and hyperspectral sensors

Future work will assess the transferability of the band selection methodology to multispectral sensors by comparing it across various commercial and experimental sensors with differing spectral resolutions. Hyperspectral sensors achieve higher spectral resolution than multispectral sensors by capturing narrow, contiguous spectral bands across the electromagnetic spectrum [42]. The finer resolution allows the detection of subtle variations in materials, while broader bands capture aggregated information across a wider range, offering less detailed spectral data [45]. This difference in spectral resolution is crucial in applications where rapid spectral signature changes occur, as multispectral sensors may miss these subtle variations.

Specifically, I plan to evaluate commercial multispectral sensors such as Silios [123] and MAIA [124], which have broad bandwidths, to understand how well the selected spectral bands perform under reduced spectral resolution. The Silios CMS-V1 captures the spectral range of 500 to 850 nm, offering bands with spectral resolutions between 25 and 34 nm [123]. MAIA-S2 aligns with the spectral bands of the multispectral instrument (MSI) aboard the Sentinel-2 satellite [104], covering 430 to 880 nm. MAIA includes bands at various resolutions: seven at 15–35 nm, one at 65 nm, and one at 115 nm [124]. In addition, I will examine the capabilities of novel experimental sensors such

as PANDORA [46], which offers a narrower 10 nm bandwidth comparable to hyperspectral sensors, often between 5 to 10 nm [125]. This comparison will show how well the band selection method generalizes across sensors with different spectral resolutions and will determine the feasibility of extending this methodology to multispectral systems.

Harnessing Cloud Computing for Scalable Environmental Data Processing

Cloud computing is increasingly transforming Earth observation by enhancing satellite image processing and analysis efficiency and scalability, especially when integrated with AI algorithms [126]. Unlike local computing, cloud platforms such as Google Earth Engine (GEE) and Microsoft Planetary Computer offer immense computational power and eliminate the need to store vast amounts of satellite imagery locally [127, 128]. These platforms provide access to extensive image collections directly on the cloud, facilitating time series analysis and enabling large-scale geographic studies. Thanks to servers' computational power, AI models are executed faster [129]. The ability to perform complex analyses remotely, without high demands on local infrastructure, makes cloud computing an ideal solution for managing and processing the immense data volumes involved in environmental monitoring [122].

Cloud computing offers a robust infrastructure to support and scale the techniques dealt with throughout the thesis. In cloud-based research, the publication **J.1** “Cloud-Based Analysis of Large-Scale Hyperspectral Imagery for Oil Spill Detection” implements a parallelized computation of the NDOI on cloud, reducing memory requirements while ensuring scalable processing for massive datasets [95]. Additionally, the conference abstract **C.4** “River Plastic Monitoring Workflow: From Satellite to Cloud Computing” marks the beginning of my ongoing research. Here, we propose a novel workflow for analyzing satellite images using cloud computing, specifically leveraging GEE and Python to extract critical spectral and spatial information efficiently. This approach optimizes computational time, enhancing the global identification of macroplastic hotspots. My work will continue to expand with additional study sites and a transferability evaluation across diverse locations and dates.

Appendix A

Resumen en Español

Esta tesis propone un conjunto de metodologías transferibles para la monitorización ambiental, centradas en la detección de contaminantes en ecosistemas acuáticos mediante el uso de teledetección con imágenes hiperespectrales (Hyperspectral Imaging, HSI) y técnicas de inteligencia artificial (IA). Estas metodologías facilitan la observación sistemática en grandes cantidades de datos, contribuyendo al desarrollo de soluciones estandarizadas para monitorizar y proteger los ecosistemas.

Este trabajo aborda las limitaciones actuales de la tecnología hiperespectral, tales como la alta dimensionalidad de los datos, la falta de técnicas eficaces de reducción dimensional y la escasez de conjuntos de datos etiquetados necesarios para entrenar los modelos de IA. En esta tesis se desarrollan y exponen métodos innovadores que mejoran la eficiencia, precisión y adaptabilidad de las técnicas de detección de contaminantes, como derrames de petróleo y residuos plásticos en ambientes acuáticos.

Entre los logros más destacados se encuentra el Índice de Diferencia Normalizada de Petróleo (Normalized Difference Oil Index, NDOI), un nuevo índice espectral que reduce la clasificación errónea de arena en suspensión, mejorando la detección de vertidos en zonas costeras. Se propone también un método de selección de bandas espectrales que optimiza la detección de contaminantes específicos, reduciendo la complejidad de las HSI y mejorando la capacidad de los modelos para generalizarse en distintos entornos acuáticos. Otro avance importante es la función de pérdida espectral (spectral loss function, Sl), que mejora la segmentación en redes neuronales no supervisadas.

La tesis finaliza con un análisis de las contribuciones realizadas, destacando los avances logrados en términos de eficiencia y transferibilidad de las tecnologías de monitorización ambiental. Estos métodos poseen un alto potencial para desarrollar la próxima generación de sensores, la gestión ambiental y la toma de decisiones en situaciones de crisis medioambiental. En futuras investigaciones, se plantea profundizar en la automatización de estas técnicas, mejorar la transferibilidad de los algoritmos y aprovechar herramientas como la computación en la nube para la observación a gran escala de la Tierra.

Objetivos

Esta tesis aborda algunos desafíos críticos de la teledetección hiperespectral en la monitorización ambiental, incluyendo la complejidad y volumen de datos, la limitada transferibilidad de los modelos a distintos entornos y la escasez de datos etiquetados, que dificultan el seguimiento sistemático a gran escala. Su objetivo principal es desarrollar un conjunto de metodologías transferibles para detectar contaminantes en ambientes acuáticos.

Para alcanzar este objetivo, se establecen varios subobjetivos específicos:

1. Presentar un nuevo índice espectral para mejorar la detección de derrames de petróleo, facilitando respuestas rápidas en situaciones de crisis ambiental.
2. Desarrollar una metodología de reducción de dimensionalidad que optimice las bandas espectrales para la monitorización de contaminantes acuáticos y mejore la transferibilidad de los resultados a diferentes entornos.
3. Proponer una nueva función de pérdida para redes neuronales no supervisadas que mejore el procesamiento de imágenes hiperespectrales.

La investigación sigue una progresión clara. Comienza con un análisis de los sensores disponibles y las misiones espaciales para monitorizar la contaminación con técnicas estándar como los índices espectrales. Avanza hacia enfoques más sofisticados para reducir la dimensionalidad, optimizando el procesamiento de datos y mejorando la adaptabilidad de los modelos de detección a diversos entornos. La etapa final amplía el alcance y aplicabilidad de los métodos mediante técnicas de detección no supervisada.

Conclusiones

Esta tesis presenta un conjunto de metodologías basadas en HSI transferibles para la monitorización de la contaminación ambiental en entornos acuáticos. La tesis aborda desafíos asociados a la complejidad de los datos hiperespectrales, la necesidad de una reducción eficiente de dimensionalidad, y la escasez de conjuntos de datos etiquetados para entrenar modelos supervisados [93–96].

Cada capítulo introduce una estrategia única para mejorar la detección de contaminantes acuáticos basada en HSI. El Capítulo 2 introduce el índice espectral NDOI, que permite detectar derrames de petróleo en costas de manera rápida y precisa. El Capítulo 3 propone una metodología de selección de bandas espectrales que optimiza la información para detectar contaminantes como plásticos, ampliando así la capacidad de adaptación de los modelos. En el

Capítulo 4, se presenta una nueva función de pérdida para redes neuronales no supervisadas, que ayuda a superar la falta de datos etiquetados.

El Capítulo 2 propone el NDOI, un índice espectral diseñado para mejorar la eficacia de la detección de petróleo en zonas costeras. El NDOI llena un vacío crítico en la literatura al discriminar eficazmente entre petróleo y arena en suspensión. Su cálculo es sencillo y solo requiere dos bandas espectrales, resultando valioso cuando se necesita una decisión ágil y los recursos computacionales son limitados [101]. Las bandas espectrales del NDOI, centradas en 599 nm y 870 nm, están disponibles en sensores multiespectrales como los de Landsat 8 [105]. Aunque los índices espectrales pueden reducir la complejidad de HSI, presentan limitaciones como la dependencia de un experto para definir umbrales manualmente, que pueden resultar sensibles a las condiciones ambientales, y la dificultad para diferenciar varios tipos de objetos con un solo índice [102]. Por ello, cuando el tiempo y el poder computacional lo permiten, es preferible optar por métodos más avanzados de IA [69].

El Capítulo 3 aborda la alta dimensionalidad de las HSI mediante una metodología de selección de bandas que identifica las bandas espectrales más relevantes para detectar elementos como plásticos o rodamina. La combinación de bandas influyentes con un clasificador proporciona más información que un índice espectral, permitiendo la identificación de múltiples clases y la evaluación de la precisión del método [99]. Métodos de reducción de dimensionalidad como el Análisis de Componentes Principales [117, 118] no seleccionan bandas específicas, lo cual limita su uso para desarrollar métodos generalizables. Esta investigación demostró la transferencia efectiva de bandas espectrales entre conjuntos de datos hiperespectrales. Sin embargo, se necesita una investigación más profunda sobre su aplicación a sensores multiespectrales, cuyas bandas más anchas no poseen la resolución fina de HSI [42]. Se ha comprobado que la primera derivada es útil para resaltar detalles espectrales sutiles y mejorar la separabilidad de las clases, aunque no reduce la dimensionalidad y depende del espectro completo, volviéndola inadecuada para desarrollar sensores multiespectrales [119]. La transferencia de modelos preentrenados requiere un refinamiento adicional, especialmente para objetos semitransparentes en aguas ópticamente complejas, lo que sugiere la necesidad de conjuntos de datos más amplios y una mejor comprensión de los efectos de fondo [120].

El Capítulo 4 presenta la función de pérdida espectral (SI), que mejora el rendimiento de redes neuronales no supervisadas, enfrentando la escasez de datos etiquetados en la monitorización ambiental basada en HSI e IA [78]. SI incrementa el rendimiento de la red no supervisada más eficaz en segmentación actual [83], superando el desempeño de los índices espectrales en la detección de derrames de petróleo. Los modelos de aprendizaje profundo, como las redes neuronales convolucionales, requieren un gran volumen de datos de entrenamiento debido a la cantidad de parámetros que optimizan [71]. Modelos

de aprendizaje automático convencionales (como Support Vector Machine o Random Forest) funcionan bien con menos datos, pero no captan la complejidad total de los datos HSI [79, 80]. Esta nueva metodología es especialmente relevante cuando no se dispone de conjuntos de datos etiquetados, pues permite generar etiquetas automáticamente, reduciendo la necesidad de anotaciones manuales [81]. Aunque los métodos no supervisados no igualan la precisión de los supervisados, ofrecen una oportunidad significativa para abordar la escasez de datos en la monitorización de zonas remotas y de difícil acceso [69].

Cada capítulo de la tesis aborda un aspecto específico de las lagunas de conocimiento en HSI, avando hacia soluciones más eficientes y transferibles para la monitorización ambiental. Los índices espectrales, como el NDOI, son soluciones simples y eficaces cuando se necesitan respuestas rápidas con recursos computacionales limitados [101], aunque requieren umbrales manuales que pueden reducir la precisión [102]. En cambio, los algoritmos de clasificación asignan clases basadas en firmas espectrales, eliminando la interpretación manual y mejorando la precisión en escenarios complejos [78]. Los algoritmos de selección de bandas identifican las bandas espectrales más influyentes, que pueden refinar el diseño de índices espectrales y entrenar clasificadores más generalizables [99]. Los métodos no supervisados pueden ayudar a generar datos etiquetados donde no están disponibles, permitiendo predicciones rápidas y sirviendo de base para el entrenamiento de clasificadores [81]. En conjunto, estos métodos crean un marco cohesionado que equilibra velocidad, precisión y transferibilidad en el análisis de imágenes hiperespectrales.

En conclusión, esta tesis desarrolla técnicas avanzadas para mejorar la detección y monitorización de contaminantes acuáticos mediante imágenes hiperespectrales e IA. Se ha obtenido una comprensión clara de sus fortalezas y debilidades, aplicando el método más adecuado según las circunstancias de cada estudio. Los resultados de esta investigación pueden facilitar el diseño de la próxima generación de sensores para drones (Uncrewed Aerial Vehicles, UAVs) y misiones espaciales, donde la eficiencia de los datos y precisión son esenciales. Además, las técnicas desarrolladas en esta tesis tienen implicaciones directas en la gestión ambiental, con aplicaciones potenciales en la detección temprana de derrames de petróleo, la coordinación de limpieza de playas, y el apoyo a nuevas políticas basadas en datos.

Los esfuerzos futuros deben centrarse en automatizar las técnicas y mejorar la transferibilidad de los modelos de inteligencia artificial. Los modelos generalizables, los sensores especializados y el procesamiento eficiente a bordo de satélites y drones va a revolucionar la monitorización ambiental en las próximas décadas. Finalmente, la computación en la nube es una herramienta novedosa que permite realizar análisis complejos de grandes volúmenes de datos de imágenes satelitales, facilitando estudios a gran escala y aumentando la eficiencia de procesamiento para aplicaciones de monitorización ambiental.

Bibliography

- [1] P. Kershaw and J. Protection, *Sources, fate and effects of microplastics in the marine environment: a global assessment*. UNESCO: United Nations Educational, Scientific and Cultural Organisation, 2015.
- [2] D.-P. Häder, A. T. Banaszak, V. E. Villafaña, M. A. Narvarte, R. A. González, and E. W. Helbling, “Anthropogenic pollution of aquatic ecosystems: Emerging problems with global implications,” *Science of The Total Environment*, vol. 713, p. 136586, 2020.
- [3] J. R. Jambeck, R. Geyer, C. Wilcox, T. R. Siegler, M. Perryman, A. Andrady, R. Narayan, and K. L. Law, “Plastic waste inputs from land into the ocean,” *Science*, vol. 347, no. 6223, pp. 768–771, 2015.
- [4] C. Morales-Caselles, J. Viejo, E. Martí, D. González-Fernández, H. Pragnell-Raasch, J. I. González-Gordillo, E. Montero, G. M. Arroyo, G. Hanke, V. S. Salvo, *et al.*, “An inshore–offshore sorting system revealed from global classification of ocean litter,” *Nature Sustainability*, vol. 4, no. 6, pp. 484–493, 2021.
- [5] Y. Liu, A. MacFadyen, Z.-G. Ji, and R. H. Weisberg, “Introduction to monitoring and modeling the deepwater horizon oil spill,” *Geophysical Monograph Series*, vol. 195, pp. 1–7, 2011.
- [6] T. Atkinson and P. Davis, “Longitudinal dispersion in natural channels: 1. experimental results from the river severn, uk,” *Hydrology and Earth System Sciences*, vol. 4, no. 3, pp. 345–353, 2000.
- [7] M. Fingas and C. Brown, “Review of oil spill remote sensing,” *Marine Pollution Bulletin*, vol. 83, no. 1, pp. 9–23, 2014.
- [8] S. Armitage, K. Awty-Carroll, D. Clewley, and V. Martinez-Vicente, “Detection and classification of floating plastic litter using a vessel-mounted video camera and deep learning,” *Remote Sensing*, vol. 14, no. 14, 2022.
- [9] L. Biermann, D. Clewley, V. Martinez-Vicente, and K. Topouzelis, “Finding plastic patches in coastal waters using optical satellite data,” *Scientific reports*, vol. 10, no. 1, p. 5364, 2020.

- [10] L. Lebreton, B. Slat, F. Ferrari, B. Sainte-Rose, J. Aitken, R. Marthouse, S. Hajbane, S. Cunsolo, A. Schwarz, A. Levivier, *et al.*, “Evidence that the great pacific garbage patch is rapidly accumulating plastic,” *Scientific reports*, vol. 8, no. 1, pp. 1–15, 2018.
- [11] C. van Lieshout, K. van Oeveren, T. van Emmerik, and E. Postma, “Automated river plastic monitoring using deep learning and cameras,” *Earth and space science*, vol. 7, no. 8, p. e2019EA000960, 2020.
- [12] I. Cortesi, “Artificial intelligence applied to multispectral imagery for fluvial macroplastics detection,” in *Proceedings of the joint international event 9th ARQUEOLÓGICA 2.0 & 3rd GEORES*, pp. 495–497, 2021.
- [13] M. Rußwurm, S. J. Venkatesa, and D. Tuia, “Large-scale detection of marine debris in coastal areas with sentinel-2,” *iScience*, 2023.
- [14] T. H. van Emmerik, S. Kirschke, L. J. Schreyers, S. Nath, C. Schmidt, and K. Wendt-Potthoff, “Estimating plastic pollution in rivers through harmonized monitoring strategies,” *Marine Pollution Bulletin*, vol. 196, p. 115503, 2023.
- [15] U. Andriolo, K. Topouzelis, T. H. van Emmerik, A. Papakonstantinou, J. G. Monteiro, A. Isobe, M. Hidaka, S. Kako, T. Kataoka, and G. Gonçalves, “Drones for litter monitoring on coasts and rivers: suitable flight altitude and image resolution,” *Marine pollution bulletin*, vol. 195, p. 115521, 2023.
- [16] P. F. Tasserou, T. H. van Emmerik, P. Vriend, R. Hauk, F. Alberti, Y. Mellink, and M. van der Ploeg, “Defining plastic pollution hotspots,” *Science of The Total Environment*, vol. 934, p. 173294, 2024.
- [17] S. Burak, E. Dogan, and C. Gazioglu, “Impact of urbanization and tourism on coastal environment,” *Ocean & Coastal Management*, vol. 47, no. 9-10, pp. 515–527, 2004.
- [18] C. Ji, C. J. Beegle-Krause, and J. D. Englehardt, “Formation, detection, and modeling of submerged oil: A review,” *Journal of Marine Science and Engineering*, vol. 8, no. 9, p. 642, 2020.
- [19] M. Paches, D. Aguado, R. Martínez-Guijarro, and I. Romero, “Long-term study of seasonal changes in phytoplankton community structure in the western mediterranean (valencian community),” *Environmental Science and Pollution Research*, vol. 26, pp. 14266–14276, 2019.

-
- [20] C. G. Avio, S. Gorbi, and F. Regoli, “Plastics and microplastics in the oceans: from emerging pollutants to emerged threat,” *Marine environmental research*, vol. 128, pp. 2–11, 2017.
- [21] M. Spalding, L. Burke, S. A. Wood, J. Ashpole, J. Hutchison, and P. Zu Ermgassen, “Mapping the global value and distribution of coral reef tourism,” *Marine Policy*, vol. 82, pp. 104–113, 2017.
- [22] L. J. Meijer, T. Van Emmerik, R. Van Der Ent, C. Schmidt, and L. Lebreton, “More than 1000 rivers account for 80% of global riverine plastic emissions into the ocean,” *Science Advances*, vol. 7, no. 18, p. eaaz5803, 2021.
- [23] D. S. Green, “Biological and ecological impacts of plastic debris in aquatic ecosystems,” in *Plastics in the Aquatic Environment-Part I: Current Status and Challenges*, pp. 111–133, Springer, 2020.
- [24] A. Markic, C. Niemand, J. H. Bridson, N. Mazouni-Gaertner, J.-C. Gaertner, M. Eriksen, and M. Bowen, “Double trouble in the south pacific subtropical gyre: Increased plastic ingestion by fish in the oceanic accumulation zone,” *Marine Pollution Bulletin*, vol. 136, pp. 547–564, 2018.
- [25] F. Gallo, C. Fossi, R. Weber, D. Santillo, J. Sousa, I. Ingram, A. Nadal, and D. Romano, “Marine litter plastics and microplastics and their toxic chemicals components: the need for urgent preventive measures,” in *Analysis of Nanoplastics and Microplastics in Food*, pp. 159–179, CRC Press, 2020.
- [26] G. Andreoli, B. Bulgarelli, B. Hosgood, and D. Tarchi, “Hyperspectral analysis of oil and oil-impacted soils for remote sensing purposes,” *European Commission Joint Research Centre: Luxembourg*, vol. 36, pp. 2–30, 2007.
- [27] D. Angelova, I. Uzunov, S. Uzunova, A. Gigova, and L. Minchev, “Kinetics of oil and oil products adsorption by carbonized rice husks,” *Chemical Engineering Journal*, vol. 172, no. 1, pp. 306–311, 2011.
- [28] A. K. Mishra and G. S. Kumar, “Weathering of oil spill: Modeling and analysis,” *Aquatic Procedia*, vol. 4, pp. 435–442, 2015. International Conference on Water Resources, Coastal and Ocean Engineering (ICWRCOE’15).
- [29] J. K. Keesing, A. Gartner, M. Westera, G. J. Edgar, J. Myers, N. J. Hardman-Mountford, and M. Bailey, “Impacts and environmental risks of

- oil spills on marine invertebrates, algae and seagrass: A global review from an Australian perspective,” *Oceanography and Marine Biology*, 2018.
- [30] C. R. Fisher, P. A. Montagna, and T. T. Sutton, “How did the deepwater horizon oil spill impact deep-sea ecosystems?,” *Oceanography*, vol. 29, no. 3, pp. 182–195, 2016.
- [31] J. Beyer, H. C. Trannum, T. Bakke, P. V. Hodson, and T. K. Collier, “Environmental effects of the deepwater horizon oil spill: a review,” *Marine pollution bulletin*, vol. 110, no. 1, pp. 28–51, 2016.
- [32] C. Court, A. W. Hodges, K. Coffey, C. H. Ainsworth, and D. Yoskowitz, “Effects of the deepwater horizon oil spill on human communities: Catch and economic impacts,” *Deep Oil Spills: Facts, Fate, and Effects*, pp. 569–580, 2020.
- [33] J. L. Martin, R. W. Schottman, and S. C. McCutcheon, *Hydrodynamics and transport for water quality modeling*. CRC press, 2018.
- [34] A. Okubo, *Oceanic diffusion diagrams*, vol. 18. Elsevier, 1971.
- [35] A. Kistovich and T. Chaplina, “Analytical and experimental modeling of the hydrocarbon slick form and its spreading on the water surface,” *Physics of Fluids*, vol. 33, no. 7, 2021.
- [36] E. Van Sebille, S. Aliani, K. L. Law, N. Maximenko, J. M. Alsina, A. Bagaev, M. Bergmann, B. Chapron, I. Chubarenko, A. Cózar, *et al.*, “The physical oceanography of the transport of floating marine debris,” *Environmental Research Letters*, vol. 15, no. 2, p. 023003, 2020.
- [37] D. B. Clark, L. Lenain, F. Feddersen, E. Boss, and R. Guza, “Aerial imaging of fluorescent dye in the near shore,” *Journal of Atmospheric and Oceanic Technology*, vol. 31, no. 6, pp. 1410–1421, 2014.
- [38] C. J. Köppl, U. S. McKnight, G. G. Lemaire, A. M. Nørregaard, T. C. Thiim, P. L. Bjerg, P. Bauer-Gottwein, and M. García, “Tracer concentration mapping in a stream with hyperspectral images from unoccupied aerial systems,” *Advances in Water Resources*, vol. 182, p. 104567, 2023.
- [39] M. Filippi, R. Hanlon, I. I. Rypina, B. A. Hodges, T. Peacock, and D. G. Schmale III, “Tracking a surrogate hazardous agent (rhodamine dye) in a coastal ocean environment using in situ measurements and concentration estimates derived from drone images,” *Remote Sensing*, vol. 13, no. 21, p. 4415, 2021.

-
- [40] C. Brekke and A. H. Solberg, "Oil spill detection by satellite remote sensing," *Remote Sensing of Environment*, vol. 95, no. 1, pp. 1–13, 2005.
- [41] C. Elachi and J. J. Van Zyl, *Introduction to the physics and techniques of remote sensing*. John Wiley & Sons, 2021.
- [42] G. Camps-Valls, D. Tuia, L. Gómez-Chova, S. Jiménez, and J. Malo, "Remote sensing image processing," *Synthesis Lectures on Image, Video, and Multimedia Processing*, vol. 5, no. 1, pp. 1–192, 2011.
- [43] H. J. Kramer *et al.*, *Observation of the Earth and its Environment: Survey of Missions and Sensors*, vol. 1982. Springer, 2002.
- [44] V. Satriano, E. Ciancia, T. Lacava, N. Pergola, and V. Tramutoli, "Improving the rst-oil algorithm for oil spill detection under severe sun glint conditions," *Remote Sensing*, vol. 11, no. 23, 2019.
- [45] K. Tempfli, G. Huurneman, W. Bakker, L. L. Janssen, W. Feringa, A. Gieske, K. Grabmaier, C. Hecker, J. Horn, N. Kerle, *et al.*, *Principles of remote sensing: an introductory textbook*. International Institute for Geo-Information Science and Earth Observation, 2009.
- [46] Á. Pérez-García, A. Rodríguez-Molina, E. Hernández, L. Vera, and J. F. López, "Development of low-cost multi-spectral cameras for precision agriculture," in *IGARSS 2023 - 2023 IEEE International Geoscience and Remote Sensing Symposium*, pp. 3466–3469, 2023.
- [47] Á. Pérez-García, M. E. Paoletti, J. M. Haut, and J. F. López, "Novel spectral loss function for unsupervised hyperspectral image segmentation," *IEEE Geoscience and Remote Sensing Letters*, vol. 20, pp. 1–5, 2023.
- [48] C. J. Legleiter, R. R. McDonald, J. M. Nelson, P. J. Kinzel, R. L. Perroy, D. Baek, and I. W. Seo, "Remote sensing of tracer dye concentrations to support dispersion studies in river channels," *Journal of Ecohydraulics*, vol. 4, no. 2, pp. 131–146, 2019.
- [49] O. Garcia-Pineda, J. Holmes, M. Rissing, R. Jones, C. Wobus, J. Svejksky, and M. Hess, "Detection of oil near shorelines during the deepwater horizon oil spill using synthetic aperture radar (sar)," *Remote Sensing*, vol. 9, no. 6, 2017.
- [50] L. Gómez-Chova, G. Camps-Valls, J. Calpe-Maravilla, L. Guanter, and J. Moreno, "Cloud-screening algorithm for envisat/meris multispectral images," *IEEE Transactions on Geoscience and Remote Sensing*, vol. 45, no. 12, pp. 4105–4118, 2007.

- [51] G. Vane, R. O. Green, T. G. Chrien, H. T. Enmark, E. G. Hansen, and W. M. Porter, “The airborne visible/infrared imaging spectrometer (aviris),” *Remote Sensing of Environment*, vol. 44, no. 2, pp. 127–143, 1993.
- [52] R. O. Green, M. L. Eastwood, C. M. Sarture, T. G. Chrien, M. Aronsson, B. J. Chippendale, J. A. Faust, B. E. Pavri, C. J. Chovit, M. Solis, *et al.*, “Imaging spectroscopy and the airborne visible/infrared imaging spectrometer (aviris),” *Remote sensing of environment*, vol. 65, no. 3, pp. 227–248, 1998.
- [53] W. Emery and A. Camps, *Introduction to satellite remote sensing: atmosphere, ocean, land and cryosphere applications*. Amsterdam: Elsevier, 2017.
- [54] S. Zhang, S. Li, W. Fu, and L. Fang, “Multiscale superpixel-based sparse representation for hyperspectral image classification,” *Remote Sensing*, vol. 9, no. 2, p. 139, 2017.
- [55] J. L. García, M. E. Paoletti, L. I. Jiménez, J. M. Haut, and A. Plaza, “Efficient semantic segmentation of hyperspectral images using adaptable rectangular convolution,” *IEEE Geoscience and Remote Sensing Letters*, vol. 19, pp. 1–5, 2022.
- [56] N. Audebert, B. L. Saux, and S. Lefèvre, “Deep learning for classification of hyperspectral data: A comparative review,” *IEEE Geoscience and Remote Sensing Magazine*, vol. 7, pp. 159–173, 2019.
- [57] C. R. Jackson and W. Alpers, “The role of the critical angle in brightness reversals on sunglint images of the sea surface,” *Journal of Geophysical Research: Oceans*, vol. 115, no. C9, 2010.
- [58] S. Hafeez, M. S. Wong, S. Abbas, C. Y. Kwok, J. Nichol, K. H. Lee, D. Tang, and L. Pun, “Detection and Monitoring of Marine Pollution Using Remote Sensing Technologies,” in *Monitoring of Marine Pollution* (H. B. Fouzia, ed.), Chapters, IntechOpen, September 2019.
- [59] Á. Pérez-García, T. H. van Emmerik, A. Mata, P. F. Tasserón, and J. F. López, “Efficient plastic detection in coastal areas with selected spectral bands,” *Marine Pollution Bulletin*, vol. 207, p. 116914, 2024.
- [60] B. E. Mahrad, A. Newton, J. D. Icely, I. Kacimi, S. Abalansa, and M. Snoussi, “Contribution of remote sensing technologies to a holistic coastal and marine environmental management framework: a review,” *Remote Sensing*, vol. 12, no. 14, p. 2313, 2020.

-
- [61] Á. Pérez-García, A. Rodríguez-Molina, E. Hernández, and J. F. López Feliciano, "Spectral indices survey for oil spill detection in coastal areas," *IEEE Journal of Selected Topics in Applied Earth Observations and Remote Sensing*, vol. 17, pp. 15359–15372, 2024.
- [62] T. Bijeesh and K. Narasimhamurthy, "A comparative study of spectral indices for surface water delineation using landsat 8 images," in *2019 International Conference on Data Science and Communication (IconDSC)*, pp. 1–5, IEEE, 2019.
- [63] P. Kolokoussis and V. Karathanassi, "Oil spill detection and mapping using sentinel 2 imagery," *Journal of Marine Science and Engineering*, vol. 6, no. 4, pp. 1–12, 2018.
- [64] D. A. Carlson, T. N.; Ripley, "On the relation between ndvi, fractional vegetation cover, and leaf area index," *Remote Sensing of Environment*, vol. 62, no. 3, 1997.
- [65] C. Hu, Z. Lee, and B. Franz, "Chlorophyll algorithms for oligotrophic oceans: A novel approach based on three-band reflectance difference," *Journal of Geophysical Research: Oceans*, vol. 117, no. C1, 2012.
- [66] D. J. Lary, A. H. Alavi, A. H. Gandomi, and A. L. Walker, "Machine learning in geosciences and remote sensing," *Geoscience Frontiers*, vol. 7, no. 1, pp. 3–10, 2016.
- [67] L. Mou, P. Ghamisi, and X. X. Zhu, "Unsupervised spectral–spatial feature learning via deep residual conv–deconv network for hyperspectral image classification," *IEEE Transactions on Geoscience and Remote Sensing*, vol. 56, no. 1, pp. 391–406, 2018.
- [68] L. Zhang and L. Zhang, "Artificial intelligence for remote sensing data analysis: A review of challenges and opportunities," *IEEE Geoscience and Remote Sensing Magazine*, vol. 10, no. 2, pp. 270–294, 2022.
- [69] O. Campesato, *Artificial intelligence, machine learning, and deep learning*. Mercury Learning and Information, 2020.
- [70] A. E. Maxwell, T. A. Warner, and F. Fang, "Implementation of machine-learning classification in remote sensing: An applied review," *International journal of remote sensing*, vol. 39, no. 9, pp. 2784–2817, 2018.
- [71] D. Fitton, E. Laurens, N. Hongkarnjanakul, C. Schwob, and L. Mezeix, "Land cover classification through convolutional neural network model assembly: A case study of a local rural area in thailand," *Remote Sensing Applications: Society and Environment*, vol. 26, p. 100740, 2022.

- [72] Q. Yuan, H. Shen, T. Li, Z. Li, S. Li, Y. Jiang, H. Xu, W. Tan, Q. Yang, J. Wang, *et al.*, “Deep learning in environmental remote sensing: Achievements and challenges,” *Remote sensing of Environment*, vol. 241, p. 111716, 2020.
- [73] L. Bottou, F. E. Curtis, and J. Nocedal, “Optimization methods for large-scale machine learning,” *SIAM review*, vol. 60, no. 2, pp. 223–311, 2018.
- [74] P. Bajcsy and P. Groves, “Methodology for hyperspectral band selection,” *Photogrammetric Engineering & Remote Sensing*, vol. 70, no. 7, pp. 793–802, 2004.
- [75] O. Kramer and O. Kramer, “Scikit-learn,” *Machine learning for evolution strategies*, pp. 45–53, 2016.
- [76] M. Paoletti, J. Haut, J. Plaza, and A. Plaza, “Deep learning classifiers for hyperspectral imaging: A review,” *ISPRS Journal of Photogrammetry and Remote Sensing*, vol. 158, pp. 279–317, 2019.
- [77] C. Huang, L. Davis, and J. Townshend, “An assessment of support vector machines for land cover classification,” *International Journal of remote sensing*, vol. 23, no. 4, pp. 725–749, 2002.
- [78] Y. Hua, D. Marcos, L. Mou, X. X. Zhu, and D. Tuia, “Semantic segmentation of remote sensing images with sparse annotations,” *IEEE Geoscience and Remote Sensing Letters*, vol. 19, pp. 1–5, 2021.
- [79] M. Hearst, S. Dumais, E. Osuna, J. Platt, and B. Scholkopf, “Support vector machines,” *IEEE Intelligent Systems and their Applications*, vol. 13, no. 4, pp. 18–28, 1998.
- [80] T. K. Ho, “Random decision forests,” in *Proceedings of 3rd International Conference on Document Analysis and Recognition*, vol. 1, pp. 278–282 vol.1, 1995.
- [81] M. P. Barbato, P. Napoletano, F. Piccoli, and R. Schettini, “Unsupervised segmentation of hyperspectral remote sensing images with superpixels,” *Remote Sensing Applications: Society and Environment*, vol. 28, p. 100823, 2022.
- [82] J. A. Hartigan and M. A. Wong, “Algorithm as 136: A k-means clustering algorithm,” *Journal of the royal statistical society. series c (applied statistics)*, vol. 28, no. 1, pp. 100–108, 1979.

-
- [83] J. Nalepa, M. Myller, Y. Imai, K.-i. Honda, T. Takeda, and M. Antoniak, “Unsupervised segmentation of hyperspectral images using 3-d convolutional autoencoders,” *IEEE Geoscience and Remote Sensing Letters*, vol. 17, no. 11, pp. 1948–1952, 2020.
- [84] L. Wang, R. Li, C. Duan, C. Zhang, X. Meng, and S. Fang, “A novel transformer based semantic segmentation scheme for fine-resolution remote sensing images,” *IEEE Geoscience and Remote Sensing Letters*, vol. 19, pp. 1–5, 2022.
- [85] Y. Duan, F. Luo, M. Fu, Y. Niu, and X. Gong, “Classification via structure-preserved hypergraph convolution network for hyperspectral image,” *IEEE Transactions on Geoscience and Remote Sensing*, vol. 61, pp. 1–13, 2023.
- [86] T. Guo, R. Wang, F. Luo, X. Gong, L. Zhang, and X. Gao, “Dual-view spectral and global spatial feature fusion network for hyperspectral image classification,” *IEEE Transactions on Geoscience and Remote Sensing*, pp. 1–1, 2023.
- [87] O. Manas, A. Lacoste, X. Giró-i Nieto, D. Vazquez, and P. Rodriguez, “Seasonal contrast: Unsupervised pre-training from uncurated remote sensing data,” in *Proceedings of the IEEE/CVF International Conference on Computer Vision*, pp. 9414–9423, 2021.
- [88] A. Hosna, E. Merry, J. Gyalmo, Z. Alom, Z. Aung, and M. A. Azim, “Transfer learning: a friendly introduction,” *Journal of Big Data*, vol. 9, no. 1, p. 102, 2022.
- [89] S. J. Pan and Q. Yang, “A survey on transfer learning,” *IEEE Transactions on knowledge and data engineering*, vol. 22, no. 10, pp. 1345–1359, 2009.
- [90] D. Baek, I. W. Seo, J. S. Kim, and J. M. Nelson, “Uav-based measurements of spatio-temporal concentration distributions of fluorescent tracers in open channel flows,” *Advances in water resources*, vol. 127, pp. 76–88, 2019.
- [91] C. J. Legleiter, P. V. Manley, S. O. Erwin, and E. A. Bulliner, “An experimental evaluation of the feasibility of inferring concentrations of a visible tracer dye from remotely sensed data in turbid rivers,” *Remote Sensing*, vol. 12, no. 1, p. 57, 2019.
- [92] K. Johansen, A. F. Dunne, Y.-H. Tu, S. Almashharawi, B. H. Jones, and M. F. McCabe, “Dye tracing and concentration mapping in coastal waters using unmanned aerial vehicles,” *Scientific Reports*, vol. 12, no. 1, p. 1141, 2022.

- [93] K. Topouzelis, D. Papageorgiou, G. Suaria, and S. Aliani, “Floating marine litter detection algorithms and techniques using optical remote sensing data: A review,” *Marine Pollution Bulletin*, vol. 170, p. 112675, 2021.
- [94] L. Schreyers, T. van Emmerik, L. Biermann, and M. van der Ploeg, “Direct and indirect river plastic detection from space,” in *IGARSS 2022 - 2022 IEEE International Geoscience and Remote Sensing Symposium*, pp. 5539–5542, 2022.
- [95] J. M. Haut, S. Moreno-Alvarez, R. Pastor-Vargas, Á. Pérez-García, and M. E. Paoletti, “Cloud-based analysis of large-scale hyperspectral imagery for oil spill detection,” *IEEE Journal of Selected Topics in Applied Earth Observations and Remote Sensing*, vol. 17, pp. 2461–2474, 2024.
- [96] Á. Pérez-García, A. Martín Lorenzo, E. Hernández, A. Rodríguez-Molina, T. H. M. van Emmerik, and J. F. López, “Developing a generalizable spectral classifier for rhodamine detection in aquatic environments,” *Remote Sensing*, vol. 16, no. 3090, pp. 1–18, 2024.
- [97] V. Martínez-Vicente, J. R. Clark, P. Corradi, S. Aliani, M. Arias, M. Bochow, G. Bonnery, M. Cole, A. Cózar, R. Donnelly, F. Echevarría, F. Galgani, S. P. Garaba, L. Goddijn-Murphy, L. Lebreton, H. A. Leslie, P. K. Lindeque, N. Maximenko, F.-R. Martin-Lauzer, D. Moller, P. Murphy, L. Palombi, V. Raimondi, J. Reisser, L. Romero, S. G. Simis, S. Sterckx, R. C. Thompson, K. N. Topouzelis, E. van Sebille, J. M. Veiga, and A. D. Vethaak, “Measuring marine plastic debris from space: Initial assessment of observation requirements,” *Remote Sensing*, vol. 11, no. 20, 2019.
- [98] A. Cózar, M. Arias, G. Suaria, J. Viejo, S. Aliani, A. Koutroulis, J. Delaney, G. Bonnery, D. Macías, R. de Vries, *et al.*, “Proof of concept for a new sensor to monitor marine litter from space,” *Nature Communications*, vol. 15, no. 1, p. 4637, 2024.
- [99] W. Sun and Q. Du, “Hyperspectral band selection: A review,” *IEEE Geoscience and Remote Sensing Magazine*, vol. 7, no. 2, pp. 118–139, 2019.
- [100] D. L. Donoho *et al.*, “High-dimensional data analysis: The curses and blessings of dimensionality,” *AMS math challenges lecture*, vol. 1, no. 2000, p. 32, 2000.
- [101] L. Qiao, W. Tang, D. Gao, R. Zhao, L. An, M. Li, H. Sun, and D. Song, “Uav-based chlorophyll content estimation by evaluating vegetation index

- responses under different crop coverages,” *Computers and electronics in agriculture*, vol. 196, p. 106775, 2022.
- [102] A. Karnieli, N. Agam, R. T. Pinker, M. Anderson, M. L. Imhoff, G. G. Gutman, N. Panov, and A. Goldberg, “Use of ndvi and land surface temperature for drought assessment: Merits and limitations,” *Journal of climate*, vol. 23, no. 3, pp. 618–633, 2010.
- [103] L. Mou, S. Saha, Y. Hua, F. Bovolo, L. Bruzzone, and X. X. Zhu, “Deep reinforcement learning for band selection in hyperspectral image classification,” *IEEE Transactions on Geoscience and Remote Sensing*, vol. 60, pp. 1–14, 2021.
- [104] N. Pahlevan, S. Sarkar, B. Franz, S. Balasubramanian, and J. He, “Sentinel-2 multispectral instrument (msi) data processing for aquatic science applications: Demonstrations and validations,” *Remote Sensing of Environment*, vol. 201, pp. 47 – 56, 2017.
- [105] R. Morfitt, J. Barsi, R. Levy, B. Markham, E. Micijevic, L. Ong, P. Scaramuzza, and K. Vanderwerff, “Landsat-8 operational land imager (oli) radiometric performance on-orbit,” *Remote Sensing*, vol. 7, no. 2, pp. 2208–2237, 2015.
- [106] M. E. Grötte, R. Birkeland, E. Honoré-Livermore, S. Bakken, J. L. Garrett, E. F. Prentice, F. Sigernes, M. Orlandić, J. T. Grasdahl, and T. A. Johansen, “Ocean color hyperspectral remote sensing with high resolution and low latency—the hypso-1 cubesat mission,” *IEEE Transactions on Geoscience and Remote Sensing*, vol. 60, no. 1000619, pp. 1–19, 2022.
- [107] C. J. Legleiter, B. J. Sansom, and R. B. Jacobson, “Remote sensing of visible dye concentrations during a tracer experiment on a large, turbid river,” *Water Resources Research*, vol. 58, no. 4, p. e2021WR031396, 2022.
- [108] M. Xu, M. Wu, K. Chen, C. Zhang, and J. Guo, “The eyes of the gods: A survey of unsupervised domain adaptation methods based on remote sensing data,” *Remote Sensing*, vol. 14, no. 17, p. 4380, 2022.
- [109] Y. Ma, S. Chen, S. Ermon, and D. B. Lobell, “Transfer learning in environmental remote sensing,” *Remote Sensing of Environment*, vol. 301, p. 113924, 2024.
- [110] G. Michau and O. Fink, “Unsupervised transfer learning for anomaly detection: Application to complementary operating condition transfer,” *Knowledge-Based Systems*, vol. 216, p. 106816, 2021.

- [111] A. E. de Investigación (AEI), “Redes de investigación 2022.” <https://www.aei.gob.es/convocatorias/buscador-convocatorias/redes-investigacion-2022>, 2022. Accessed: 2024-08-18.
- [112] E. S. A. (ESA), “Living planet symposium,” 2022. Accessed: 2024-08-18.
- [113] Á. Pérez-García, P. Horstrand, and J. F. López, “A novel spectral index for ocean oil spill detection,” in *ESA Living Planet Symposium*, 2022.
- [114] I. E. Society, “Edunine 2023 - vii iee world engineering education conference,” 2023. Accessed: 2024-08-18.
- [115] Á. Pérez García and J. F. López Feliciano, “Impact of covid-19 on education: Evolution of virtual laboratories,” in *2023 IEEE World Engineering Education Conference (EDUNINE)*, pp. 1–4, 2023.
- [116] Á. Pérez-García, A. M. Lorenzo, and J. López, “Spectral band selection methodology for future sensor development,” in *2024 47th MIPRO ICT and Electronics Convention (MIPRO)*, pp. 152–156, 2024.
- [117] S. Wold, K. Esbensen, and P. Geladi, “Principal component analysis,” *Chemometrics and intelligent laboratory systems*, vol. 2, no. 1-3, pp. 37–52, 1987.
- [118] H. Abdi and L. J. Williams, “Principal component analysis,” *Wiley interdisciplinary reviews: computational statistics*, vol. 2, no. 4, pp. 433–459, 2010.
- [119] N. Developers, “Numpy gradient function,” 2024. Accessed: 2024-06-26.
- [120] C. J. Legleiter, V. M. Scholl, B. J. Sansom, and M. A. Burgess, “Hyperspectral image transects during transient events in rivers (hitter): Framework development and application to a tracer experiment on the missouri river, usa,” *Remote Sensing*, vol. 16, no. 3743, pp. 1–33, 2024.
- [121] M. Carroll, A. Van Der Merwe, and P. Kotze, “Secure cloud computing: Benefits, risks and controls,” in *2011 Information Security for South Africa*, pp. 1–9, IEEE, 2011.
- [122] M. Amani, A. Ghorbanian, S. A. Ahmadi, M. Kakooei, A. Moghimi, S. M. Mirmazloumi, S. H. A. Moghaddam, S. Mahdavi, M. Ghahremanloo, S. Parsian, *et al.*, “Google earth engine cloud computing platform for remote sensing big data applications: A comprehensive review,” *IEEE Journal of Selected Topics in Applied Earth Observations and Remote Sensing*, vol. 13, pp. 5326–5350, 2020.

- [123] SILIOS Technologies, “Multispectral Cameras. CMS Series.” <https://www.silios.com/cms-series>. [Online; accessed 03-Jan-2023].
- [124] MAIA, the multispectral camera, “MAIA WV model.” <https://www.spectralcam.com/maia-tech/>. [Online; accessed 06-Oct-2019].
- [125] Specim Spectral Imaging, “FX Series hyperspectral cameras.” <http://www.specim.fi/fx/>. [Online; accessed 06-Oct-2019].
- [126] J. M. Haut, J. A. Gallardo, M. E. Paoletti, G. Cavallaro, J. Plaza, A. Plaza, and M. Riedel, “Cloud deep networks for hyperspectral image analysis,” *IEEE transactions on geoscience and remote sensing*, vol. 57, no. 12, pp. 9832–9848, 2019.
- [127] N. Gorelick, M. Hancher, M. Dixon, S. Ilyushchenko, D. Thau, and R. Moore, “Google earth engine: Planetary-scale geospatial analysis for everyone,” *Remote sensing of Environment*, vol. 202, pp. 18–27, 2017.
- [128] B. Wilder, *Cloud architecture patterns: using microsoft azure.* ” O’Reilly Media, Inc.”, 2012.
- [129] J. M. Haut and M. E. Paoletti, “Cloud implementation of multinomial logistic regression for uav hyperspectral images,” *IEEE Journal on Miniaturization for Air and Space Systems*, vol. 1, no. 3, pp. 163–171, 2020.

